RADIATIONHYDRODYNAMICAL EQUILIBRIUM AND DUST MECHANICS IN PROTOPLANETARY ACCRETION DISKS

Von der Universität Bayreuth
zur Erlangung des Grades eines
Doktors der Naturwissenschaften (Dr. rer. nat.)
genehmigte Abhandlung

von

Benjamin N. Schobert

aus Helmbrechts

1. Gutachter Prof. Dr. Arthur G. Peeters
2. Gutachter Prof. Dr. Gregor J. Golabek

Tag der Einreichung: 28.05.2024
Tag des Kolloquiums: 09.10.2024

This thesis is dedicated to my late grandfather, Karl-Wilhelm Meisel, who encouraged me to pursue an academic career and continuously supported me along the way.

Contents

Chapter 1

Summary

Accretion is a phenomenon commonly observed throughout the universe across many length scales (Clarke & Carswell 2009). From active galactic nuclei (AGN), located at the center of galaxies, at the largest scale (Shakura 2018) to small T Tauri stars and their accretion disks on the smaller side. Their feature of commonalty is matter, in the form of gas (or sometimes plasma) and dust falling onto the central object due to gravity.

This thesis specifically researches protoplanetary disks. These are accretion disks around young stellar objects (YSOs), with the potential to form planets. The process of planet formation and, closely connected, the structure of planetary disks are topics of great interest in astrophysics. Understanding the intricacies of distant protoplanetary disks could also lead to insights in the formation of the solar system. Ever improving earthbound and satellite telescopes are currently observing nascent exoplanets in ever increasing numbers (Keppler, M. et al. 2018), as well as probing the extend of proto-planetary disks and their spatially resolved radiation. This radiation can be scrutinized in spectra and through interferometry as visibility curves.

In order to make conclusions from experimental observations to the inner workings of the disk, a physically self-consistent model of the processes within the disk is necessary. Such a model has been realised in this work as a numerical simulation. The model includes the radiative transfer of energy from the star onto the disk, the transport of energy through the disk via radiative diffusion and thermal conduction, the dissipation of energy as it is converted from the motion of accretion to heat, and the energy loss from the disk through radiative cooling (Schobert et al. 2019). It includes the equilibrium of the density within the disk with respect to the stellar gravity, its own gravity, the centrifugal force and steady-state accretion. Most importantly it includes the sublimation and reformation of the dust at the inner rim of the disk, as well as the diffusion of dust via turbulence as it bounds to the gas (Schobert, B. N. & Peeters, A. G. 2021).

This thesis features three different publications, which will for brevity be referred to as (SPR19) (Schobert et al. 2019), (SP21) (Schobert, B. N. & Peeters, A. G. 2021) and (SVUFP24) in the following. The latest one is currently in review at Astronomy & Astrophysics. The three publications are closely connected and form a coherent path that cumulates in the final publication. While the first two publications can certainly be seen to stand on their own based on scientific merit, they simultaneously lay the foundations for the third paper.

The first work (SPR19) investigates the influence of accretion heating and turbulent heat conduction on the equilibrium of protoplanetary disks. Extending a previous 2D axis-symmetric passive disk model (Flock et al. 2016) a new and independent numerical code was developed. The model includes dust sublimation and radiative transfer with the flux-limited diffusion approximation, and predicts the density and temperature profiles as well as the dust-to-gas ratio of the disk. It is shown that the addition of accretion heating has a large impact: For accretion rates above $5 \cdot 10^{-8}\, M_{\odot}/\mathrm{yr}$ (solar masses per year) a zone forms behind the silicate condensation front with sufficiently high temperature to sublimate the dust and form a gaseous cavity. Assuming a Prandtl number ~ 0.7, it is furthermore shown that the turbulent heat conduction cannot be neglected in the evaluation of the temperature profile. While the inner rim position is not affected by viscous heating, the dead zone edge shifts radially outward for higher accretion rates. The main impact of this work was the previously often neglected accretion heating. This effect is therefore necessarily included in all the following works.

The second work (SP21) hypothesizes if turbulence in protoplanetary disks is necessary for accretion and small dust particles are well coupled to the gas, they have to undergo diffusion due to this turbulent motion. SP21 then investigates the influence of turbulence-induced dust diffusion on the equilibrium of protoplanetary disks, by including dust diffusion in the model. It is shown that dust diffusion can have a large impact: Assuming the dust survives for 10^4 seconds or longer before it can be evaporated, this leads the dust diffusion to widen the inner disk considerably. This effect is generated through a feedback mechanism as the diffusion length is much shorter than the disk width. With increasing dust diffusion, the inclination of the inner rim toward the stellar radiation becomes steeper until it is almost vertical. The temperature range of evaporation and condensation, which is linked to the dust composition, has no influence on this effect. For realistic parameters, dust diffusion cannot be neglected when determining the equilibrium of the disk. Stronger turbulence inside the disk induces more dust diffusion. Therefore, the dust density grows more gradually over a greater distance and less radiation reaches the disk surface. The new equilibrium shape of the disk is more inclined toward the star. This effect is universal and independent of the specific dust composition. The main impact of this work is the inclusion of dust diffusion, which enables a significantly better and physically more realistic treatment of the dust sublimation front. This effect is therefore necessarily included in the following work.

The third and final paper (SVUFP24) uses the now fully developed model (with accretion heating and dust diffusion) to explain the spectral energy distribution and visibility curves in near- and mid-infrared of the Herbig Ae star HD 144432. HD 144432 is an object of elevated interest in the astrophysical community (Pérez, M. R. et al. 2004; Carmona, A. et al. 2007; Müller, A. et al. 2011; Varga, J. et al. 2018), because its luminosity to radial extension relation is as theoretically expected in the near-infrared, but it is larger than expected in the mid-infrared region. It has this feature in common with several systems that have been observed and various theories have been proposed to explain this phenomenon. HD 144432 is like many other YSOs a system of multiple stars, specifically a hierarchical triple system. This paper finds that these companion stars to HD 144432A provide a necessary boundary condition on the outer rim of the disk and its ability to radiatively cool the disk. Further the influence of accretion heating cannot be neglected and is important for the understanding of the structure of this disk. This corresponds well with measured visibility curves from HD 144432, where mid infrared radiation, is observed coming from further away from the star as expected without accretion heating. Further it is possible to constrain the accretion rate and inner rim radius of the disk, as well as confining possible dust compositions. The 3 μm visibility curve is strongly connected to the inner rim position and there is an easy analytical equation connecting half-width of the visibility to the inner rim position. The 9 μm visibility curve is indicative of the amount of accretion heating within the disk, HD 144432 has a high turbulent viscosity, with $\alpha = 0.04$ and an accretion rate of $\dot{M} = 1.6 \cdot 10^{-8} M_{\odot}\mathrm{yr}^{-1}$. The SED is best reproduced with graphite and silicate particles with sizes in the range of 0.003-1 μm and an absorption to emission ratio of $\varepsilon = 0.11$. So (SVUFP24) presents a method, with which it is possible to extract decisive properties of a system from observational data using the proposed physical model. The code for which can be found online at `https://bitbucket.org/astro_bayreuth/rmhdcode`.

The structure of this thesis is as follows: after the English and German abstracts a theory chapter is provided with all the necessary derivations for the model used in the publications. In chapter 4 the numerics are explained, followed by a list of the publications and then the publications themselves.

Chapter 2

Zusammenfassung

Akkretion ist ein Phänomen, das über viele Längenskalen hinweg im gesamten Universum beobachtet wird (Clarke & Carswell 2009). Die größten Objekte sind aktive Galaxiekerne, die sich im Zentrum von Galaxien befinden (Shakura 2018) und am kleineren Ende der Skala sind die T-Tauri-Sterne mit ihren Akkretionsscheiben. Das gemeinsame Merkmal aller Akkretionsprozesse ist, dass Materie in Form von Gas (oder manchmal Plasma) und Staub aufgrund der Schwerkraft auf das zentrale Objekt fällt.

Diese Arbeit untersucht speziell protoplanetare Scheiben. Sie sind Akkretionsscheiben um junge Sterne, mit dem Potenzial, Planeten zu bilden. Der Prozess der Planetenbildung und, eng damit verbunden, die Struktur planetarer Scheiben sind Themen großen Interesses in der Astrophysik. Das Verständnis der Feinheiten entfernter protoplanetarer Scheiben könnte auch zu Einblicken in die Entstehung des Sonnensystems führen. Die sich stetig verbessernden bodengebundenen und Satelliten-Teleskope beobachten derzeit immer mehr junge Exoplaneten, die in der Entstehung begriffen sind (Keppler, M. et al. 2018). Außerdem sondieren die Teleskope die Ausdehnung protoplanetarer Scheiben und ihre räumlich aufgelöste Strahlung. Diese Strahlung kann in Spektren oder durch Interferometrie als Interferenzkurven untersucht werden.

Um Schlussfolgerungen aus experimentellen Beobachtungen auf die inneren Abläufe der Scheibe ziehen zu können, ist ein physikalisch selbst konsistentes Modell der Prozesse innerhalb der Scheibe erforderlich. Ein solches Modell wurde in dieser Arbeit als numerische Simulation realisiert. Das Modell umfasst den Strahlungstransport von Energie vom Stern auf die Scheibe, den Transport der Energie durch die Scheibe mittels Strahlungsdiffusion und Wärmeleitung, die Umwandlung von Energie, die durch Akkretionsheizung aus der Bewegung entsteht, und Verlust von Energie aus der Scheibe durch Strahlungskühlung (Schobert et al. 2019). Es umfasst das Kräftegleichgewicht eines Dichteelements innerhalb der Scheibe unter Berücksichtigung der Gravitation des Sterns, der Gravitation des Dichteelements selbst und der Zentrifugalkraft um stationäre Akkretion zu gewährleisten. Am wichtigsten ist jedoch die Sublimation und Kondensation des

Staubs am inneren Rand der Scheibe sowie die Diffusion des Staubs durch Turbulenz, während er sich im Gas suspendiert befindet (Schobert, B. N. & Peeters, A. G. 2021).

Diese Arbeit umfasst drei verschiedene Veröffentlichungen, die der Einfachheit halber im Folgenden als (SPR19) (Schobert et al. 2019), (SP21) (Schobert, B. N. & Peeters, A. G. 2021) und (SVUFP24) bezeichnet werden. Die neueste befindet sich derzeit in der Überprüfung bei "Astronomy & Astrophysics". Die drei Veröffentlichungen sind eng miteinander verbunden und bilden einen stringenten Weg hin zur abschließenden Veröffentlichung. Während die ersten beiden Veröffentlichungen aufgrund ihres wissenschaftlichen Beitrags für sich allein stehen können, legen sie gleichzeitig auch die Grundlagen für das dritte Papier.

Die erste Arbeit (SPR19) untersucht den Einfluss von Akkretionsheizung und turbulenter Wärmeleitung auf den Gleichgewichtszustand von protoplanetaren Scheiben. Der verwendete numerische Code wurde selbst entwickelt, basiert auf einem früheren 2D-achsensymmetrischen Modell (Flock et al. 2016) ohne Akkretionsheizung und erweitert dieses. Das Modell umfasst die Sublimation von Staub und den Strahlungstransport mit der flusslimitierten Diffusionsnäherung und sagt die Dichte- und Temperaturprofile sowie das Staub-zu-Gas-Verhältnis der Scheibe voraus. Es wird gezeigt, dass die Ergänzung der Akkretionsheizung einen großen Einfluss hat: Für Akkretionsraten über $5 \cdot 10^{-8}\, M_\odot$/Jahr (Sonnenmassen pro Jahr) bildet sich hinter der Silikatkondensationsfront eine Zone mit ausreichend hoher Temperatur, um den Staub zu sublimieren und eine gasförmige Kavität zu bilden. Unter der Annahme einer Prandtl-Zahl von ~ 0.7 wird außerdem gezeigt, dass die turbulente Wärmeleitung bei der Bewertung des Temperaturprofils nicht vernachlässigt werden kann. Während die Position des inneren Rands nicht von der viskosen Heizung beeinflusst wird, verschiebt sich der Rand der toten Zone radial nach außen bei höheren Akkretionsraten. Der Hauptbeitrag dieser Arbeit war die zuvor oft vernachlässigte Akkretionsheizung. Dieser Effekt ist daher in allen folgenden Arbeiten notwendigerweise enthalten.

Die zweite Arbeit (SP21) stellt die Hypothese auf, dass sich kleine Staubpartikel, die die Bewegung des Gases mitvollziehen, diffusiv verhalten aufgrund der Turbulenz des Gases, die für Akkretion in protoplanetaren Scheiben notwendig ist. SP21 untersucht dann den Einfluss der turbulenzinduzierten Staubdiffusion auf das Gleichgewicht von protoplanetaren Scheiben, indem die Staubdiffusion im Modell berücksichtigt wird. Es wird gezeigt, dass die Staubdiffusion einen großen Einfluss haben kann: Wenn angenommen wird, dass der Staub 10^4 Sekunden oder länger überlebt, bevor er sublimieren kann, führt dies dazu, dass die Staubdiffusion den inneren Rand der Scheibe erheblich erweitert. Dieser Effekt wird durch einen Rückkopplungsmechanismus erzeugt, da die Diffusionslänge viel kürzer ist als die Scheibenbreite. Mit zunehmender Staubdiffusion wird die Neigung des inneren Rands zur stellaren Strahlung steiler, bis sie fast vertikal ist. Der Temperaturbereich der Sublimation und Kondensation, der mit der Staubzusammensetzung verbunden ist, hat keinen Einfluss auf diesen Effekt. Für realistische Parameter kann die Staubdiffusion nicht vernachlässigt werden, wenn das Gleichgewicht der Scheibe bestimmt wird. Stärkere Turbulenzen innerhalb der Scheibe induzieren eine größere Staubdiffusion. Daher nimmt die Staubdichte über eine größere Entfernung allmählicher zu, und weniger Strahlung erreicht die Oberfläche der Scheibe. Die neue Gleichgewichtsform der Scheibe neigt sich stärker zum Stern hin. Dieser Effekt ist universell und unabhängig von der spezifischen Staubzusammensetzung. Der Hauptbeitrag dieser Arbeit besteht in der Berücksichtigung der Staubdiffusion, die eine deutlich bessere und physikalisch realistischere Behandlung der Staubsublimationsfront ermöglicht. Dieser Effekt ist daher in der folgenden Arbeit notwendigerweise enthalten.

Das dritte und abschließende Papier (SVUFP24) verwendet das nun vollständig entwickelte Modell (mit Akkretionsheizung und Staubdiffusion), um die spektrale Energiedichteverteilung und die Interferenzkurven im nahen und mittleren Infrarotbereichs des Herbig Ae-Sterns HD 144432 zu erklären. HD 144432 ist ein Objekt von hohem Interesse in der astrophysikalischen Gemeinschaft (Pérez, M. R. et al. 2004; Carmona, A. et al. 2007; Müller, A. et al. 2011; Varga, J. et al. 2018), weil sein Verhältnis von Leuchtkraft zu radialer Ausdehnung im Nahinfrarot theoretisch erwartungsgemäß ist, aber im mittleren Infrarot größer als erwartet ist. Es hat dieses Merkmal mit mehreren Systemen gemeinsam, die beobachtet wurden, und es wurden verschiedene Theorien vorgeschlagen, um dieses Phänomen zu erklären. HD 144432 ist wie viele andere Systeme aus mehreren Sternen zusammengesetzt, in diesem Fall handelt es sich speziell ein hierarchisches Dreifachsystem. Diese Arbeit zeigt, dass diese Begleitsterne von HD 144432A eine notwendige Randbedingung am äußeren Rand der Scheibe und ihre Fähigkeit zur Strahlungskühlung bereitstellen. Darüber hinaus kann der Einfluss der Akkretionsheizung nicht vernachlässigt werden und ist wichtig für das Verständnis der Struktur dieser Scheibe. Dies entspricht gut den gemessenen Interferenzkurven von HD 144432, bei denen mittlere Infrarot Strahlung, weiter vom Stern entfernt als ohne Akkretionsheizung erwartet, beobachtet wird. Weiterhin ist es möglich, die Akkretionsrate und den inneren Rand der Scheibe sowie mögliche Staubzusammensetzungen einzuschränken. Die 3 μm Interferenzkurve ist eng verknüpft mit der Position des Staubsublimationsfront und (SVUFP24) präsentiert einen analytischen Zusammenhang zwischen dem Halblichtradius der 3 μm Interferenzkurve und der Position der Sublimationsfront. Die 9 μm Interferenzkurve ist kenneichnend für die Menge an Akkretionswärme in der Scheibe, HD 144432 hat eine hohe turbulente Viskosität, mit $\alpha = 0.04$ und einer Akkretionsrate von $\dot{M} = 1.6 \cdot 10^{-8} M_{\odot}\mathrm{yr}^{-1}$. Die SED kann am besten mit der Simulation genähert werden, wenn Graphit- und Silikatpartikel als Staub angenommen werden mit Korngrößen von 0.003-1 μm und einem Verhältnis zwischen Absorption und Emission der Staubopazitäten von $\varepsilon = 0.11$. Daher präsentiert (SVUFP24) eine Methode, mit der es möglich ist, entscheidende Eigenschaften eines Systems aus Beobachtungsdaten unter Verwendung des vorgeschlagenen physikalischen Modells abzuleiten. Der Code hierfür ist online verfügbar unter

`https://bitbucket.org/astro_bayreuth/rmhdcode`.
Die Struktur dieser Arbeit ist wie folgt: Nach den englischen und deutschen Zusammenfassungen kommt ein Theoriekapitel mit allen notwendigen Herleitungen für das in den Veröffentlichungen verwendete Modell. In Kapitel 4 wird die Numerik erläutert, gefolgt von einer Liste der Veröffentlichungen und dann den Veröffentlichungen selbst.

Chapter 3

Theoretical Background

This chapter motivates the model equations and provides the necessary theoretical background for the three publications and the numerical framework used therein.

3.1 Protoplanetary disks

A protoplanetary disk is the material orbiting around a YSO, mainly dense gas and dust. The gas is comprised of mostly hydrogen and to a lesser part helium and other trace gases. The dust is mainly silicates, but iron and carbon based grains are also present to a lesser extent in some disks. The disk extents from close to the stellar surface to several astronomic units outward and its vertical dimension is much smaller than its radial distance from the star. The central star is either a Herbig Ae/Be star or a T Tauri star, depending on its mass. Herbig Ae/Be stars are slightly more massive (2-5 $M_\odot$) while younger than our sun (Herbig 1960) and T Tauri stars have even less mass ($<$2 $M_\odot$) and are also early in their evolution.

The specific mechanism of disk formation may vary in each scenario, yet initial insights can be gleaned through general principles. For instance, one could consider a gas cloud contracting due to its own gravitational pull (Clarke & Carswell 2009). Typically, the cloud possesses a finite angular momentum relative to its centre of mass, which remains conserved. Consequently, as the cloud's diameter decreases, its rotational velocity must increase. Meanwhile, internal energy can escape the system through radiation into the surrounding areas. The emitted photons carry energy but only very little momentum. As a result, the internal temperature and pressure decrease, while the angular momentum almost completely remains. After contracting in one dimension, the system tends to adopt a disk-like configuration.

These disks then evolve further, transporting angular momentum outwards and matter inwards to the central star in a process called accretion. It is aided by the viscosity of the flow, however, calculations show that the molecular viscosity within accretion disks would lead to much larger time scales of evolution than observed. Therefore the process of accretion within most protoplanetary disks must be aided by turbulence. This is further described in section 3.6.

The temperature in the disk generally decreases with the distance from its central star. So there is a position within the disk where it becomes sufficiently cold for the dust particles to be formed. This transition area is called the inner rim of the disk and it exists in a delicate balance with the stellar radiation. The presence of dust increases the opacity of the disk medium and thus more radiation is absorbed. Further, the disk rim, if it is sufficiently large, can cast a shadow on the disk behind it. Because of these effects the inner rim is a particular area of interest in the structure of protoplanetary disks.

It is advantageous to have a theoretical framework for a protostellar disk to assess it against empirical observations and to evaluate the impact of different factors. Given that the non-linear equations governing the evolution of such a disk lack known analytical solutions, employing numerical simulations emerges as the most viable approach.

The objective is to compute the density and temperature distributions of the disk for a star characterized by specific parameters, namely its mass M_*, radius R_*, and luminosity L_* (or alternatively, surface temperature T_*). The methodology adopted here closely mirrors that outlined in (Flock et al. 2016). Nonetheless, for thoroughness, the following sections motivate the model equations and provide the necessary theoretical background.

3.2 Hydrostatic Equilibrium

The density structure is derived by assuming hydrostatic equilibrium between the pressure exerted by an ideal gas, the centrifugal force and gravity. This assumption is justified due to the relatively rapid attainment of this equilibrium compared to other processes discussed in section 4.1, as demonstrated subsequently. To facilitate integration along the optical path later on, employing spherical coordinates (r, θ, ϕ) for the simulation proves convenient. The polar axis of the coordinate system aligns with the rotational axis of the disk, thereby situating the protostellar disk within the equatorial plane. Consequently, the azimuthal velocity of the gas substantially surpasses the radial or polar velocities ($v_\phi \gg v_r, v_\theta$). Commencing with the Euler equation

$$\rho\left(\partial_t \mathbf{v} + (\mathbf{v}\cdot\nabla)\mathbf{v}\right) = -\nabla p - \rho\nabla\Phi \tag{3.1}$$

and employing $\partial_t \mathbf{v} = 0$ along with the gradient in polar coordinates results in

$$\rho\frac{v_\phi}{r\sin\theta}\partial_\phi\left(v_\phi\hat{\boldsymbol{\phi}}\right) = -\nabla p - \rho\nabla\Phi. \tag{3.2}$$

In this context, ∂_x represents the partial derivative with respect to x. Next, one differentiates the unit vector $\hat{\boldsymbol{\phi}}$ with respect to ϕ and arranges the terms according to their unit vectors, yielding

$$-\rho\frac{v_\phi^2}{r\sin\theta}(\cos\theta\,\hat{\boldsymbol{\theta}}+\sin\theta\,\hat{\boldsymbol{r}}) = -\left(\partial_r p+\rho\partial_r\Phi\right)\hat{\boldsymbol{r}}-\frac{1}{r}\partial_\theta\, p\,\hat{\boldsymbol{\theta}} \tag{3.3}$$

$$\partial_r p = -\rho\partial_r\Phi+\frac{\rho\, v_\phi^2}{r} \tag{3.4}$$

$$\frac{1}{r}\partial_\theta\, p = \frac{\rho\, v_\phi^2}{r\tan\theta}\,, \tag{3.5}$$

where ρ represents the gas density, v_ϕ denotes the velocity in the azimuthal direction, and uppercase Φ denotes the gravitational potential, defined as $\Phi = \frac{GM_*}{r}$, where G is the gravitational constant and M_* is the stellar mass. The pressure p is incorporated for closure with the thermodynamic equations, assuming ideal gas pressure as follows:

$$p = \frac{\rho k_B T}{\mu_g u}, \tag{3.6}$$

where T denotes temperature, k_B signifies the Boltzmann constant, μ_g represents the mean molecular weight, and u denotes the atomic mass unit.

A reasonable approximation is that $\partial_\theta T = 0$, owing to the fact that many particles orbit around the star in a plane slightly tilted with respect to the equator. A small volume of these particles retains its temperature during one orbit, thus providing a constant temperature along θ for a fixed radius. Although not entirely accurate, this assumption provides further insight, as elaborated in section 4.3.1. Employing this approximation on equation (3.5) alongside (3.6), one obtains:

$$\frac{1}{r}\frac{k_B T}{\mu_g u}\partial_\theta\rho = \frac{\rho\, v_\phi^2}{r\tan\theta} \tag{3.7}$$

This simplifies to:

$$c_s^2\,\partial_\theta\rho = \frac{\rho\, v_\phi^2}{\tan\theta} \tag{3.8}$$

where $c_s = \sqrt{\partial_\rho p} = \sqrt{\frac{k_B T}{\mu_g u}}$ represents the isothermal speed of sound, and $\tan\theta = \frac{r}{z}$, where z is the height over the midplane, and $rd\theta \approx -dz \implies \partial_\theta \approx -r\partial_z$ around $\theta = \pi/2$ at the equator. Hence:

$$\frac{1}{\rho}\partial_z\rho = -\frac{v_\phi^2}{r^2\, c_s^2}z = -\frac{\Omega^2}{c_s^2}z \tag{3.9}$$

leading to the solution:

$$\rho(z) = \rho_0 \exp\left(-\frac{z^2}{2H^2}\right) \tag{3.10}$$

representing a Gaussian density profile for an isothermal disk. Here, H signifies the pressure scale height, defined as:

$$H = \frac{c_s}{\Omega}, \tag{3.11}$$

where the rotational frequency $\Omega = v_\phi / r$ is utilized. Substituting Ω with the Kepler rotational frequency:

$$\Omega_K = \sqrt{\frac{GM_*}{r^3}}\,, \tag{3.12}$$

the pressure scale height becomes:

$$H = \sqrt{\frac{k_B T r^3}{GM_* \mu_g u}} \tag{3.13}$$

with M_* representing the stellar mass. Defining the surface density as:

$$\Sigma(r) = \int\limits_{-\infty}^{\infty} \rho(r, z) dz \tag{3.14}$$

ρ_0 can be expressed through integration of (3.10) as:

$$\Sigma = \sqrt{2\pi} H \rho_0 \tag{3.15}$$

$$\rho_0 = \frac{\Sigma}{\sqrt{2\pi} H}\,. \tag{3.16}$$

This expression for ρ_0 is utilized to calculate the midplane density in the code, and by utilizing formulae (3.4) and (3.5), the density can be integrated for every point, as further explained in section 4.3.1.

3.3 Radiation equilibrium

To determine the temperature distribution, one must solve a coupled set of equations for the radiation energy density E_R and the internal energy density of the gas ϵ. These equations describe radiation transfer and represent a subset of ideal radiative magnetohydrodynamics (RMHD). If electric and magnetic fields were neglected, these equations, combined with those from the previous section, would describe the complete ideal RMHD. However, these fields only become significant at the turbulent length scale and will be introduced later through viscous dissipation. The two coupled equations remaining are:

$$\partial_t \rho\epsilon = -\sigma c(a_R T^4 - E_R) - \nabla \cdot \mathbf{F}_* \tag{3.17}$$

$$\partial_t E_R - \nabla \frac{c\lambda}{\sigma} \nabla E_R = +\sigma c(a_R T^4 - E_R), \tag{3.18}$$

where σ represents the mean opacity, $a_R = 4\sigma_B/c$ denotes the radiation constant with σ_B being the Stefan-Boltzmann constant, $\mathbf{F}_*$ stands for the irradiation flux from the star, c indicates the vacuum speed of light, and λ signifies the flux limiter. The flux limiter serves as the diffusion constant for the radiation energy density and is determined according to Levermore & Pomraning (1981). They propose the following rational approximation:

$$\lambda = \frac{2+R}{6+3R+R^2} \qquad \text{with} \tag{3.19}$$

$$R = \frac{|\nabla E_R|}{\sigma E_R}, \tag{3.20}$$

where $R = \frac{|\nabla E_R|}{\sigma E_R}$. This approximation satisfies $\lim\limits_{R\to 0} \lambda(R) = 1/3$ in the optically thick limit and $\lim\limits_{R\to\infty} \lambda(R) = 0$ in the optically thin limit. Ensuring causality, the flux-limited diffusion theory (FDT) restricts the radiative flux to never exceed c times the radiation energy density.

To establish closure between internal energy and temperature, the ideal gas approximation is employed again:

$$\rho\epsilon = \frac{p}{\Gamma - 1} = \frac{\rho k_B T}{(\Gamma - 1)\mu_g u} = c_V \rho T \tag{3.21}$$

Here, Γ denotes the adiabatic index and c_V signifies the specific heat capacity. This yields for equation (3.17):

$$c_V \partial_t \rho T = -\sigma c(a_R T^4 - E_R) - \nabla \cdot \mathbf{F}_* \,. \tag{3.22}$$

The irradiation flux is modelled as blackbody radiation times an attenuation factor:

$$\mathbf{F}_*(r) = \left(\frac{R_*}{r}\right)^2 \sigma_B T_*^4 e^{-\tau_*}. \tag{3.23}$$

Here, $e^{-\tau_*}$ accounts for the absorption of light in the stellar medium and the disk. The optical depth from the star is computed by integrating along the optical path starting at the magnetic truncation radius R_{trunc} of the star:

$$\tau_* = \int\limits_{R_{\text{trunc}}}^{r} \sigma_* dr = \tau_0 + \int\limits_{r_{\text{min}}}^{r} \sigma_* dr \,, \tag{3.24}$$

where τ_0 represents the optical depth up to the inner box radius r_{min}. This estimation is linear, $\tau_0 = \kappa_{\mathrm{gas}}\rho(r_{\mathrm{min}})(r_{\mathrm{min}} - R_{\mathrm{trunc}})$, being the product of the distance from the truncation radius of the star to the inner box radius times the mean gas opacity. The mean gas opacity is the product of the gas density at the inner box radius and the density-independent opacity of the gas κ_{gas} at the frequency of the stellar light.

The mean opacities at the typical wavelengths of the stellar light and the rim's thermal emission are defined as:

$$\begin{aligned} \sigma_* &= \rho_{\mathrm{dust}}\kappa_{\mathrm{dust}}(\nu_*) + \rho_{\mathrm{gas}}\kappa_{\mathrm{gas}} && \text{and} && (3.25)\\ \sigma &= \rho_{\mathrm{dust}}\kappa_{\mathrm{dust}}(\nu_{\mathrm{rim}}) + \rho_{\mathrm{gas}}\kappa_{\mathrm{gas}} && \text{with} && (3.26)\\ \rho_{\mathrm{dust}} &= f_{\mathrm{d2g}}\rho_{\mathrm{gas}}\,. && && (3.27) \end{aligned}$$

Here, κ_{gas} represents the density-independent opacity of the gas, which is generally frequency-dependent. For computational simplification, an average value of $\kappa_{\mathrm{gas}} = 10^{-5}, \mathrm{m^2kg^{-1}}$ is assumed for all frequencies, ensuring that the radial optical depth τ_* remains small throughout the gaseous inner disk before reaching the dust condensation front. This choice prevents excessive radiation blockage and ensures that the inner rim does not approach the star too closely.

Regarding the dust opacity, two wavelengths are significant: the stellar light's wavelength and the thermal radiation of the rim at the condensation temperature.

With these characteristic temperatures T and their corresponding wavelengths ν known the Planck mean opacities are calculated with the formula

$$\kappa_{\mathrm{Planck}} = \frac{\int_0^\infty \kappa_\nu B_\nu(T)\mathrm{d}\nu}{\int_0^\infty B_\nu(T)\mathrm{d}\nu} \tag{3.28}$$

with

$$B_\nu(\nu, T) = \frac{2h\nu^3}{c^2}\frac{1}{\exp\left(\frac{h\nu}{k_B T}\right) - 1} \tag{3.29}$$

For example for a star with a surface temperature $T_* = 10,000$ K, a dust opacity of $\kappa_{\mathrm{dust}}(\nu_*) = 210\,\mathrm{m^2kg^{-1}}$ was calculated in (Flock et al. 2016) using the frequency dependent opacity $\kappa(\nu)$ obtained by the MieX code by Wolf & Voshchinnikov (2004). Similarly, they determined an opacity value for the thermal radiation at approximately 1300 K, representing a typical dust sublimation temperature. This value is $\kappa_{\mathrm{dust}}(\nu_{\mathrm{rim}}) = 70\,\mathrm{m^2kg^{-1}}$.

The next point of interest is the dust, f_{d2g} denotes the dust-to-gas ratio of the respective densities, the calculation of which will be explained in the following section.

3.4 Dust treatment

Arguably, the most significant factor influencing the evolution of the disk is dust sublimation. Due to its higher radiation absorption compared to gas, dust experiences substantial heating from both the star and its own emitted infrared radiation, a process known as backwarming.
Additionally, even a small amount of dust can considerably attenuate the radiation that penetrates beyond it, resulting in a narrow transition zone between vapour and condensed dust. Within the three publications that comprise this thesis the treatment of the dust has evolved, these changes are explained in the following.

3.4.1 Starting point

To address the sharp boundary, the dust sublimation formula proposed by Flock et al. (2016) smooths the transition over a temperature span of 100 K, employing the hyperbolic tangent function as a modelling tool. The formula, expressed as:

$$\begin{aligned} f_{\mathrm{d2g}} &= \frac{f_{\Delta\tau}}{2}\left\{1-\tanh\left[\left(\frac{T-T_{\mathrm{ev}}}{100\,\mathrm{K}}\right)^3\right]\right\}\left\{\frac{1-\tanh(1-\tau_*)}{2}\right\} && \text{if } T > T_{\mathrm{ev}} \\ &= \frac{f_0}{2}\left\{1-\tanh(20-\tau_*)\right\}+f_{\Delta\tau} && \text{if } T < T_{\mathrm{ev}}\,, \end{aligned} \tag{3.30}$$

utilizes the dust evaporation temperature T_{ev}, the reference dust-to-gas ratio f_0, and the transition dust-to-gas ratio $f_{\Delta\tau}$.
For the dust evaporation temperature, the fitting model proposed by Isella & Natta (2005) is adopted:

$$T_{\mathrm{ev}} = 2000\,\mathrm{K}\left(\frac{\rho}{1\,\mathrm{g\,cm^{-3}}}\right)^{0.0195} \tag{3.31}$$

which characterizes the evaporation temperature's dependence on gas density for silicate grains. The transition dust-to-gas ratio $f_{\Delta\tau}$ is defined as:

$$f_{\Delta\tau} = \frac{\Delta\tau_*}{\rho_{\mathrm{gas}}\kappa_{\mathrm{dust}}(\nu_*)\Delta r} = \frac{0.3}{\rho_{\mathrm{gas}}\kappa_{\mathrm{dust}}(\nu_*)\Delta r} \tag{3.32}$$

where Δr denotes the radial size of a single grid cell. The choice of a transition optical depth $\Delta\tau_* = 0.3$ ensures the resolution of radiation absorption at the rim (Flock et al. 2016).
To maintain numerical stability, it is beneficial to impose a minimum value of $f_{d2g}^{\mathrm{min}} = 10^{-10}$, indicating virtually complete dust evaporation, and a maximum value of $f_0 = 10^{-2}$, representing the dust-to-gas reference ratio.

The dust sublimation formula illustrates a gradual formation of the dust halo for temperatures lower than T_{ev}, while it delineates the actual sublimation front for temperatures exceeding it. Notably, the formula for the dust halo reaches an upper limit of $f_{\Delta\tau}$ beyond an optical depth of one and close to the evaporation temperature. Beyond the condensation front, the dust-to-gas ratio increases with optical depth and peaks past $\tau_* = 20$.

However, if an optically thick region is heated beyond the evaporation temperature, this method experiences discontinuity. Such an occurrence was noted in (Schobert et al. 2019) as dust waves traversing the inner hole of the disk. To address this issue and provide a smoother description, (Schobert, B. N. & Peeters, A. G. 2021) introduces a new formula for the dust-to-gas ratio that is both simpler and continuous. This new formula and the introduction of dust diffusion, that enables it is presented in the next section.

3.4.2 Dust diffusion

The simplified dust-to-gas ratio is:

$$f_{\mathrm{d2g,2021}} = \frac{f_0}{2}\left\{1 - \tanh\left[\left(\frac{T - T_{\mathrm{ev}}}{\Delta T_{\mathrm{dust}}}\right)^3\right]\right\}\left\{\frac{1 - \tanh(1 - \tau_*)}{2}\right\}, \tag{3.33}$$

The substitution of $f_{\Delta\tau}$ with f_0 ensures that there is no longer a need for a distinction between temperatures above and below the evaporation point, as the second scenario outlined in equation (3.30) is now integrated into the first one. Achieving the same outcome as before, where $f_{\mathrm{d2g}} = f_0$ for low temperatures and high optical depths, is preferable with just a single continuous equation. Furthermore, a new parameter, ΔT_{dust}, is introduced to characterize the temperature range over which the transition in dust-to-gas ratio occurs. This parameter's value, generally set at $\Delta T_{\mathrm{dust}} = 100{,}\mathrm{K}$ in this work, is contingent upon the dust composition, though various values are explored in (Schobert, B. N. & Peeters, A. G. 2021).

Incorporating this new formula into the numerical framework becomes feasible by circumventing a drawback of the previous model, where all radiation would be absorbed within a single cell if the dust-to-gas ratio increases too steeply. To ensure a seamless transition, the new model now relies on the phenomenon of dust diffusion instead of a staggered dust-to-gas ratio.

To formulate a description for dust diffusion, one begins by considering the continuity equation and incorporates both the advective and diffusive flux components:

$$\frac{\partial \rho}{\partial t} = \nabla \cdot (D \nabla \rho) - \nabla \cdot (\mathbf{v}\rho) + R, \tag{3.34}$$

where ρ represents density, D stands for the diffusion coefficient, $\mathbf{v}$ denotes fluid velocity, and R encompasses any necessary source or sink terms relevant to dust description. Due to the relatively small magnitude of the diffusion term, it can initially be disregarded, allowing the equations to be solved for the purely advective scenario. This results in the hydrostatic solution for gas density (Flock et al. 2016; Schobert et al. 2019), yielding $\rho_{\text{dust}} = f_{\text{d2g}}\rho_{\text{gas}} = \rho_0$ as the most suitable approximation, considering that R is incompletely characterized. Substituting this lowest-order solution ρ_0 into the first-order terms yields:

$$\frac{\rho_{\text{diff}} - \rho_0}{\tau_{\text{diff}}} = \nabla \cdot (D\nabla\rho_{\text{diff}}) \tag{3.35}$$

$$\frac{\rho_{\text{diff}} - \rho_0}{\tau_{\text{diff}}} = D\,\nabla^2\rho_{\text{diff}} \tag{3.36}$$

$$\left[1 - D\tau_{\text{diff}}\nabla^2\right]\rho_{\text{diff}} = \rho_0, \tag{3.37}$$

where ρ_0 represents the lowest-order solution for density, accounting solely for advection, while ρ_{diff} denotes the first-order solution incorporating diffusion. A forward difference approach was employed along with a typical time scale, τ_{diff}, to approximate the derivative. In Step (3.36), it is assumed that the gradient length of the mass density is significantly smaller than the length scale over which the diffusion coefficient D varies. To incorporate diffusion, the following implicit equations are computed numerically:

$$\left[1 - D\tau_{\text{diff}}\nabla^2\right]\rho_{\text{gas,diff}} = \rho_{\text{gas}} \tag{3.38}$$

$$\left[1 - D\tau_{\text{diff}}\nabla^2\right]\rho_{\text{dust,diff}} = \rho_{\text{dust}} \tag{3.39}$$

expressed by the dust-to-gas ratio as $f_{\text{d2g}} = \rho_{\text{dust,diff}}/\rho_{\text{gas,diff}}$, ρ_{diff} denotes the respective density of dust or gas following one diffusion time step. Here, τ_{diff} represents the typical duration for dust condensation or evaporation, and D signifies the dust diffusion constant. The concept revolves around the notion that dust particles undergoing formation or destruction continue to be displaced over this period due to intrinsic turbulence or their strong coupling with the gas. One can visualize this as a form of dust memory, as its creation and annihilation are not instantaneous.

The dust diffusion constant is linked to gas diffusion through the Stokes number St (Brauer et al. 2008):

$$D_{\text{dust}} = \frac{D_{\text{gas}}}{1 + St} \approx D_{\text{gas}} \tag{3.40}$$

Given that $St < 1$ for small particles, both coefficients approximately coincide (Brauer et al. 2008), leading to $D_{\text{dust}} = \nu = \alpha c_s H$.

The typical condensation time τ_{diff} spans from 10^5 to 10^7 s (Morfill 1988). Chondrules form within a timescale of 10^5 s (Tachibana et al. 2011), while the formation timescales for corundum and hibonite range from 10^5 to 10^7 s (Nakamura et al. 2007). Silicate grain destruction occurs via sublimation and proceeds under

quasi-equilibrium conditions (Lenzuni et al. 1995), suggesting that the evaporation of silicate dust takes a comparable time to its formation.
Assuming one diffusion time as the average formation time is a useful simplification, as the exact nucleation time of dust particles and their evaporation depend on the dust's chemistry and the temperature difference between the evaporation temperature and the particle's environment. However, to encompass a wide range of possible dust compositions, a study on the impact of different formation timescales was conducted in (Schobert, B. N. & Peeters, A. G. 2021).
The references discussed above show that a one μm sized grain can survive longer than 10^5 seconds. To further strengthen this point a short concise estimate is provided that shows, that a grain can not evaporate on a timescale much shorter than the one considered. The following presents a comparison between the energy needed for evaporation and the maximum energy available to the grain within one diffusion time:
First one calculates the latent heat of evaporation of the dust grain. For all intents and purposes now the physical properties of forsterite are used. Forsterite is an olivine, that is abundant in the Earth's upper mantle and is commonly found in meteorites Hashimoto (1990), it is used here as a stand in for our generic silicate grains. First the mass of the dust grain is, assuming a radius of 1 μm,

$$m_{\text{grain}} = \frac{4}{3}\pi(1\mu\text{m})^3\rho_{\text{forsterite}} \approx 1.36 \cdot 10^{-11}\text{g} \tag{3.41}$$

with the density of forsterite being $\rho_{\text{forsterite}} = 3.25\frac{\text{g}}{\text{cm}^3}$.
The enthalpy of evaporation is

$$\Delta H_v = 543 \pm 33\frac{\text{kJ}}{\text{mol}} \tag{3.42}$$

as stated by Nagahara et al. (1994) in the abstract. This is corroborated by Chase et al. (1986), which states

$$\Delta H^0 = 139.7 \pm 8.0\frac{\text{kcal}}{\text{mol}} = 584.5 \pm 33.5\frac{\text{kJ}}{\text{mol}} \tag{3.43}$$

as the enthalpy of evaporation. Using the molar weight of forsterite, 140.69 g mol^{-1}, and the average of both values given

$$\Delta H = 4.01\,\frac{\text{kJ}}{\text{g}} \tag{3.44}$$

yields

$$\Delta E_{\text{evap}} = m_{\text{grain}}\Delta H = 5.45 \cdot 10^{-8}\text{J} \tag{3.45}$$

Next, the maximum amount of gas molecules that can pass their energy onto the dust grain within $\tau_{\text{diff}} = 10^5$ seconds is calculated. The gas molecules move at the speed of sound. The speed of sound is

$$c_\mathrm{s} = \sqrt{\frac{k_B \Gamma T}{m_g}} \tag{3.46}$$

where $m_g = 2.353u$ is the mass of a gas molecule, u is the atomic unit of mass and $\Gamma = 1.42$ is the adiabatic index. This yields for $T = 1385.7$ K, which is taken from a fiducial simulation at the $\tau = 1$ surface and also a reasonable estimate for the temperature of evaporation:

$$c_\mathrm{s} \approx 2637\,\frac{\mathrm{m}}{\mathrm{s}} \tag{3.47}$$

Multiplying this by the time yields

$$l = c_\mathrm{s}\tau_\mathrm{diff} = 2.637 \cdot 10^8\,\mathrm{m} \tag{3.48}$$

If the the gas travels this distance past the dust grain then it covers a cylindrical volume of

$$V = l\,(1\mu\mathrm{m})^2\pi \approx 8.28 \cdot 10^{-4}\mathrm{m}^3 \tag{3.49}$$

assuming the grain has a radius of 1 μm. This volume contains N gas molecules

$$N = \frac{V \rho_{gas}}{m_g} \approx 7.46 \cdot 10^{13} \tag{3.50}$$

with which the dust grain can theoretically collide, assuming a gas density $\rho_{gas} = 3.52 \cdot 10^{-13}$ g/cm^3, taken from the simulation at the point of interest (namely the lateral side of the inner rim, where the significant widening takes place). These can transmit a maximum heat of

$$\Delta E = \frac{3}{2} N k_B \Delta T = 3.1 \cdot 10^{-8}\,\mathrm{J} < \Delta E_\mathrm{evap} = 5.45 \cdot 10^{-8}\mathrm{J} \tag{3.51}$$

if the temperature difference is $\Delta T = 20$ K, which is directly taken from the simulation results in (Schobert, B. N. & Peeters, A. G. 2021).

Not only is the calculated energy that can be transferred to the dust grain in the time 10^5 seconds smaller than the energy needed to evaporate the grain, it is also overestimates the energy that can realistically be transmitted to the grain, because it neglects that the grain will receive less radiation from grains nearby as it travels to regions where dust is less abundant and will radiate more itself as it gets hotter. Also collisions are neglected, which are expected to reduce the energy flow from the gas to the dust. This estimate is a very simple picture that directly shows that the gas cannot transport enough energy onto the grain to evaporate it within 10^5 seconds.

Finally, it should be noted that 10^5 seconds must be considered a very short timescale when compared with any of the other physical processes occurring in the disk. It is, for instance two orders of magnitude smaller than a full revolution around the star at 1 AU.

3.4.3 Self shadowing disk

Previous theoretical models have included a raised inner rim with a shaded area behind it (Dullemond et al. 2001). The model depicted in (SVUFP24) exhibits multiple brightness rings in Fig. 2, therein, particularly for $9\,\mu$m. Upon comparison with Fig. 9 in (SVUFP24), it becomes apparent that the ring positions correlate with an elevated region of dust density.

The model proposed in (SVUFP24) employs a formula for the dust-to-gas ratio adapted from Flock et al. (2016), which was further simplified in Schobert, B. N. & Peeters, A. G. (2021), and now additionally improved by eliminating the optical depth dependency:

$$f_{\mathrm{d2g,2024}} = \frac{f_0}{2}\left\{1 - \tanh\left[\left(\frac{T - T_{\mathrm{ev}}}{\Delta T_{\mathrm{dust}}}\right)^3\right]\right\}, \tag{3.52}$$

where T_{ev} represents the dust evaporation temperature, $\Delta T_{\mathrm{dust}} = 100\,\mathrm{K}$ denotes the evaporation temperature range, and the reference dust-to-gas ratio is $f_0 = 10^{-2}$. For the dust evaporation temperature, the fitting model proposed by Isella & Natta (2005) is still used.

Using Eq. (3.52), one can interpret the green lines in Fig. 9 in (SVUFP24). The solid line represents the equilibrium point $f_{\mathrm{d2g}} = \frac{f_0}{2}$ or $T = T_{\mathrm{ev}}$, corresponding to an almost conical rim with a wall-like inner surface. It also exhibits a small raised rim, resulting in a shaded region between ~ 0.35 AU and ~ 0.9 AU. This is further highlighted in the dashed line, where $f_{\mathrm{d2g}} = 5 \cdot 10^{-7}$ or $T \approx T_{\mathrm{ev}} + 170\,\mathrm{K}$; it demonstrates a higher polar angle at the rim, decreasing to lower angles behind it before the disk starts to flare at approximately 0.6 AU. This dust density profile translates to the two brightness rings observed in Fig. 2 in (SVUFP24), indicative of a shaded disk. At even lower dust thresholds, the characteristic rounded-off rim connected to a density-dependent evaporation temperature becomes apparent.

3.5 Disk structure and inner rim

3.5.1 Grazing angle

This section briefly examines the radial variation of the grazing angle γ defining the angle at which stellar radiation reaches the surface of a flared accretion disk and derives the solution for the flaring disk. This solution will later serve as a boundary condition for the outer regions. The methodology outlined in the appendix of Ruden & Pollack (1991) is applied to derive the formula provided by Chiang & Goldreich (1997).

In cylindrical coordinates, with the centre of the disk lying in the $z = 0$ plane and denoting the distance from the $\hat{\mathbf{z}}$-axis as r, the height of the disk surface above the midplane is denoted by $H(r)$. Thus, the spherical radius R satisfies

$R^2 = r^2 + H^2$. Let $\hat{\mathbf{n}}_\mathbf{d}$ be the normal vector to the disk surface, $\hat{\mathbf{n}}_*$ be the normal to a surface element dA_* on the stellar surface, and $\mathbf{s} = s\hat{\mathbf{n}}$ be the ray from the element dA_* to the disk surface. The energy flux from dA_* intercepted normally by a unit area of the disk surface is given by:

$$F_\nu = B_\nu(T_*) \iint_{A_*} \frac{dA_*}{s^2} (\hat{\mathbf{n}} \cdot \hat{\mathbf{n}}_*)(-\hat{\mathbf{n}} \cdot \hat{\mathbf{n}}_\mathbf{d}), \tag{3.53}$$

assuming the star radiates like a blackbody with constant surface temperature T_*. The surface integral is evaluated using spherical coordinates with the polar axis along the line joining the center of the star and the disk surface element, and the origin in the disk surface element. The polar angle is Ψ and the azimuthal angle is Φ. This geometry is shown in figure 3.1. The integration is done over concentric half annuli on the stellar surface. The normal vectors expressed in these coordinates are:

$$\hat{\mathbf{n}}_\mathbf{d} = -\frac{\frac{dH}{dr}}{\sqrt{1 + \left(\frac{dH}{dr}\right)^2}} \hat{\mathbf{n}}_\mathbf{x} + \frac{1}{\sqrt{1 + (\frac{dH}{dr})^2}} \hat{\mathbf{n}}_\mathbf{z} \tag{3.54}$$

$$\begin{aligned} \hat{\mathbf{n}} = & \left[\frac{r}{R}\cos(\Psi) + \frac{H(r)}{R}\sin(\Psi)\cos(\Phi)\right] \hat{\mathbf{n}}_\mathbf{x} \\ & - \sin(\Psi)\sin(\Phi)\hat{\mathbf{n}}_\mathbf{y} + \left[\frac{H(r)}{R}\cos(\Psi) - \frac{r}{R}\sin(\Psi)\cos(\Phi)\right] \hat{\mathbf{n}}_\mathbf{z}. \end{aligned} \tag{3.55}$$

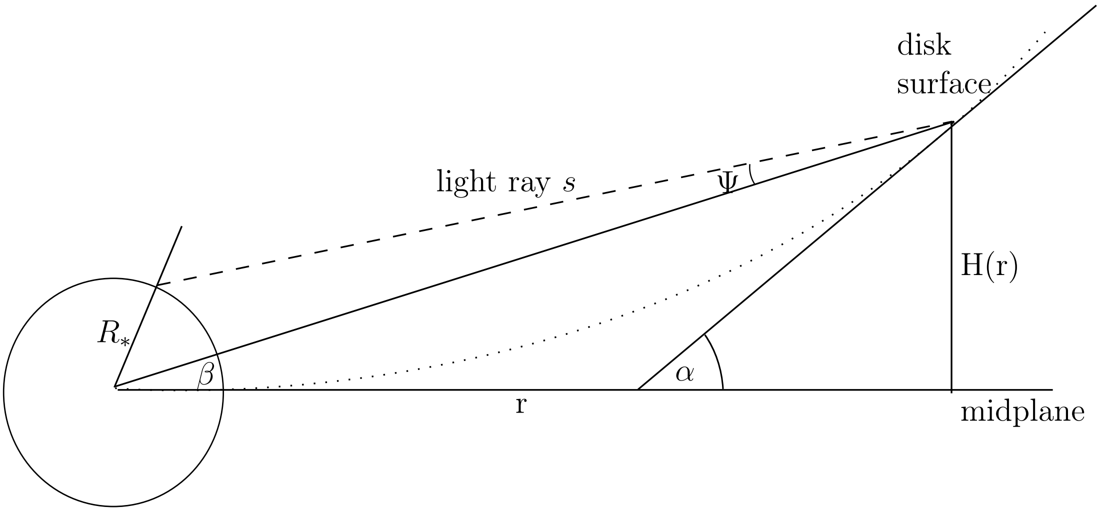

Figure 3.1: Depiction of coordinates, the dotted line represents the surface of the protostellar disk, the dashed line is the path of a light ray that is also used as the polar axis for the spherical coordinates.

The scalar product of the normal vectors is given by:

$$
\begin{aligned}
-\hat{\mathbf{n}}\cdot\hat{\mathbf{n}}_{\mathbf{d}} =& \frac{\frac{dH}{dr}}{\sqrt{1+\left(\frac{dH}{dr}\right)^2}}\left[\frac{r}{R}\cos(\Psi)+\frac{H(r)}{R}\sin(\Psi)\cos(\Phi)\right] \\
&-\frac{1}{\sqrt{1+(\frac{dH}{dr})^2}}\left[\frac{H(r)}{R}\cos(\Psi)-\frac{r}{R}\sin(\Psi)\cos(\Phi)\right] \\
=& \frac{\tan(\alpha)}{\sqrt{1+(\tan(\alpha))^2}}\left[\cos(\beta)\cos(\Psi)+\sin(\beta)\sin(\Psi)\cos(\Phi)\right] \\
&-\frac{1}{\sqrt{1+(\tan(\alpha))^2}}\left[\sin(\beta)\cos(\Psi)-\cos(\beta)\sin(\Psi)\cos(\Phi)\right] \\
=& \sin(\alpha)\left[\cos(\beta)\cos(\Psi)+\sin(\beta)\sin(\Psi)\cos(\Phi)\right] \\
&-\cos(\alpha)\left[\sin(\beta)\cos(\Psi)-\cos(\beta)\sin(\Psi)\cos(\Phi)\right] \\
=& \cos(\Psi)[\sin(\alpha)\cos(\beta)-\cos(\alpha)\sin(\beta)] \\
&+\sin(\Psi)\cos(\Phi)[\sin(\alpha)\sin(\beta)+\cos(\alpha)\cos(\beta)] \\
=& \cos(\Psi)\sin(\alpha-\beta)+\sin(\Psi)\cos(\Phi)\cos(\alpha-\beta),
\end{aligned}
$$

where the following angles have been defined:

$$
\tan(\alpha) = \frac{dH}{dr} \tag{3.56}
$$

$$
\tan(\beta) = \frac{H}{r} \tag{3.57}
$$

$$
\implies \cos(\beta) = \frac{r}{R} \quad \text{and} \quad \sin(\beta) = \frac{H}{R}.
$$

Now the first part of the integrand is transformed accordingly

$$
\begin{aligned}
\frac{dA_*}{s^2}(\hat{\mathbf{n}}\cdot\hat{\mathbf{n}}_*) &= \frac{1}{s^2}d\hat{\mathbf{A}}_*\cdot\hat{\mathbf{n}} \\
&= \frac{1}{s^2}d\hat{\mathbf{A}}_{\text{ray}}\cdot\hat{\mathbf{n}} \\
&= \frac{1}{s^2}dA_{\text{ray}}(\hat{\mathbf{n}}\cdot\hat{\mathbf{n}}) \\
&= \frac{1}{s^2}s^2\sin(\Psi)d\Psi d\Phi \\
&= \sin(\Psi)d\Psi d\Phi.
\end{aligned}
$$

This significant simplification arises from a specific choice of coordinates. The crucial step involves transitioning the surface parameterization from $d\hat{\mathbf{A}}_*$ to $d\hat{\mathbf{A}}_{\text{ray}}$.

This transition ensures that the same area is covered after integration, while accounting for the viewing angle. The integration utilizes spheres with a radius identical to s for each infinitesimal half ring, with their normal vectors matching the ray direction $\hat{\mathbf{n}}$.

The following step involves determining the boundaries of the new integral $\Psi_{\max}$ and $\Phi_{\max}$. The polar angle reaches its maximum at the star's edge, indicating that

$$\sin(\Psi_{\max}) = \frac{R_*}{R} = \frac{R_*}{\sqrt{r^2+H^2}} = \frac{R_*}{r\sqrt{1+\left(\frac{H^2}{r^2}\right)}} = \frac{R_*}{r} + O\left(\left(\frac{H}{r}\right)^2\right) \tag{3.58}$$

and $\Phi_{\max}$ is a non-trivial function of Ψ and r, but its exact form isn't necessary. One can reasonably approximate $\Phi_{\max} = \frac{\pi}{2}$ by integrating the azimuthal angle from $-\Phi_{\max} = \frac{\pi}{2}$ to $\Phi_{\max} = \frac{\pi}{2}$, forming precisely a half ring. The assumption is that the lower half of the star remains unseen from the upper disk surface. Now, solving the integral and integrating over all frequencies yields the total flux on the disk:

$$\begin{aligned}
F_d = &\int_0^{\infty} d\nu B_\nu(T_*) \int_0^{\Psi_{\max}} \sin(\Psi) d\Psi \int_{-\Phi_{\max}}^{\Phi_{\max}} d\Phi [\cos(\Psi)\sin(\alpha-\beta) \\
&+ \sin(\Psi)\cos(\Phi)\cos(\alpha-\beta)] &(3.59)\\
=&2\int_0^{\infty} d\nu B_\nu(T_*) \int_0^{\Psi_{\max}} \sin(\Psi) d\Psi \int_0^{\Phi_{\max}} d\Phi [\cos(\Psi)\sin(\alpha-\beta) \\
&+ \sin(\Psi)\cos(\Phi)\cos(\alpha-\beta)] &(3.60)\\
=&2\frac{1}{\pi}\sigma T_*^4 \int_0^{\Psi_{\max}} d\Psi \sin(\Psi)\left[\frac{\pi}{2}\cos(\Psi)\sin(\alpha-\beta) + \sin(\Psi)\cos(\alpha-\beta)\right] &(3.61)\\
=&\sigma T_*^4 \left[\frac{1}{2}\sin^2(\Psi_{\max})\sin(\alpha-\beta)\right. \\
&\left.+\frac{1}{\pi}\cos(\alpha-\beta)(\Psi_{\max} - \sin(\Psi_{\max})\cos(\Psi_{\max}))\right]. &(3.62)
\end{aligned}$$

In the limit where $H \ll r$ and $R_* \ll r$, the functions in $\Psi_{\max}$ and $\alpha - \beta$ can be Taylor-expanded, retaining only the lowest-order terms in these quantities. Assuming $\alpha - \beta \ll 1$ implies the disk doesn't flare excessively. This results in the flux:

$$\begin{aligned}
F_d &= \sigma T_*^4 \left[\frac{1}{2}\sin^2(\Psi_{\max})\sin(\alpha-\beta) + \frac{1}{\pi}\cos(\alpha-\beta)(\Psi_{\max} - \frac{1}{2}sin(2\Psi_{\max}))\right] \\
&\approx \sigma T_*^4 \left[\frac{1}{2}\sin^2(\Psi_{\max})(\alpha-\beta) + \frac{1}{\pi}(\Psi_{\max} - \Psi_{\max} + \frac{2}{3}\Psi_{\max}^3)\right] \\
&\approx \sigma T_*^4 \left[\frac{1}{2}\left(\frac{R_*}{r}\right)^2\left(\frac{dH}{dr} - \frac{H}{r}\right) + \frac{2}{3\pi}\left(\frac{R_*}{r}\right)^3\right] \\
&= \sigma T_*^4 \left[\frac{1}{2}\left(\frac{R_*}{r}\right)^2 r\frac{d}{dr}\left(\frac{H}{r}\right) + \frac{2}{3\pi}\left(\frac{R_*}{r}\right)^3\right]. \qquad (3.63)
\end{aligned}$$

Now, defining an effective angle γ under which the star's radiation impinges on the disk at radius r:

$$F_d = \sigma T_*^4 \frac{\gamma}{2}\left(\frac{R_*}{r}\right)^2 \qquad (3.64)$$

This leads to the grazing angle γ:

$$\gamma = \frac{4}{3\pi}\frac{R_*}{r} + r\frac{d}{dr}\left(\frac{H}{r}\right). \qquad (3.65)$$

This expression is utilized to derive the flaring disk approximation by equating emitted and absorbed fluxes:

$$\begin{aligned}
F_* &= F_{\text{disk}} & (3.66)\\
\epsilon r^2 \sigma_B T^4 &= \gamma R_*^2 \sigma_B T_*^4 & (3.67)\\
T^4 &= \gamma\frac{1}{\epsilon}\left(\frac{R_*}{r}\right)^2 T_*^4, & (3.68)
\end{aligned}$$

where ϵ represents the ratio between emission and absorption efficiencies, r denotes the radial distance, σ_B stands for the Stefan-Boltzmann constant, $T(r)$ signifies the height-averaged disk temperature, R_* indicates the stellar radius, and T_* denotes the stellar surface temperature. Subsequently, (3.65) is employed, with the initial term disregarded due to the radii of interest being significantly larger than R_*, and (3.13) is utilized for H, as the pressure scale height offers a suitable approximation for the disk's height:

$$\begin{aligned}
T^4 &= \frac{T_*^4 R_*^2}{\epsilon\, r}\frac{d}{dr}\left(\frac{H}{r}\right) & (3.69)\\
&= \frac{T_*^4 R_*^2}{\epsilon\, r}\frac{d}{dr}\left(\sqrt{\frac{k_B T r}{\mu_g u G M_*}}\right) & (3.70)\\
&= \frac{T_*^4 R_*^2}{\epsilon\, r}\sqrt{\frac{k_B}{\mu_g u G M_*}}\left(\frac{1}{2}T^{0.5}r^{-0.5} + \frac{1}{2}T^{-0.5}r^{0.5}\frac{dT}{dr}\right). & (3.71)
\end{aligned}$$

Once again, the initial term can be disregarded for large distances r, resulting in:

$$T^{4.5} = \frac{T_*^4 R_*^2}{2\epsilon} \sqrt{\frac{k_B}{\mu_g u G M_*}} r^{-0.5} \frac{dT}{dr} \tag{3.72}$$

$$r^{0.5} dr = C\, T^{-4.5} dT \tag{3.73}$$

$$\frac{2}{3} dr^{1.5} = -\frac{2}{7} C\, dT^{-3.5} \tag{3.74}$$

$$r^{1.5} \propto T^{-3.5} \tag{3.75}$$

$$T \propto r^{-3/7}, \tag{3.76}$$

where C encompasses all constants. Thus, at significant distances from the star, the dominant factor is the flaring term, affirming the correctness of the flaring disk solution with $T(r) \propto r^{-3/7}$. This serves as a boundary condition for the outer radii in the simulation.

3.5.2 Inner rim

In (Schobert, B. N. & Peeters, A. G. 2021) the radial position and height of the inner rim is compared against a theoretical model described in (Dullemond et al. 2001). For better understanding this theoretical model is briefly explained here. Dullemond et al. (2001) describe a cylindrical inner rim, a inner hole around the star, where dust is fully evaporated and only gas exists.

In (Dullemond et al. 2001), the rim position was defined as the radius where radiative equilibrium is attained at the evaporation temperature:

$$R_{\text{rim}} = \left(\frac{L_*}{4\pi T_{\text{rim}}^4 \sigma_B} \right)^{1/2} \left(1 + \frac{H_{\text{rim}}}{R_{\text{rim}}} \right). \tag{3.77}$$

Here, L_* represents stellar luminosity, T_{rim} stands for the evaporation temperature at the rim, σ_B denotes the Stefan-Boltzmann constant, and $H_{\text{rim}} = \chi_{\text{rim}} h_{\text{rim}}$ represents the height of the disk at the rim, which is χ_{rim} times the pressure scale height at that location. The second factor in this equation accounts for the radiation emitted from the opposing disk area.

To compute χ_{rim}, a vertical Gaussian density profile is assumed, along with a linear relationship of $H(R)/R$ with a slope of $-1/8$ (refer to section A3 in (Dullemond et al. 2001), this slope is an estimate). In this context, the surface height is defined as the height at which the optical depth τ of the rim on a radially outward directed ray exceeds 1:

$$\begin{aligned} \tau(H_{\text{rim}}) &= \int_{R_{\text{rim}}}^{\infty} \rho(R, H_{\text{rim}}) \kappa_{\text{dust}}(T_*) f_{\text{d2g}} dR = 1 \\ \text{erf}\left(\frac{\chi_{\text{rim}}^{\text{theo}}}{\sqrt{2}} \right) &= 1 - \frac{1}{4\Sigma(R_{\text{rim}}) \kappa_{\text{dust}}(T_*) f_{\text{d2g}}}. \end{aligned} \tag{3.78}$$

In this context, the symbol erf(x) represents the error function, and Σ represents the gas surface density of the disk. From the formulae above it is possible to calculate the rim radius and the disk height, or its ratio with the pressure scale height, by applying them iteratively until the values converge, if Σ is a function of R_{rim}. If Σ is chosen to be constant, then no iteration is necessary.

3.5.3 Disk structure

The structure of a protoplanetary disk can be sectioned into four distinct regions as identified in (Flock et al. 2016; Ueda et al. 2017), it is advantageous to identify them in an early example simulation, with fixed surface density of 100 gcm^{-2}, no dust diffusion and no accretion heating, the `S100` case. This case is shown in Fig. 3.2.

The first region comprises a **dust-free inner zone** following the optically thin gas temperature and is situated inward of 0.3 AU.

Next is the **dust halo**, where the dust-to-gas ratio gradually increases before reaching the condensation temperature at 0.5 AU.

Following this is the **condensation front** enveloping the third region, formed by the rounded-off rim. At its centre lies an active zone where MRI is possible. This stands in contrast to a dead zone, where temperatures are too low for MRI (see following section) to occur.

The fourth and outermost region is the outer disk, growing colder with radial distance and situated at optical depths beyond unity. Complete thermal equilibrium is achieved, the temperature within the disk is vertically constant. This zone is also called the **dead zone**, because it can not sustain MRI.

Even further out than visible in Fig. 3.2 the disk becomes optically thin again as the surface density decreases. In this possible fifth region it can be ionized by interstellar radiation or far-UV radiation from the jet of the central star and be potentially MRI active again, marking the end of the dead zone.

3.6 Turbulence and MRI

Incorporating the influences of accretion and viscous heating necessitates estimating the viscosity within the disk. This task presents challenges due to various turbulence-inducing instabilities in the disk, notably the magnetorotational instability or MRI (Velikhov 1959; Chandrasekhar 1960; Balbus & Hawley 1998).

A widely employed method to address this complexity is the α-viscosity prescription introduced by Shakura & Sunyaev (1973). The concept parallels the kinematic ideal gas viscosity, which is proportional to the product of the mean free path of molecules and their thermal velocity:

$$\nu_{\text{ideal}} \propto \lambda_{\text{free}} v_{\text{therm}} , \tag{3.79}$$

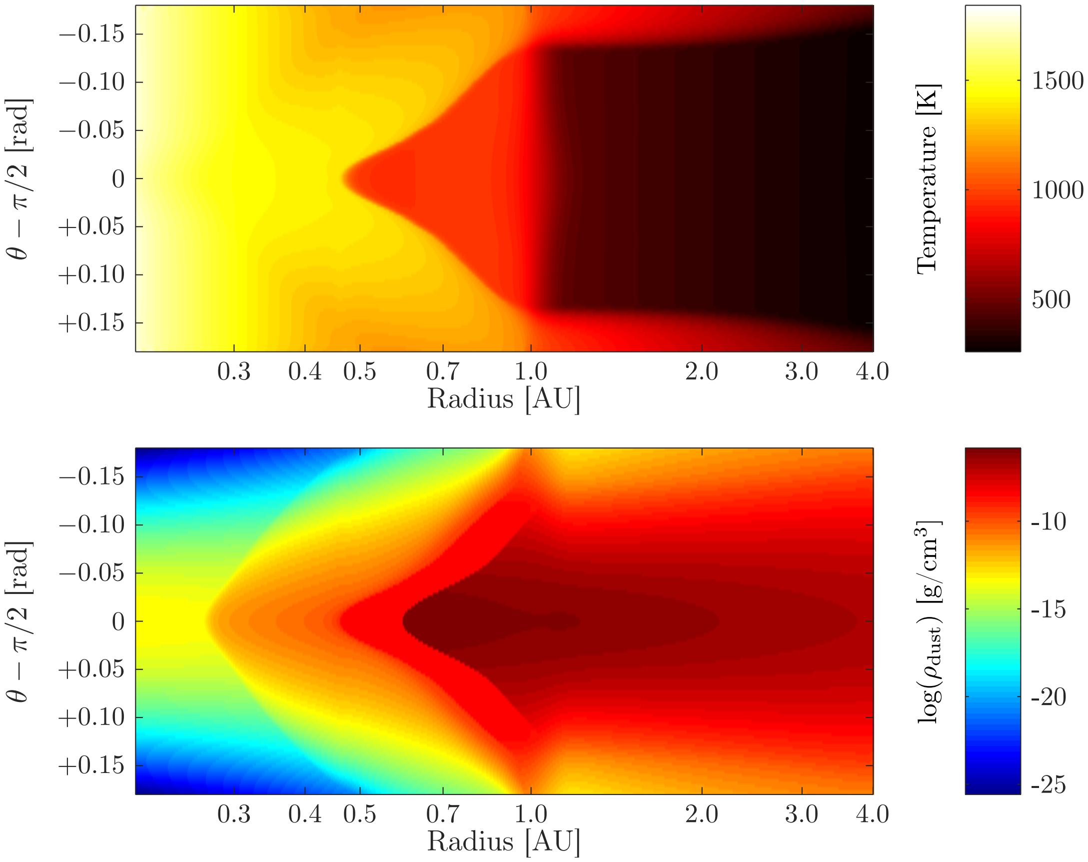

Figure 3.2: 2D profiles of temperature (top) and the logarithm of the dust density in g/cm^3 to the base 10 (bottom) for the `S100` case. The y-axis is the polar angle in rad offset by $\pi/2$ and the x-axis the radial distance in AU.

Similarly, the turbulent viscosity ν_t is approximated by considering the standard length scale of eddies in a turbulent flow. Although this length L exceeds the molecular mean free path, it remains smaller than the pressure scale length H, roughly corresponding to the height of the disk. Additionally, the velocities of these eddies are notably slower than the speed of sound c_s. Combining these factors and introducing a dimensionless constant $\alpha < 1$ yields the expression for viscosity:

$$\begin{aligned} \nu_t &= \alpha H c_s && (3.80) \\ &= \frac{\alpha c_s^2}{\Omega} \, . && (3.81) \end{aligned}$$

Here, eq. (3.11) was utilized to express the kinematic turbulent viscosity ν_t in terms of the speed of sound c_s squared divided by the Keplerian rotation frequency Ω. Typically, the constant α falls within the range of 10^{-1} for strong turbulence to 10^{-3} for weaker turbulence. Shakura & Sunyaev (1973) argued that for $\alpha > 1$, turbulence must be supersonic, resulting in rapid plasma heating and consequently reducing α to $\alpha \leq 1$.

Having determined the viscosity, it becomes feasible to compute the surface density and examine the impact of viscous dissipation on temperature.

The magnitude of the viscosity is determined by the mechanism that drives the turbulence. Of specific interest is the magneto-rotational instability (Velikhov 1959; Chandrasekhar 1960; Balbus & Hawley 1998), because it sustains α values between 0.1 and 10^{-2} (Flock et al. 2017) in a sufficiently ionized medium. In an unionised medium different hydrodynamical processes, such as shear flow, lead to turbulence, but at a smaller scale of $\alpha = 10^{-3}$ to 10^{-5}. This stark difference explains why the dead zone is described as such, it exhibits drastically less dynamic turbulence as MRI active zones, therefore it is comparatively dead.

3.7 Steady state accretion

The surface density Σ is characterized by employing the steady thin disk approximation. This implies that the disk is cool, nearly Keplerian, axisymmetric ($\partial_\phi = 0$), and $v_z = 0$. To streamline the derivation, it is conducted in cylindrical coordinates. However, since the solution is integrated over the height z, it is equally applicable for spherical coordinates. In a steady disk, $\partial_t = 0$, and the mass accretion rate $\dot{M}$ remains constant throughout the disk. The derivation in this section closely follows Clarke & Carswell (2009). With these assumptions, the continuity equation can be manipulated as follows:

$$\partial_t \rho + \nabla \cdot (\rho \mathbf{v}) = 0 \tag{3.82}$$

$$\frac{1}{r}\partial_r(r\rho v_r) = 0 \tag{3.83}$$

$$\partial_r(r\Sigma v_r) = 0 \tag{3.84}$$

$$r\Sigma v_r = C_1. \tag{3.85}$$

In the second step, the integration over z was performed, followed by integration over the radius r in the third step. The integration constant C_1 can be determined by considering the mass accretion rate through a ring, given by $\dot{M} = -2\pi r\Sigma v_r$. This leads to $C_1 = -\dot{M}/2\pi$. The subsequent equation to consider is the ϕ component of the Navier-Stokes equation:

$$\rho\left(\partial_t \mathbf{v} + (\mathbf{v}\cdot\nabla)\mathbf{v}\right) = \nabla\cdot\boldsymbol{\sigma} - \rho\nabla\Phi \tag{3.86}$$

$$\rho\left(v_r\partial_r v_\phi + \frac{v_r v_\phi}{r}\right) = \partial_r(\eta\partial_r v_\phi) + \partial_z(\eta\partial_z v_\phi) + \frac{1}{r}\partial_r(\eta v_\phi) - \frac{\eta v_\phi}{r^2}, \tag{3.87}$$

which is also integrated over z to obtain

$$\Sigma\left(v_r\partial_r v_\phi + \frac{v_r v_\phi}{r}\right) = \partial_r(\nu\Sigma\partial_r v_\phi) + \frac{1}{r}\partial_r(\nu\Sigma v_\phi) - \frac{\nu\Sigma v_\phi}{r^2}. \tag{3.88}$$

Here, $\eta = \rho\nu$ represents the dynamic viscosity, expressed in terms of kinematic viscosity and density. Consequently, after integration, one obtains Σ, the surface density, and ν, which becomes the density-weighted average value of kinematic viscosity over z. Integrating over z implicitly disregards any variation of v_r and v_ϕ with z, although any such dependence would likely be minimal. The term involving $\partial_z^2 v_\phi$ disappears upon integration, under the assumption that $\eta\partial_z v_\phi$ equals 0 at the top and bottom surfaces of the disk. Utilizing $\Omega = v_\phi/r$, the sum of (3.84)$\cdot v_\phi$ and (3.88)$\cdot r$ can be expressed as:

$$\frac{1}{r}\partial_r(\Sigma r^2 v_\phi v_r) = \frac{1}{r}\partial_r\left(\nu\Sigma r^3\frac{d\Omega}{dr}\right). \tag{3.89}$$

It follows by integration over r:

$$\Sigma r^3\Omega v_r - \nu\Sigma r^3\frac{d\Omega}{dr} = C_2 \tag{3.90}$$

with the integration constant C_2. Determining its value necessitates finding an inner boundary condition. As matter accretes, it flows onto the surface of the star, increasing its velocity as it moves inward. However, the surface of the star rotates with an angular velocity Ω_* lower than the Keplerian velocity, ensuring stability. This implies that the angular velocity attains a maximum, where $\frac{d\Omega}{dr} = 0$, likely located near the stellar surface. Assuming this point is at $r = R_*$ and $\Omega = \Omega_K(R_*)$ there, the condition is:

$$\Sigma R_*^3 \Omega_K v_r = -\frac{\dot{M}}{2\pi} R_*^2 \Omega_K \tag{3.91}$$

$$= -\frac{\dot{M}}{2\pi}(GM_* R_*)^{0.5} = C_2. \tag{3.92}$$

This yields

$$-\frac{\dot{M}}{2\pi}(GM_* r)^{0.5} - \nu \Sigma r^3 \frac{d\Omega}{dr} = -\frac{\dot{M}}{2\pi}(GM_* R_*)^{0.5} \tag{3.93}$$

$$\frac{3}{2}\nu\Sigma(GM_* r)^{0.5} = \frac{\dot{M}}{2\pi}[(GM_* r)^{0.5} - (GM_* R_*)^{0.5}] \tag{3.94}$$

$$\Sigma = \frac{\dot{M}}{3\pi\nu}\left[1 - \left(\frac{R_*}{r}\right)^{0.5}\right] \approx \frac{\dot{M}}{3\pi\nu} \tag{3.95}$$

at a significant distance from the star, the condition holds true. Here, $\dot{M}$ represents the accretion rate, r denotes the radial distance, and ν stands for the kinematic viscosity. To estimate the viscosity, one utilizes the α-viscosity prescription introduced by Shakura & Sunyaev (1973) in the preceding section:

$$\nu_t = \alpha H c_s = \frac{\alpha c_s^2}{\Omega}. \tag{3.96}$$

The pressure scale height $H = c_s/\Omega$ was employed to express the kinematic turbulent viscosity ν_t in terms of the local speed of sound c_s and the Keplerian rotation frequency $\Omega = \sqrt{GM_*/R^3}$.
Given a specific viscosity, it becomes feasible to compute the surface density using the formula:

$$\Sigma = \frac{\dot{M}\Omega}{3\pi\alpha c_s^2}. \tag{3.97}$$

In (SVUFP24) the simulation box was closer to the star, than in the previous works, so the approximation in eq. (3.95) was not used. Instead R_* was replaced by R_{trunc} the magnetic truncation radius of the star, because the maximum of the rotation frequency can safely be assumed to be further from the star then the truncation radius (which is about 3 to 5 stellar radii) (Calvet & Gullbring 1998).

3.8 Accretion heating

The initial equation in the radiative hydrodynamics section (3.17) outlines the internal energy density of the gas, yet it is incomplete. A complementary equation

in general fluid dynamics for the internal energy will be introduced in this section, as it incorporates additional physical processes.
The total energy equation of a fluid, as derived in works such as (Johnson 1998), is:

$$\rho D_t \left(\tfrac{1}{2}v^2 + \epsilon\right) = -\nabla \cdot \mathbf{q} + \nabla \cdot [\boldsymbol{\sigma} \cdot \mathbf{v}] \qquad \text{with} \tag{3.98}$$

$$\boldsymbol{\sigma} = -p\mathbf{I} + \eta\left(\nabla\mathbf{v} + (\nabla\mathbf{v})^{\mathrm{t}}\right) - (\tfrac{2}{3}\eta - \kappa)(\nabla \cdot \mathbf{v})\mathbf{I} \qquad \text{and} \tag{3.99}$$

$$\mathbf{q} = -k\nabla T\,. \tag{3.100}$$

In this expression, D_t denotes the substantial or total derivative with respect to time, defined in this context as $\rho D_t X = \partial_t \rho X + (\rho\mathbf{v} \cdot \nabla X)$. The tensor $\boldsymbol{\sigma}$ represents the stress tensor, η stands for the dynamic viscosity, κ represents the bulk viscosity, $\mathbf{I}$ denotes the identity matrix of dimension three, $\mathbf{q}$ signifies the heat flux, and k denotes the thermal conductivity.
To obtain the internal energy density, it is necessary to subtract the mechanical energy, which can be derived from the Navier-Stokes equation by taking the inner product with the velocity vector $\mathbf{v}$:

$$\rho\, D_t\mathbf{v} = \nabla \cdot \boldsymbol{\sigma} \tag{3.101}$$

$$\mathbf{v} \cdot \rho\, D_t\mathbf{v} = \mathbf{v} \cdot (\nabla \cdot \boldsymbol{\sigma}) \tag{3.102}$$

$$\rho\, D_t\left(\tfrac{1}{2}v^2\right) = \mathbf{v} \cdot (\nabla \cdot \boldsymbol{\sigma}). \tag{3.103}$$

Now taking the difference yields

$$\rho\, D_t\epsilon = -\nabla \cdot \mathbf{q} + \nabla \cdot [\boldsymbol{\sigma} \cdot \mathbf{v}] - \mathbf{v} \cdot (\nabla \cdot \boldsymbol{\sigma}) \tag{3.104}$$

$$= -\nabla \cdot \mathbf{q} + (\boldsymbol{\sigma} \colon \nabla\mathbf{v}) \tag{3.105}$$

in a coordinate-independent notation, where : signifies a double contraction.
Now, assuming an ideal gas $\epsilon = c_V T$ and constant thermal conductivity, this can be expressed as:

$$\rho c_V D_t T = k\nabla^2 T + (\boldsymbol{\sigma} \colon \nabla\mathbf{v}) \tag{3.106}$$

$$= k\nabla^2 T + \Theta - p(\nabla \cdot \mathbf{v}) \qquad \text{with} \tag{3.107}$$

$$\Theta = \boldsymbol{\sigma} \colon \nabla\mathbf{v} + p(\nabla \cdot \mathbf{v}). \tag{3.108}$$

Here Θ is the dissipation function and it can be written in Gibb's notation as

$$\Theta = \frac{1}{2}\eta\left(\left[\nabla\mathbf{v} + (\nabla\mathbf{v})^{\mathrm{t}} - \tfrac{2}{3}(\nabla \cdot \mathbf{v})\mathbf{I}\right] \colon \left[\nabla\mathbf{v} + (\nabla\mathbf{v})^{\mathrm{t}} - \tfrac{2}{3}(\nabla \cdot \mathbf{v})\mathbf{I}\right]\right) + \kappa(\nabla \cdot \mathbf{v})^2. \tag{3.109}$$

As this formula remains coordinate-independent, calculating the dissipation function Θ in spherical coordinates is a straightforward task. The requisite metric is:

$$\mathbf{g} = \begin{bmatrix} 1 & 0 & 0 \\ 0 & r^2 & 0 \\ 0 & 0 & r^2 \sin^2\theta \end{bmatrix} \tag{3.110}$$

With this, one can compute all the required Christoffel symbols for the covariant derivatives and derive the expression for Θ. Given the lengthiness of the calculation, only the final result is presented here, which is also available in Johnson (1998):

$$\begin{aligned} \Theta = \eta \Bigg[& 2(\partial_r v_r)^2 + 2\left(\frac{1}{r}\partial_\theta v_\theta + \frac{v_r}{r}\right)^2 + 2\left(\frac{1}{r\sin\theta}\partial_\phi v_\phi + \frac{v_r + v_\theta\cot\theta}{r}\right)^2 \\ & + \left(\frac{1}{r}\partial_\theta v_r + r\partial_r\left(\frac{v_\theta}{r}\right)\right)^2 + \left(\frac{1}{r\sin\theta}\partial_\phi v_\theta + \frac{\sin\theta}{r}\partial_\theta\left(\frac{v_\phi}{\sin\theta}\right)\right)^2 \\ & + \left(r\partial_r\left(\frac{v_\phi}{r}\right) + \frac{1}{r\sin\theta}\partial_\phi v_r\right)^2\Bigg] - \left(\tfrac{2}{3}\eta - \kappa\right)\left(\frac{1}{r^2}\partial_r(r^2 v_r)\right. \\ & \left. + \frac{1}{r\sin\theta}\partial_\theta(v_\theta\sin\theta) + \frac{1}{r\sin\theta}\partial_\phi v_\phi\right)^2 . \end{aligned} \tag{3.111}$$

In the context of accretion disks many of these terms become zero, as seen in the following.

The substantial turbulent viscosity, as discussed in section 3.6, indicates the necessity of considering heat dissipation in the energy balance, particularly for active disks. Unlike in (Flock et al. 2016), this effect is accounted for in the internal energy without solving the full set of hydrodynamic equations.

Due to the orientation of the coordinate system along the rotational axis, there exists a strong ordering of velocities $v_\phi \gg v_\theta, v_r$. Furthermore, owing to the spherical symmetry, $\partial_\phi = 0$ and $\partial_\theta = 0$. Consequently, terms of the form $\partial_r v_\phi$ are the only ones remaining and are naturally the dominant ones.

Subsequently, the dissipation function simplifies to:

$$\Theta = \eta\left(r\partial_r\left(\frac{v_\phi}{r}\right)\right)^2 \tag{3.112}$$

$$= \eta(r\partial_r\Omega)^2 \tag{3.113}$$

and further the term $-p(\nabla\cdot\mathbf{v})$ vanishes. This yields an additional term in (3.17):

$$\partial_t\rho\epsilon = -\sigma c(a_R T^4 - E_R) - \nabla\cdot\mathbf{F}_* + Q_{\mathrm{heat}}. \tag{3.114}$$

The new term Q_{heat} is the dissipation function

$$Q_{\mathrm{heat}} = \rho\nu_t\left[r\,\partial_r\,\Omega\right]^2 \tag{3.115}$$

with the angular rotation frequency $\Omega(r)$. It describes the heating of the matter through viscous interaction and the effect of this new term is discussed in the first publication (Schobert et al. 2019).

3.9 Thermal conduction

Another term appearing in the energy equation is thermal conduction. Since momentum eddy diffusivity and heat transfer eddy diffusivity are related through the turbulent Prandtl number $Pr_t = c_p \nu_t \rho / k_t = \mathcal{O}(1)$, the impact of thermal conduction should be comparable to that of viscous dissipation and therefore warrants consideration. This addition is entirely new to this model and plays an important role in the regime of high accretion rates explored in this thesis. Here, k_t represents the turbulent thermal conductivity and c_p denotes the specific heat at constant pressure. This leads to the expression for k_t:

$$k_t = \frac{\rho \nu_t \Gamma c_V}{Pr_t}, \tag{3.116}$$

utilizing $c_p = \Gamma c_v$ with the adiabatic index Γ, one obtains another additional term in (3.17):

$$\partial_t \rho \epsilon = -\sigma c (a_R T^4 - E_R) - \nabla \cdot \mathbf{F}_* + Q_{\text{heat}} + Q_{\text{cond}} \tag{3.117}$$

with

$$Q_{\text{cond}} = k_t \nabla^2 T \,. \tag{3.118}$$

The effects of thermal conduction are also discussed in the first publication (Schobert et al. 2019).

3.10 Spectral energy distribution (SED)

A spectral energy distribution (SED) illustrates the energy emitted by an object across various wavelengths. In case of an accretion disk it includes the contribution from central star and from the disk itself. The stellar spectrum is approximately a black body spectrum with the star's effective temperature. The contribution of the disk has also a continuum component related to its surface temperature in the near- and mid-infrared and additionally line features.

These will show, depending on the specific dust composition, features at characteristic wavelengths, i.e. the silicate feature at ca. 10 μm. Other materials found in protoplanetary disks, that produce prominent peaks are polycyclic aromatic hydrocarbons (PAH) (Habart, E. et al. 2004) and in some cases diamonds (Goto et al. 2009).

Apart from the dust composition the SED also gives insight into the geometry and temperature surface profile of the disk through its continuum component. A hotter inner rim will emit at shorter wavelengths compared to a colder inner rim. However, the SED alone can not provide a complete picture of the disk, multiple geometry and temperature profile combinations can lead to the same SED. Therefore, it is necessary to spatially resolve the disk, but often direct imaging is impossible due to technical limitations of the telescopes. Then a visibility curve can provide additional information about the configuration of the disk, this is explained in the following section.

3.11 Visibility

The interferometric visibility, also referred to as interference visibility or fringe visibility, is a metric indicating the contrast of interference in any system experiencing wave superposition. It is often used in astrophysics to gain spatial information about objects, that otherwise could not be spatially resolved. A prominent example was the imaging of the supermassive black hole M87* (Collaboration et al. 2019).
Visibility can be computed from the mutual coherence function:

$$\Gamma_{12}(u,v) = \int\int_{\text{source}} I(l,m)\exp(-2\pi i(ul - vm))\,\mathrm{d}l\,\mathrm{d}m, \tag{3.119}$$

which is defined as the Fourier transform of intensity I according to the van Cittert–Zernike theorem (van Cittert 1934; Zernike 1938). Here, (u,v) is the angular coordinates vector in the Fourier plane and (l,m) is the angular coordinate vector in the plane of the sky. The complex visibility $\mu(u,v)$ is normalized as follows:

$$\mu(u,v) = \frac{\Gamma_{12}(u,v)}{\Gamma_{12}(0,0)} \tag{3.120}$$

However, the complex visibility cannot be directly measured for near- and mid-infrared wavelengths; only the absolute value can be determined. Under the assumption of cylindrical symmetry, it is convenient to employ the radial distance in phase space, or baseline, $B = \sqrt{u^2+v^2}$:

$$V(B) = \left|\mu(\sqrt{u^2+v^2})\right| \tag{3.121}$$

The baseline essentially represents the distance between the two measuring telescopes.

Chapter 4

Numerical Methods

This chapter outlines the procedure utilized in the code, along with the numerical methods employed. It also discusses the set of initial and boundary conditions. Establishing the boundary conditions, in particular, presents a delicate challenge that requires cautious exploration because of its impact on the speed of convergence. Finally, a benchmark for a specific set of parameters is provided.

4.1 Time scales

The numerical method relies on the separation of several time scales to differentiate between processes and simplify numerical computations. The shortest time scale corresponds to radiative transfer in the optically thin regime, denoted as $t_{\mathrm{rad}} = R/c$, where light traverses a characteristic distance R at nearly vacuum light speed c. The second shortest time scale is the dynamical time scale required to achieve hydrostatic equilibrium, expressed as $t_{\mathrm{dyn}} = R/v_k = 1/\Omega$, where v_k represents the Keplerian orbital velocity and Ω denotes the angular velocity. After one orbit, each particle experiences equilibrium between the upper and lower hemispheres. Subsequently, the thermal time scale $t_{\mathrm{therm}} = E_t/W_{\mathrm{heat}}$ emerges, representing the time it takes for the temperature to reach equilibrium. This can be estimated by dividing the enthalpy of the disk per volume by the viscous dissipation:

$$\begin{aligned} t_{\text{therm}} &= \frac{\frac{\Gamma}{\Gamma-1}p}{\rho\nu_t[r\partial_r\Omega]^2} && (4.1)\\ &= \frac{\Gamma}{\Gamma-1}\frac{\frac{k_BT}{\mu_g u}\rho}{\frac{9}{4}\Omega^2\nu_t\rho} && (4.2)\\ &= \frac{4\Gamma}{9(\Gamma-1)}\frac{c_s^2}{\alpha\Omega^2\frac{c_s^2}{\Omega}} && (4.3)\\ &\approx \frac{1}{\alpha\Omega}. && (4.4) \end{aligned}$$

The fourth and final time scale to consider is the viscous time scale, denoted as $t_{\text{visc}} = R/(-v_r)$, where v_r represents the radial drift speed. This time scale pertains to the evolution of the surface density profile. To estimate the radial drift velocity, one can utilize equation (3.95) and the accretion flux through a ring:

$$\begin{aligned} \dot{M} &= 3\pi\nu_t\Sigma = -2\pi R\Sigma v_r && (4.5)\\ v_r &= -\frac{3\nu_t}{2R} && (4.6)\\ t_{\text{visc}} &= \frac{2R^2}{3\alpha H c_s} && (4.7)\\ &= \frac{2}{3\alpha\Omega}\left(\frac{R}{H}\right)^2. && (4.8) \end{aligned}$$

This time scale is the longest because $R \gg H$, or equivalently, the radial velocity is very small. This explains why the radial velocity could be neglected in previous calculations.
Given the order of magnitudes as:

$$t_{\text{rad}} \ll t_{\text{dyn}} \ll t_{\text{therm}} \ll t_{\text{visc}} \tag{4.9}$$

one can separately compute the radiation flux from the star and the local volume density through the vertical hydrostatic balance for each temperature profile. These values can then be used to solve the equations for the internal energy and the radiation energy to obtain the next temperature profile. The global surface density profile changes slowly over many iterations of the temperature profile and is the last variable to converge.

4.2 Finite volumes

The system of coupled equations discussed in section 3.3 is numerically solved using the finite volume method. This involves dividing the space into small volumes,

which, in the case of spherical coordinates, are spherical segments. Naturally, these volumes vary in size and must be duly considered. The necessary geometric coefficients are computed in this section.
Given that the focus of the problem lies in energies, namely internal and radiation energy, the two formulae adopt the general form of a conservation law with source and loss or exchange terms. Therefore, to illustrate the principle, it is beneficial to examine a simple conservation law expressed by the following partial differential equation:

$$\partial_t E + \nabla \cdot (\nabla E) = 0. \tag{4.10}$$

The complete expressions for ϵ and E_R will be provided in section 4.3. Initially, the process involves integrating over a specific cell (i, j) with volume $v_{i,j}$.

$$\int\limits_{v_{i,j}} \partial_t E \, dV + \int\limits_{v_{i,j}} \nabla \cdot (\nabla E) \, dV = 0 \tag{4.11}$$

$$v_{i,j} \partial_t E_{i,j} + \oint_{S_{i,j}} \nabla E \cdot \mathbf{n} \, dS = 0. \tag{4.12}$$

In the next step, $E_{i,j}$ denotes the averaged value of E within the cell (i, j), and for the second term, the divergence theorem is employed. Next, the spherical coordinates are introduced:

$$\partial_t E_{i,j} + \frac{1}{v_{i,j}} \oint_{S_{i,j}} \left(\partial_r E \mathbf{r} + \frac{1}{r} \partial_\theta E \boldsymbol{\theta} + \frac{1}{r \sin\theta} \partial_\phi E \boldsymbol{\phi} \right) \cdot \mathbf{n} \, dS = 0, \tag{4.13}$$

the equation was divided by $v_{i,j}$, and the bold symbols represent orthonormal vectors. Due to the system's axisymmetry, $\partial_\phi = 0$, the third term in the brackets is zero. The first two terms in the brackets are evaluated by assuming constant $\partial_r E$ and $\partial_\theta E$ over the small surfaces of one tiny volume:

$$\begin{aligned} \partial_t E_{i,j} + \frac{1}{v_{i,j}} \Bigg[& (A_r \partial_r E)_{r_i + 0.5\Delta r} - (A_r \partial_r E)_{r_i - 0.5\Delta r} + \\ & \left(A_\theta \frac{1}{r} \partial_\theta E \right)_{\theta_j + 0.5\Delta\theta} - \left(A_\theta \frac{1}{r} \partial_\theta E \right)_{\theta_j - 0.5\Delta\theta} \Bigg] = 0. \end{aligned} \tag{4.14}$$

Subsequently, the volume $v_{i,j}$ and the areas A_r and A_θ are computed. To simplify, a new notation is introduced, where $r_i \pm 0.5\Delta r = r_{i\pm0.5}$, $\theta_j \pm 0.5\Delta\theta = \theta_{j\pm0.5}$, and

$\phi_k \pm 0.5\Delta\phi = \phi_{k\pm0.5}$:

$$\begin{aligned}
v_{i,j} &= \int\limits_{\phi_{k-0.5}}^{\phi_{k+0.5}} \int\limits_{\theta_{j-0.5}}^{\theta_{j+0.5}} \int\limits_{r_{i-0.5}}^{r_{i+0.5}} r^2 \sin\theta dr d\theta d\phi && (4.15)\\
&= \frac{1}{3}(r_{i+0.5}^3 - r_{i-0.5}^3)(\cos\theta_{j-0.5} - \cos\theta_{j+0.5})(\phi_{k+0.5} - \phi_{k-0.5}) && (4.16)\\
A_{r_i} &= \int\limits_{\phi_{k-0.5}}^{\phi_{k+0.5}} \int\limits_{\theta_{j-0.5}}^{\theta_{j+0.5}} r_i^2 \sin\theta d\theta d\phi && (4.17)\\
&= r_i^2(\cos\theta_{j-0.5} - \cos\theta_{j+0.5})(\phi_{k+0.5} - \phi_{k-0.5}) && (4.18)\\
A_{\theta_j} &= \int\limits_{\phi_{k-0.5}}^{\phi_{k+0.5}} \int\limits_{r_{i-0.5}}^{r_{i+0.5}} r \sin\theta_j dr d\phi && (4.19)\\
&= \frac{1}{2}(r_{i+0.5}^2 - r_{i-0.5}^2)\sin\theta_j(\phi_{k+0.5} - \phi_{k-0.5}). && (4.20)
\end{aligned}$$

Especially the respective ratios

$$\begin{aligned}
\frac{A_{r_i}}{v_i} &= \frac{r_i^2}{\frac{1}{3}(r_{i+0.5}^3 - r_{i-0.5}^3)} \qquad \text{and} && (4.21)\\
\frac{A_{\theta_j}}{v_i} &= \frac{\sin\theta_j}{\cos\theta_{j-0.5} - \cos\theta_{j+0.5}} \frac{\frac{1}{2}(r_{i+0.5}^2 - r_{i-0.5}^2)}{\frac{1}{3}(r_{i+0.5}^3 - r_{i-0.5}^3)} && (4.22)\\
&\approx \frac{\sin\theta_j}{\cos\theta_{j-0.5} - \cos\theta_{j+0.5}} \frac{1}{r_i} && (4.23)
\end{aligned}$$

are of interest.

In the previous step, the rule of L'Hospital was employed to assess the limit of the second ratio, which is valid for infinitesimal volumes and provides a highly accurate approximation for small ones. With this, it becomes both possible and advantageous to define some of the geometry coefficients as follows:

$$\begin{aligned}
S_i^r &= r_i^2 && (4.24)\\
S_j^\theta &= |\sin\theta_j| && (4.25)\\
V_i^r &= \frac{1}{3}(r_{i+0.5}^3 - r_{i-0.5}^3) && (4.26)\\
V_j^\theta &= |\cos\theta_{j-0.5} - \cos\theta_{j+0.5}|, && (4.27)
\end{aligned}$$

taking the absolute value ensures that both volume and surface are always positive. These values can be substituted into (4.14) to obtain

$$\begin{aligned}\partial_t E_{i,j} + \frac{S^r_{i+0.5}}{V^r_i}(\partial_r E)_{i+0.5,j} - \frac{S^r_{i-0.5}}{V^r_i}(\partial_r E)_{i-0.5,j} \\ + \frac{S^\theta_{j+0.5}}{r_i^2 V^\theta_j}(\partial_\theta E)_{i,j+0.5} - \frac{S^\theta_{j-0.5}}{r_i^2 V^\theta_j}(\partial_\theta E)_{i,j-0.5} = 0.\end{aligned} \tag{4.28}$$

Finally, all partial derivatives can be substituted with centered differences, except for the time step, which utilizes a backward difference:

$$\begin{aligned}\frac{E^{n+1}_{i,j} - E^n_{i,j}}{\Delta t} + \frac{S^r_{i+0.5}}{V^r_i}\frac{E^{n+1}_{i+1,j} - E^{n+1}_{i,j}}{\Delta r} - \frac{S^r_{i-0.5}}{V^r_i}\frac{E^{n+1}_{i,j} - E^{n+1}_{i-1,j}}{\Delta r} \\ + \frac{S^\theta_{j+0.5}}{r_i^2 V^\theta_j}\frac{E^{n+1}_{i,j+1} - E^{n+1}_{i,j}}{\Delta \theta} - \frac{S^\theta_{j-0.5}}{r_i^2 V^\theta_j}\frac{E^{n+1}_{i,j} - E^{n+1}_{i,j-1}}{\Delta \theta} = 0,\end{aligned} \tag{4.29}$$

here, the superscript n denotes the time iteration. This notation is also adopted in section 4.3 to present the equations.

4.3 Iterative procedure

The process for determining the final disk structure involves three main steps.
Firstly, the hydrostatic equilibrium is computed for a given temperature distribution, this will be explained in the following section 4.3.1. Additionally, the optical depth is calculated using equation (3.24), allowing for the determination of the corresponding radiation flux F_* using equation (3.23).
Secondly, the two coupled equations for the temperature and radiation field from section 3.3 are solved implicitly, see section 4.3.2 for more details.
The last step involves computing the dust-to-gas ratio using equation 3.52 or its earlier versions depending on the flags set in the input file. When diffusion is included another matrix inversion is performed on the dust and gas density files, to simulate one diffusion time passing, as described in section 3.4.2.
Following this, the process iterates again, commencing with the determination of hydrostatic equilibrium for the updated temperatures until the simulation converges. To aid numerical stability the dust-to-gas ratio logarithmically increases for the first few steps through a prefactor, so that the calculation begins with no dust present and then the effect is slowly introduced. The specific number of steps over which the dust is introduced can be set in the input file; 30 steps has proven beneficial. The grid spacing is equidistant in both radial and polar direction. Furthermore it is possible to set multiple different time step sizes, e.g. initially smaller ones for a set number of iterations, then bigger ones afterwards and in the end smaller ones again. This way the code converges into a stable configuration faster. The convergence criteria are explained in section 4.4.

4.3.1 Vertical integration

To determine the gas density distribution of the disk, the hydrostatic equations outlined in section 3.2 are integrated outward from the midplane, both upwards and downwards in the polar direction.
For the density at the equatorial plane ρ_0, the surface density Σ and the pressure scale height $H = [k_B T r^3/(GM_* \mu_g u)]^{0.5}$ are employed:

$$\rho_0 = \frac{\Sigma}{\sqrt{2\pi} H}. \tag{4.30}$$

As the density peaks at the centre of the disk, this value gradually decreases further above or below the midplane. However, in the outer regions of the Gaussian-like distribution, this reduction may lead to negative density values if overestimated. To mitigate this issue, the logarithm of the density is utilized, then integrated, and subsequently exponentiated again. Employing a fourth-order Runge-Kutta integration ensures high accuracy in density calculations. Indeed, the sum of all densities at a particular radius is within 0.01% of the postulated $\Sigma(r)$ with which the integration commenced.
Following the calculation of ρ_0, the next step involves determining v_ϕ at the midplane using equation (3.4):

$$\begin{aligned}
\frac{\rho v_\phi^2}{r} &= \partial_r p + \rho \partial_r \Phi & (4.31)\\
v_\phi^2 &= r\left(\frac{1}{\rho}\partial_r p + \partial_r \Phi\right) & (4.32)\\
v_\phi &= \left[r\left(\frac{1}{\rho}\partial_r p + \partial_r \Phi\right)\right]^{0.5} & (4.33)\\
&= \left[r\left(\frac{k_B}{\mu_g u}\partial_r T + \frac{k_B T}{\mu_g u \rho}\partial_r \rho - \frac{GM_*}{r^2}\right)\right]^{0.5}. & (4.34)
\end{aligned}$$

The derivatives are computed using five-point stencils. Since the temperature is known everywhere and the density is known for the midplane, v_ϕ can be computed. Substituting this into (3.5), one has:

$$\begin{aligned}
\partial_\theta p &= \frac{\rho v_\phi^2}{\tan\theta} && (4.35)\\
\frac{k_B}{\mu_g u}\left(\rho\partial_\theta T + T\partial_\theta \rho\right) &= \frac{\rho v_\phi^2}{\tan\theta} && (4.36)\\
\frac{1}{T}\partial_\theta T + \frac{1}{\rho}\partial_\theta \rho &= \frac{\mu_g u}{k_B T}\frac{v_\phi^2}{\tan\theta} && (4.37)\\
\partial_\theta(\log\rho) &= \frac{1}{T}\left(\frac{\mu_g u\, v_\theta^2}{k_B\tan\theta} - \partial_\theta T\right) && (4.38)\\
(\log\rho)_{j+1} &= (\log\rho)_j + \Delta\theta\left[\frac{1}{T}\left(\frac{\mu_g u\, v_\theta^2}{k_B\tan\theta} - \partial_\theta T\right)\right]_{j+0.5} && (4.39)
\end{aligned}$$

This process is employed to compute the next polar row of $\rho(\theta)$. Initially, it is executed for the upper half and then for the lower one, both for the grid points and half grid points simultaneously. The temperature is linearly interpolated to obtain values at the half grid points. Only the initial step from the midplane outwards needs to be predictive, as subsequently the half grid points are integrated using the grid points for the evaluation of the integral and vice versa. The values of ρ and v_ϕ are stored at both half grid points and grid points for later use. The final profile in the θ-direction retains a Gaussian-like shape, as depicted in figure 4.1, while also accounting for the non-uniform temperature distribution.

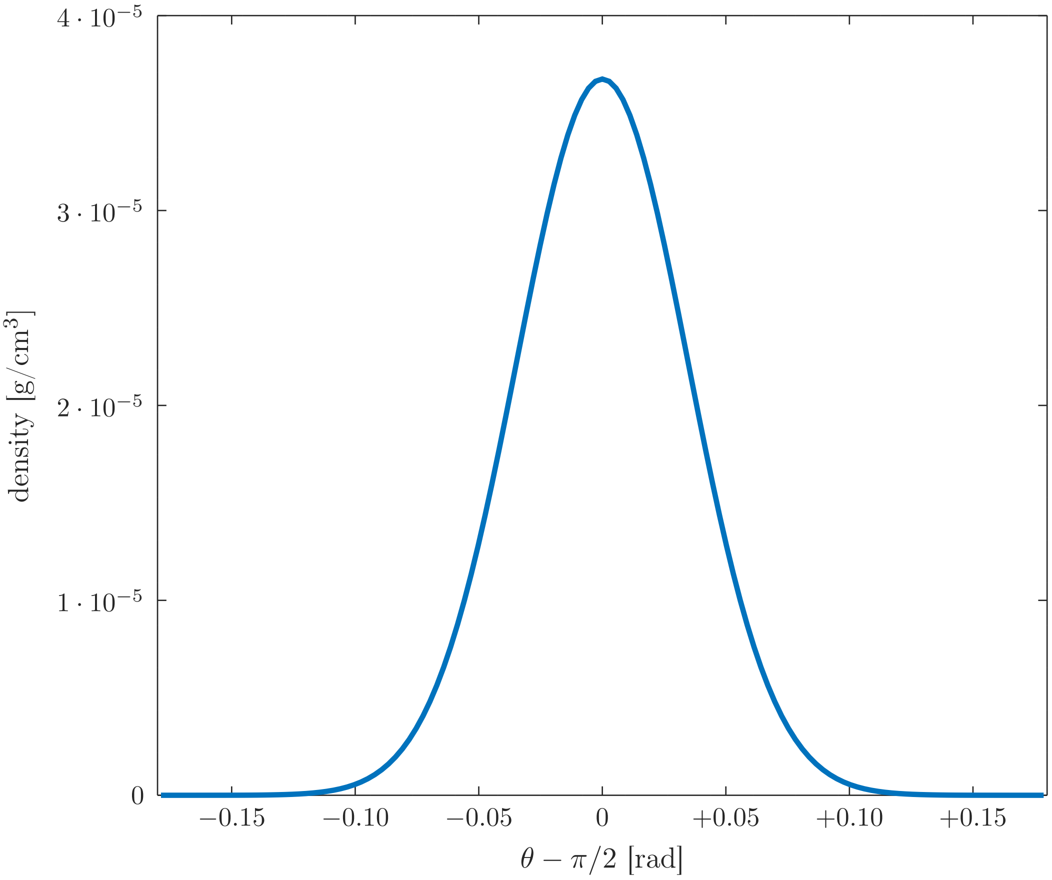

Figure 4.1: The gas density distribution as a function of θ at a constant radius resembles a Gaussian.

4.3.2 Matrix inversion and implicit equations

The second step is to implicitly solve the two coupled equations for the temperature and radiation field from section 3.3. The equations are in the notation from section 4.2:

$$
\begin{aligned}
\frac{E^{n+1}_{R,i,j}-E^{n}_{R,i,j}}{\Delta t} =& \left(\frac{c\lambda}{\sigma}\right)^{n}_{i+0.5,j}\frac{S^{r}_{i+0.5}}{V^{r}_{i}}\frac{E^{n+1}_{R,i+1,j}-E^{n+1}_{R,i,j}}{\Delta r}\\
&-\left(\frac{c\lambda}{\sigma}\right)^{n}_{i-0.5,j}\frac{S^{r}_{i-0.5}}{V^{r}_{i}}\frac{E^{n+1}_{R,i,j}-E^{n+1}_{R,i-1,j}}{\Delta r}\\
&+\left(\frac{c\lambda}{\sigma}\right)^{n}_{i,j+0.5}\frac{S^{\theta}_{j+0.5}}{r_i^2V^{\theta}_{j}}\frac{E^{n+1}_{R,i,j+1}-E^{n+1}_{R,i,j}}{\Delta \theta}\\
&-\left(\frac{c\lambda}{\sigma}\right)^{n}_{i,j-0.5}\frac{S^{\theta}_{j-0.5}}{r_i^2V^{\theta}_{j}}\frac{E^{n+1}_{R,i,j}-E^{n+1}_{R,i,j-1}}{\Delta \theta}\\
&+\sigma^{n}_{i,j}c\left(a_R\left(T^{n+1}_{i,j}\right)^4-E^{n+1}_{R,i,j}\right) \qquad \text{and}
\end{aligned}
\tag{4.40}
$$

$$
\begin{aligned}
\frac{c^n_vT^{n+1}_{i,j}-c^n_vT^{n}_{i,j}}{\Delta t} =& \left(\frac{\Gamma c_v\nu_t}{Pr_t}\right)^{n}_{i+0.5,j}\frac{S^{r}_{i+0.5}}{V^{r}_{i}}\frac{T^{n+1}_{i+1,j}-T^{n+1}_{i,j}}{\Delta r}\\
&-\left(\frac{\Gamma c_v\nu_t}{Pr_t}\right)^{n}_{i-0.5,j}\frac{S^{r}_{i-0.5}}{V^{r}_{i}}\frac{T^{n+1}_{i,j}-T^{n+1}_{i-1,j}}{\Delta r}\\
&+\left(\frac{\Gamma c_v\nu_t}{Pr_t}\right)^{n}_{i,j+0.5}\frac{S^{\theta}_{j+0.5}}{r_i^2V^{\theta}_{j}}\frac{T^{n+1}_{i,j+1}-T^{n+1}_{i,j}}{\Delta \theta}\\
&-\left(\frac{\Gamma c_v\nu_t}{Pr_t}\right)^{n}_{i,j-0.5}\frac{S^{\theta}_{j-0.5}}{r_i^2V^{\theta}_{j}}\frac{T^{n+1}_{i,j}-T^{n+1}_{i,j-1}}{\Delta \theta}\\
&-\left(\kappa_{\mathrm{gas}}+f_{\mathrm{d2g}}\kappa_{\mathrm{dust}}(\nu_{\mathrm{rim}})\right)^{n}_{i,j}c\left(a_R\left(T^{n+1}_{i,j}\right)^4-E^{n+1}_{R,i,j}\right)\\
&+F_{*,i,j}\left(\kappa_{\mathrm{gas}}+f_{\mathrm{d2g}}\kappa_{\mathrm{dust}}(\nu_{*})\right)^{n}_{i,j}.
\end{aligned}
\tag{4.41}
$$

The last term in eq. (4.41) was transformed according to section 2.1 in (SVUFP24). The equations are coupled by linearising the term proportional to T^4, which appears in both of them, as explained in (Commerçon et al. 2011):

$$
\left(T^{n+1}\right)^4 = 4\left(T^n\right)^3T^{n+1}-3\left(T^n\right)^4. \tag{4.42}
$$

This formulation allows the equations to be arranged into a matrix form, $\mathbf{A}\cdot\mathbf{x}=\mathbf{b}$, where $\mathbf{x}$ represents the solution vector of the form $\mathbf{x}=\left(T^{n+1}11, E^{n+1}R, 11, T^{n+1}_{12}, ...\right)^t$, with alternating entries of temperature and radiation energy, and $\mathbf{b}$ contains all terms that are not proportional to E^{n+1}_R or T^{n+1}. As a result, the matrix has non-zero entries on seven diagonals, as illustrated in figure 4.2.

The next step involves inverting the matrix $\mathbf{A}$. In the earlier version of the code,

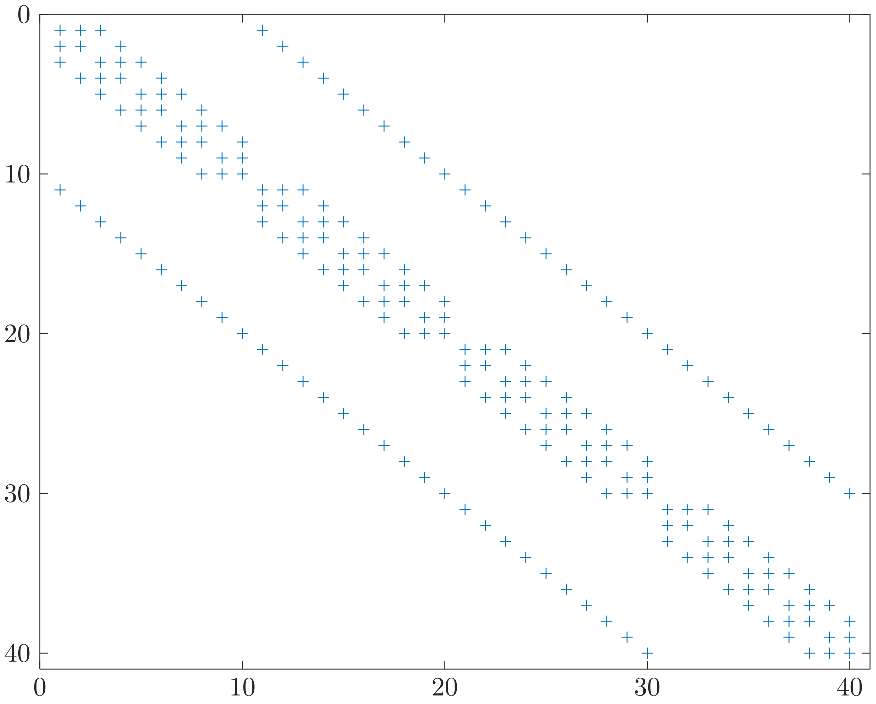

Figure 4.2: The matrix $\mathbf{A}$ with non-zero entries marked with a $+$.

named `radiation_code` and written in octave, this is accomplished using the BiCSTAB solver initially introduced by Van der Vorst (1992), as it is well-suited for sparsely populated, non-symmetric matrices. For preconditioning, incomplete LU-factorization is utilized, and the convergence criteria rely on the reduction of the L_2 norm of the residual, $||\mathbf{r}||_2/||\mathbf{r}_{\text{init}}||_2 < 10^{-5}$. This code is used for the first two publications.

The code was then completely rewritten in C++ and renamed `rmhd_code`. This version uses the LU-factorisation provided by the UMFPACK (Davis 2006) and was used in the third publication. It has a considerably improved runtime, and enables the solution of problems at significantly higher grid resolutions.

The matrix $\mathbf{A}$ is represented in compressed column form, i.e. it consists of three arrays (Ap[n+1], Ai[n_z] and Ax[n_z]). If the matrix is m-by-n with n_z entries and has the following form:

$$\mathbf{A} = \begin{bmatrix} 2.5 & 3 & 0 & 0 & 0 \\ 3 & 0 & 4 & 0 & 6 \\ 0 & 5 & 7 & 2.6 & 0 \\ 0 & 0 & 1 & 0 & 0 \\ 0 & 4 & 2 & 0 & 1 \end{bmatrix} \tag{4.43}$$

Then Ap[j] stores the cumulative number of entries up to and including the j-th column. The first entry Ap[0] is always 0 and the final entry Ap[n+1] is always n$_z$ the total number of entries. The row indices of entries in column j are stored in Ai[ ] (starting to count at 0 for the first row) and the corresponding numerical values are stored in Ax, that means for the matrix **A** as above the three arrays would be:

$$\begin{aligned} \mathrm{Ap}[\,] &= \{0, 2, 5, 9, 10, 12\} \\ \mathrm{Ai}[\,] &= \{0, 1, 0, 2, 4, 1, 2, 3, 4, 2, 1, 4\} \\ \mathrm{Ax}[\,] &= \{2.5, 3, 3, 5, 4, 4, 7, 1, 2, 2.6, 6, 1\} \end{aligned} \tag{4.44}$$

The matrix inversion for the dust diffusion is separate, because it needs to be performed sequentially after the temperature and radiation energy matrix inversion. However, it follows the same numerical process as described above.

4.4 Convergence Criteria

As a convergence criterion the change in the temperature and density fields is examined. Simulations are converged when they fulfil:

$$\max(\max((T^n - T^{n-1})/T^{n-1}), \max((\rho^n - \rho^{n-1})/\rho^{n-1})) < 10^{-4} \tag{4.45}$$

In all cases shown in this work the criterion plateaus afterwards, sometimes at even lower values.
One exception to this rule is the periodic behaviour observed in one case showcased in (Schobert, B. N. & Peeters, A. G. 2021). In that case the disk was considered converged when the outer region fulfils the convergence criterion and the inner periodic region has completed more than 100 cycles.

4.5 Initial and boundary conditions

As stated in the previous section, initially, no dust is present, resulting in a dust-to-gas ratio of zero throughout. Consequently, the initial temperature distribution mirrors that of an optically thin gas. Assuming the existence of a single spherical dust grain with radius a at a distance r from the star, it presents a geometric cross-section of πa^2 and radiates its energy across its entire surface area $4\pi a^2$. Equating the cooling and heating rates of the dust grain yields:

$$F_{\mathrm{cool}} = F_{\mathrm{heat}} \tag{4.46}$$

$$4\pi a^2 \beta \sigma_B T_{\mathrm{thin}}^4 = \pi a^2 \alpha \sigma_B \left(\frac{R_*}{r}\right)^2 T_*^4 \tag{4.47}$$

$$T_{\mathrm{thin}}(r) = \left(\frac{1}{\epsilon}\right)^{0.25} \left(\frac{R_*}{2r}\right)^{0.5} T_* \tag{4.48}$$

where ϵ represents the ratio between emission and absorption efficiency (Dullemond & Monnier 2010). The initial temperature distribution is computed with $\epsilon_{\text{gas}} = 1$. Subsequently, the initial surface density can be calculated using eq. (3.95), or set as constant, as in the benchmark case, with density integration performed accordingly. The initial condition for the radiation energy density is: $E_R = a_R T^4$ with the radiation constant a_R.
Next the boundary conditions must be considered. The temperature field is subject to a zero gradient on all four edges, while the boundaries for the energy density remain fixed.
Determining boundary conditions for the outer regions poses a challenge, particularly due to their higher dust content, making it difficult to obtain analytic solutions. Therefore, at the outer edge ($r = r_{\text{max}}$), the radiation energy is fixed. In the first two publications the outer point was at 4 AU and the boundary condition was set at $E_R = 3.4255 \cdot 10^{-6}\,\text{J/m}^3$, approximately equivalent to 260 K. This temperature matches the outer edge temperature reported in Flock et al. (2016) and is also close to the analytical expression in Ueda et al. (2017). In the third publication it was necessary to consider the stellar environment to find a realistic value, additionally the computational domain was chosen larger, for more detailed information see (SVUFP24).
To establish boundary conditions for the remaining three edges, one must analytically solve (3.17). Assuming convergence of the final solution, $\partial_t = 0$ is set to obtain:

$$0 = -\sigma c (a_R T^4 - E_R) - \nabla \cdot \mathbf{F}_* \tag{4.49}$$

and with the expression for the stellar flux (3.23) and the divergence in spherical coordinates this is

$$0 = -\sigma c (a_R T^4 - E_R) + F_* \partial_r \tau. \tag{4.50}$$

With (3.24), one can derive the optical depth τ towards the radius, expanding the mean opacities σ and σ_* using (3.25) - (3.27) to obtain:

$$c\rho_{\text{gas}}[\kappa_{\text{gas}} + f_{\text{d2g}}\kappa_{\text{dust}}(\nu_{\text{rim}})](a_R T^4 - E_R) = F_* \rho_{\text{gas}}[\kappa_{\text{gas}} + f_{\text{d2g}}\kappa_{\text{dust}}(\nu_*)] \tag{4.51}$$

$$(a_R T^4 - E_R) = \frac{F_*}{c} \frac{\kappa_{\text{gas}} + f_{\text{d2g}}\kappa_{\text{dust}}(\nu_*)}{\kappa_{\text{gas}} + f_{\text{d2g}}\kappa_{\text{dust}}(\nu_{\text{rim}})}. \tag{4.52}$$

On the right hand side one finds the ratio between the mean opacities, which can be identified with the previous ϵ like this:

$$\epsilon = \frac{\kappa_{\text{gas}} + f_{\text{d2g}}\kappa_{\text{dust}}(\nu_{\text{rim}})}{\kappa_{\text{gas}} + f_{\text{d2g}}\kappa_{\text{dust}}(\nu_*)}, \tag{4.53}$$

that simplifies the equation to

$$(a_R T^4 - E_R) = \frac{F_*}{c}\frac{1}{\epsilon} \tag{4.54}$$

$$E_R = a_R T^4 - \frac{1}{\epsilon}\frac{F_*}{c}. \tag{4.55}$$

Now, an assumption for the temperature is required, which can be obtained in the optically thin regime using (4.48). Additionally, the stellar flux is expanded to find:

$$E_R = a_R T_{\text{thin}}^4 - \frac{1}{\epsilon}\frac{\sigma_B}{c}\left(\frac{R_*}{r}\right)^2 \mathrm{e}^{-\tau_*} T_*^4 \tag{4.56}$$

$$= a_R T_{\text{thin}}^4 - \frac{1}{\epsilon}\frac{4\sigma_B}{c}\left(\frac{R_*}{2r}\right)^2 \mathrm{e}^{-\tau_*} T_*^4 \tag{4.57}$$

$$= (1 - \mathrm{e}^{-\tau_*}) a_R \frac{1}{\epsilon}\left(\frac{R_*}{2r}\right)^2 T_*^4 \tag{4.58}$$

$$= (1 - \mathrm{e}^{-\tau_*}) a_R T_{\text{thin}}^4. \tag{4.59}$$

And this serves as the boundary condition for the radiation energy density in the optically thin regime.

At the inner edge ($r = r_{\text{min}}$), this condition simplifies to:

$$E_R = (1 - \mathrm{e}^{-\tau_0}) a_R T_{\text{thin}}^4(r_{\text{min}}), \tag{4.60}$$

which accounts for the optical depth up to the inner boundary, while still assuming $\epsilon_{\text{gas}} = 1$ since no dust is present near the star.

On the upper and lower radial boundaries ($\theta = \theta_{\text{min}}, \theta_{\text{max}}$), the situation is more intricate. While the gas remains optically thin, the condition is given in eq. (4.59) but with the modified ϵ incorporating the dust-to-gas ratio from eq. (4.53). This means the ratio between emission and absorption efficiencies ϵ continuously transitions from the gas value $\epsilon_{\text{gas}} = 1$ to the dust value $\epsilon_{\text{dust}} = \frac{1}{3}$. This approach continues until the dust-to-gas ratio on the rim reaches its maximum value f_0.

At this juncture, the assumption of an optically thin gas temperature breaks down. Therefore, once the dust is fully present ($f_{d2g} = f_0$), the flaring disk approximation for the radiation energy, derived for the temperature in section 3.5.1, is employed:

$$E_R = a_R T_{\text{flaring}}^4 \tag{4.61}$$

$$= a_R \left(\frac{550\,\mathrm{K}}{r_{\text{AU}}^{3/7}}\right)^4, \tag{4.62}$$

In the first two publications, the value of 550 K is also adopted from Flock et al. (2016), and r_{AU} denotes the radius in astronomical units. These analytic expressions partially align with those presented by (Ueda et al. 2017).

Table 4.1: Model `S100` setup parameters.

Parameter	Value
Surface density	100 g cm^{-2}, uniform
$N_r \times N_\theta$	1280×129
$[r_{\mathrm{min}}, r_{\mathrm{max}}]$	[0.2 AU, 4 AU]
$[\theta_{\mathrm{min}}, \theta_{\mathrm{max}}]$	$[\pi/2 - 0.18, \pi/2 + 0.18]$
Stellar parameter	$T_* = 10000$ K, $R_* = 2.5 R_\odot$, $M_* = 2.5 M_\odot$
Gas parameter	$\mu_g = 2.353$, $\Gamma = 1.42$
Dust-to-gas ratio	$f_0 = 0.01$
Time steps	$dt_1 = 10^4\,\mathrm{s}$, $dt_2 = 10^{12}\,\mathrm{s}$
Iterations	$N_1 = 40$, $N_2 = 20$

4.6 Benchmark

To verify the consistency of the code with previous findings, this section presents a benchmark against the `S100` run from Flock et al. (2016). Therefore, both viscous heating and thermal conduction are disabled, and the run utilizes a constant surface density in every iteration for comparability, following the same setup as the comparison run. The parameters employed are listed in table 4.1, typical for a Herbig Ae class star (van den Ancker et al. 1998).

The resulting radial temperature is depicted in figure 4.3, while the dust-to-gas ratio is shown in figure 4.4. The temperatures exhibit good agreement, with slight deviations likely arising from differences in grid spacing or boundary conditions. Similarly, the dust-to-gas ratios demonstrate congruence, albeit a minor discrepancy appears at 0.5,AU due to variations in radial cell sizes. In (Flock et al. 2016), a logarithmically spaced grid was employed, whereas this version adopts equidistant spacing, impacting $f_{\Delta\tau}$ in (3.30). Consequently, the runs are not numerically identical due to differences in code implementation.

Figure 3.2 illustrates a vertical 2D cross-section through the protoplanetary disk. The star is located further to the left, while the disk extends into space on the right. Notably, the y-axis represents the polar angle rather than height, hence a conical disk appears flat in this representation, whereas a flaring disk exhibits expansion to greater angles with larger radii. The x-axis, logarithmic to better display the inner region of interest, indicates radial distance from the star. Since the disk is symmetric in the ϕ-direction, a 2D cut effectively captures all significant features.

The lower depiction showcases a profile of the dust density, revealing familiar characteristics such as the dust halo from 0.3 AU to 0.5 AU, a rounded-off rim from 0.5 AU to 1.0 AU, and a shadowed region beyond 1.0 AU, consistent with findings from the `S100` run. The upper image displays the temperature profile,

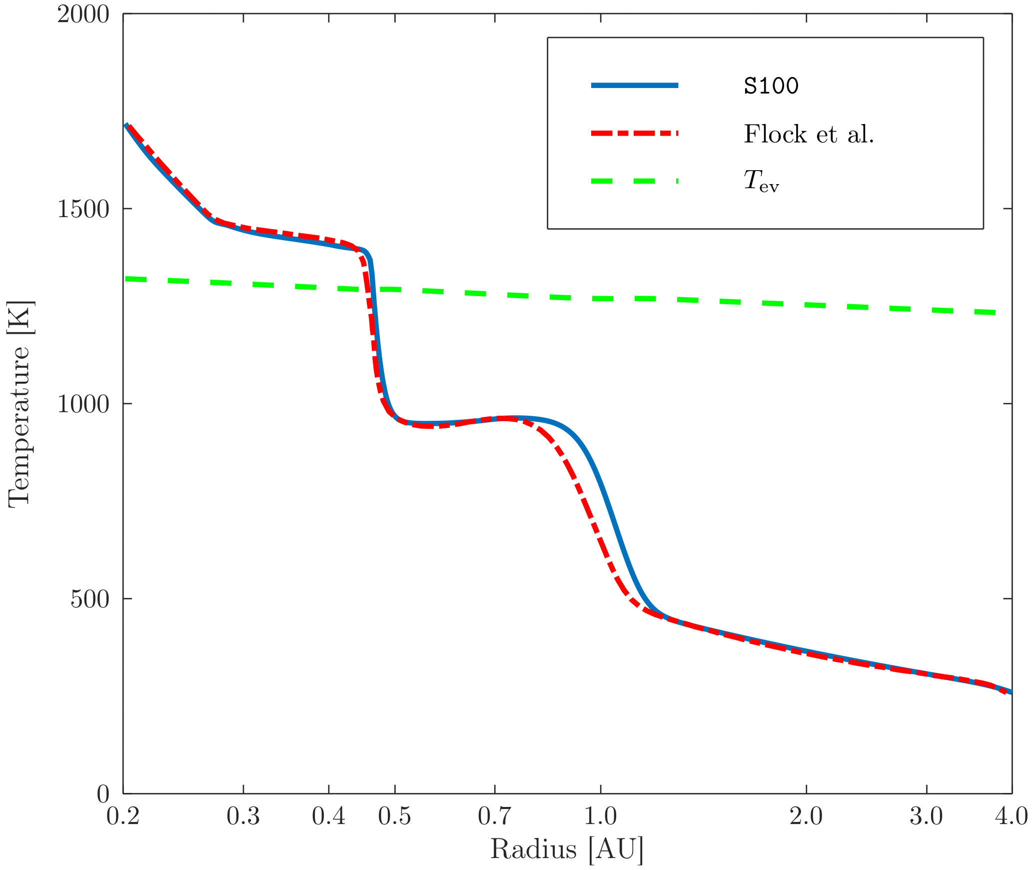

Figure 4.3: The midplane radial temperature profile (blue solid line) for model `S100` compared to the temperature profile of (Flock et al. 2016) (red dashed and dotted line). The evaporation temperature (green dashed line) is shown for reference.

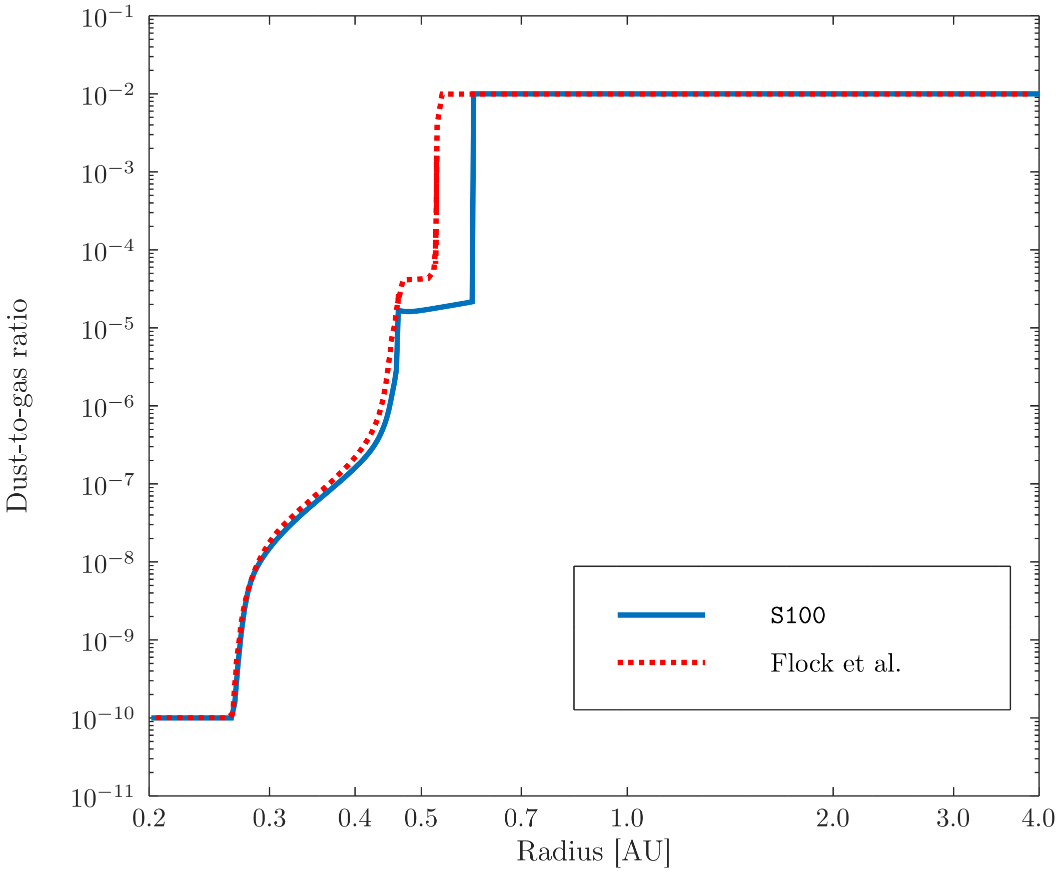

Figure 4.4: The midplane radial profile of the dust-to-gas ratio (blue solid line) for model `S100` compared to the dust-to-gas ratio of (Flock et al. 2016) (red dotted line).

with temperatures following the analytic prediction for an optically thin gas from 0.2 AU to 0.3 AU. Subsequently, as the dust halo forms, the midplane temperature plateaus at approximately 1400 K before dropping abruptly at the evaporation front at 0.5 AU. The temperature within the rounded-off rim remains relatively constant at 1000 K. Transitioning to the shadowed region at 1.0 AU, temperatures gradually decrease to 500 K before aligning with the analytic prediction for a flaring disk. In the outer disk region, temperatures remain vertically constant at each radius.

These findings align entirely with those of Flock et al. (2016), indicating that the simulation faithfully reproduces qualitative and quantitative results for identical parameters. Thus, the benchmark is deemed complete and successful.

Chapter 5

List of Publications with Author Contributions

This chapter lists all the publications that are included in the cumulative thesis, and states where they where published.
The included works are:

- Schobert, B. N., Peeters, A. G. & Rath, F., 2019, The Astrophysical Journal, 881:56
  Title: "THE IMPACT OF ACCRETION HEATING AND THERMAL CONDUCTION ON THE DEAD ZONE OF PROTOPLANETARY DISKS"
  URL: `https://doi.org/10.3847/1538-4357/ab2df6`
  Short: **SPR19**, see Chapter 6
- Schobert, B. N. & Peeters, A. G., 2021, Astronomy & Astrophysics, 651, A27
  Title: "IMPACT OF DUST DIFFUSION ON THE RIM SHAPE OF PROTOPLANETARY DISKS"
  URL: `https://doi.org/10.1051/0004-6361/202039398`
  Short: **SP21**, see Chapter 7
- Schobert, B. N., Varga, J., Ueda, T., Flock, M. & Peeters, A. G., 2024, submitted to Astronomy & Astrophysics, in review
  Title: "NUMERICAL MODELLING OF THE INNER DISK STRUCTURE OF A YOUNG STELLAR OBJECT: HD 144432 BASED ON NEAR- AND MID-INFRARED INTERFEROMETRY AND SPECTROSCOPY "
  Short: **SVUFP24**, see Chapter 8

The first two works have been published in "The Astrophysical Journal" Schobert et al. (2019) and "Astronomy & Astrophysics" Schobert, B. N. & Peeters, A. G. (2021) respectively. The third paper has been submitted to "Astronomy & Astrophysics" and is currently in review.

5.1 SPR19

As mentioned in the initial summary the aim of this project was to understand the inner physical processes of a protoplanetary disk. Specifically to investigate passive versus active disks, where accretion heating plays only a minor role in the first category, whereas it is significant in the second one.

For this publication I (Benjamin N. Schobert, first author) developed a physical model based on a previous work Flock et al. (2016). I included accretion heating in the energy conservation, which is a equilibrium between internal heat and radiative energy. I wrote the code in octave (see: `https://bitbucket.org/astro_bayreuth/radiation_code`), made all the simulations, interpreted the results and made analytical calculations. The paper contents, i.e. the text as well as all plots, were created by me.

The second author, Prof. A. G. Peeters, has contributed in his role as my supervisor, by providing helpful hints and guidance. He has also proofread the final manuscript before and during the submission process.

The third author, Dr. F. Rath, has contributed during the initial model building phase through invaluable discussions about the literature and protoplanetary disk models and has proofread the final manuscript before submission.

5.2 SP21

The second work makes an important step by not only proofing that dust diffusion necessarily occurs in protoplanetary disks, but also by its incorporation in the code, the dust dependence on the temperature can be simplified and is made more physically realistic.

For this work I completely rewrote the code from octave to C++ (see: `https://bitbucket.org/astro_bayreuth/rmhdcode`), making it more capable to handle bigger problems, which were previously unfeasible. This facilitated the inclusion of dust diffusion through an additional implicit system of equations, changes to the dust temperature dependence and better handling of boundary conditions. I made analytical calculations about the lifetime of a typical dust grain, about its Stokes number, measuring how well it is bound to the gas, I ran the simulations and interpreted the results. The paper contents, i.e. the text as well as all plots, were created by me.

The second author, Prof. A. G. Peeters, has contributed in his role as my supervisor, by providing helpful hints and guidance. He has also proofread the final manuscript before and during the submission process.

5.3 SVUFP24

This paper uses the physical model presented in the previous two papers to explain the experimental observations of the YSO HD 144432, especially the deviation of its mid-infrared visibility curve from an a priori expectation.
For this work I specifically modified my code to enable simulations encompassing the complete disk, whereas I only simulated the inner rim region before. I made analytical calculations pertaining to the outer boundary condition as it is set by the companion stars of HD144432A. I programmed a tool to simulate the visibility curve as it would be measured by an interferometric telescope array and performed ray-tracing simulations for the SED. I interpreted the results and formulated conclusions. The paper contents, i.e. the text as well as all the plots, but not the observational data measured by telescopes, were created by me.
The second author, Dr. J. Varga, has provided the observational data, i.e. the SED, as well as the near- and mid-infrared visibility curves Varga, J. et al. (2024) measured by VLTI/MATISSE. He has provided me with the source code of his diagnostic to calculate visibility curves from synthetic images, from which my tool is based off and benchmarked against. We had multiple meetings, where he provided helpful hints and guidance towards the project and explained how the data was measured. He has also proofread the final manuscript before and during the submission process.
The third author, Dr. T. Ueda, provided helpful hints and guidance towards the project through his extensive experience during multiple meetings. He has also proofread the final manuscript before and during the submission process.
The fourth author, Dr. M. Flock, suggested the initial idea for the project and has made the connection between Dr. Varga and me possible, by facilitating a meeting and encouraging a potential cooperation. We had multiple meetings, where he provided helpful hints and guidance towards the project through his extensive experience. He has also proofread the final manuscript before and during the submission process.
The fifth author, Prof. A. G. Peeters, has contributed in his role as my supervisor, by providing helpful hints and guidance. He has also proofread the final manuscript before and during the submission process.

Chapter 6

The Impact of Accretion Heating and Thermal Conduction on the Dead Zone of Protoplanetary Disks

B. N. Schobert, A. G. Peeters, and F. Rath

This chapter has been published in the Astrophysical Journal:

- Schobert, B. N., Peeters, A. G. & Rath, F., 2019, The Astrophysical Journal, 881:56
  URL: `https://doi.org/10.3847/1538-4357/ab2df6`

The Astrophysical Journal, 881:56 (10pp), 2019 August 10 https://doi.org/10.3847/1538-4357/ab2df6

The Impact of Accretion Heating and Thermal Conduction on the Dead Zone of Protoplanetary Disks

B. N. Schobert, A. G. Peeters, and F. Rath
Physics Department, University of Bayreuth, Universitätsstraße 30, Bayreuth, Germany; benjamin.schobert@uni-bayreuth.de

Received 2019 May 2; revised 2019 June 27; accepted 2019 June 28; published 2019 August 13

Abstract

The paper investigates the influence of accretion heating and turbulent heat conduction on the equilibrium of protoplanetary disks, extending the 2D axisymmetric passive disk model of Flock. The model includes dust sublimation and radiative transfer with the flux-limited diffusion approximation, and predicts the density and temperature profiles as well as the dust-to-gas ratio of the disk. It is shown that the accretion heating can have a large impact: for accretion rates above $5 \cdot 10^{-8}\,M_\odot\,\mathrm{yr}^{-1}$ a zone forms behind the silicate condensation front with sufficiently high temperature to sublimate the dust and form a gaseous cavity. Assuming a Prandtl number $\sim$0.7, it is furthermore shown that the turbulent heat conduction cannot be neglected in the evaluation of the temperature profile. While the inner rim position is not affected by viscous heating, the dead zone edge shifts radially outward for higher accretion rates.

Key words: accretion, accretion disks – conduction – hydrodynamics – methods: numerical – protoplanetary disks – radiative transfer

1. Introduction

The observational techniques used to picture exoplanets have constantly been enhanced culminating in the recent observation of a nascent exoplanet, PDS 70b (Keppler et al. 2018; Müller et al. 2018). In order to explain the formation of planets it is paramount to understand the physics of the protoplanetary disks where they originate. Modern terrestrial and satellite telescopes use large parts of the electromagnetic spectrum, especially near-infrared (NIR), to resolve young stellar objects and their disks. Thus, they deliver valuable data for the models to be tested against or built upon. Of special interest are Herbig Ae/Be stars, since they are slightly more massive (2–5 $M_\odot$) but also younger than the Sun (Herbig 1960). Interferometric examinations of such stars allow for conclusions about their disks; however, the interpretation has proven difficult.

Therefore, the theoretical model of such disks has been continually augmented. Early contributions are the α-prescription to estimate the turbulent viscosity (Shakura & Sunyaev 1973) and the flaring disk model (Chiang & Goldreich 1997) for passive disks. In passive disks the effects of viscous dissipation are neglected, which is assumed to be a good approximation for accretion rates below $2 \cdot 10^{-7}\,M_\odot\,\mathrm{yr}^{-1}$ (van den Ancker 2005). The effect of viscous dissipation on the vertical structure of passive disks has been treated in 1D for T Tauri stars by D'Alessio et al. (1998).

Because rocky planets originate in the inner regions of the disk, this is a focus of research (Kretke et al. 2009). The temperatures close to the star are sufficient to sublimate the dust and an inner gaseous zone forms. In Dullemond et al. (2001) this area was modeled to be limited by a cylindrical sublimation front. The stellar radiation is strongly absorbed at this front, leading to a region of lower temperature behind the front known as the dead zone. In this zone the ionization is expected to be insufficient for magnetorotational instability (MRI; Balbus & Hawley 1998) and, consequently, the turbulent viscosity is also possibly small (Turner et al. 2014).

The geometry of the inner rim was further explored by Flock et al. (2016) for Herbig Ae/Be stars. Using a 2D radiative transfer model based on the flux-limited diffusion approximation a rounded-off rim was obtained with four distinct regions: an inner gaseous hole, an optically thin dust halo, the round irradiated rim, and a shadowed region behind it. That work also included accretion heating through viscous dissipation in some models with rates up to $\dot{M} = 10^{-8}\,M_\odot\,\mathrm{yr}^{-1}$. To achieve this a hydrostatic simulation was run first and then the results were used as initial conditions for a second hydrodynamic simulation based on previous work (Flock et al. 2013). At this accretion rate a small increase in temperature of only 10% in the shadowed region was found. The density and temperature structure remained similar to that of a hydrostatic model without accretion heating.

In this paper the abovementioned model is extended to include accretion heating through viscous dissipation at rates beyond $10^{-8}\,M_\odot\,\mathrm{yr}^{-1}$. Indeed, experimental data suggest that accretion rates up to $10^{-6}\,M_\odot\,\mathrm{yr}^{-1}$ are common (van den Ancker 2005) and that 25% of HAe stars have $\dot{M} > 10^{-7}\,M_\odot\,\mathrm{yr}^{-1}$ (Garcia Lopez et al. 2006). Furthermore, the accretion rate of a star decreases with time and is therefore likely to be high in the early stages of development that are relevant for the planet formation. The accretion heating is modeled within a single hydrostatic simulation by modifying the energy balance to include viscous heating. The model is also expanded by adding thermal conduction, so that turbulent heat transport is no longer neglected. This is a reasonable addition considering that turbulence plays a vital role in momentum transfer; it might impact heat transfer as well. The term is estimated by assuming a Prandtl number of order unity and turns out to be relevant as well, especially for cases of high viscous heating. Therefore, it needs to be treated simultaneously, as will be discussed later in Section 2.6.

This paper is structured as follows: Section 2 explains the model equations needed to describe the disk. In Section 3 the numerical model used to solve the equations is presented. Additionally, the boundary conditions are motivated and a benchmark to validate the implementation is performed. Section 4 outlines the results and the qualitative changes compared to a model without accretion heating and thermal conduction. Section 5 discusses the results and possible limitations of the work. The paper concludes in Section 6 with a summary of the results and a short outlook.

2. Model Equations

The model used in this paper closely follows the model of Flock et al. (2016), extending the latter to include viscous heating and turbulent heat conduction. In this section the model equations are presented. Since there is a considerable overlap with Flock et al. (2016) at some points the discussion is brief and the reader is referred to the latter reference. The model describes the density and temperature distributions of the disk for a star with known parameters, specifically mass M_*, radius R_*, and luminosity L_* or, equivalently, surface temperature T_*.

The model relies on the large difference in relevant timescales. These are the dynamical timescale in which hydrostatic equilibrium is achieved t_{dyn}, typically the duration of one orbit; the timescale of radiative transfer in the optically thick regime $t_{\mathrm{rad}}^{\tau\gg 1}$, typically 50 orbits; and the viscous timescale t_{visc} over which the surface density changes, typically 10^4 orbits. For typical disk parameters the ordering is

$$t_{\mathrm{dyn}} \ll t_{\mathrm{rad}}^{\tau\gg 1} \ll t_{\mathrm{visc}}. \tag{1}$$

The timescale followed in the solution is that of the surface density; it changes slowly over many iterations of the temperature profile and is the last variable to converge. The temperature profile for each step is obtained by solving the equations for the internal and radiation energy, which operate on the intermediary timescale. For the density one can assume vertical hydrostatic balance for each step because that forms on an even shorter timescale (Flock et al. 2016).

2.1. Hydrostatic Equilibrium

The density structure is calculated assuming a hydrostatic equilibrium between ideal gas pressure, the centrifugal force, and gravity. It is convenient to use spherical coordinates (r, θ, ϕ) for the model problem, since they facilitate a straightforward integration of the radiation from the star along its optical path. The polar axis of the coordinate system is oriented along the rotational axis of the star, so that the protoplanetary disk lies in the equatorial plane. This means the azimuthal velocity of the gas will be significantly greater than radial or polar velocities $v_\phi \gg v_r, v_\theta$. Neglecting the latter the hydrostatic equations are

$$\frac{\partial p}{\partial r} = -\rho \frac{\partial \Phi}{\partial r} + \frac{\rho\, v_\phi^2}{r}, \tag{2}$$

$$\frac{1}{r}\frac{\partial p}{\partial \theta} = \frac{\rho\, v_\phi^2}{r \tan\theta}, \tag{3}$$

where ρ is the gas density, v_ϕ is the velocity in azimuthal direction, $\Phi = G\, M_*/r$ is the gravitational potential, and p is the pressure. For closure with the thermodynamic equations an ideal gas is assumed:

$$p = \frac{\rho k_{\mathrm{B}} T}{\mu_g u}, \tag{4}$$

with temperature T, Boltzmann constant k_{B}, mean molecular weight μ_g, and atomic mass unit u.

2.2. Radiative Hydrodynamics

The temperature distribution is the solution of a coupled system of equations for the radiation energy density E_R and the internal energy density of the gas ϵ. These equations represent a subset of ideal radiative magnetohydrodynamics with magnetic and electric field neglected. The two coupled equations for the radiation and internal energy are

$$\partial_t \rho\epsilon = -\sigma c (a_R T^4 - E_R) - \nabla \cdot \boldsymbol{F}_*, \tag{5}$$

$$\partial_t E_R - \nabla \frac{c\lambda}{\sigma} \nabla E_R = +\sigma c (a_R T^4 - E_R), \tag{6}$$

where σ is the mean opacity, $a_R = 4\sigma_{\mathrm{B}}/c$ is the radiation constant with σ_{B} being the Stefan–Boltzmann constant, $\boldsymbol{F}_*$ is the irradiation flux from the star, c is the vacuum speed of light, and λ is the flux limiter. The flux limiter acts as a diffusion constant for the radiation energy density; it is taken from Levermore & Pomraning (1981) and has the following form:

$$\lambda = \frac{2 + R}{6 + 3R + R^2} \qquad \text{with} \tag{7}$$

$$R = \frac{|\nabla E_R|}{\sigma E_R}, \tag{8}$$

which fulfills $\lim_{R\to 0} \lambda(R) = 1/3$ in the optically thick limit and $\lim_{R\to\infty} \lambda(R) = 0$ in the optically thin limit. Since the product $R\, \lambda(R)$ can never exceed unity, this flux-limited diffusion theory (FDT) preserves causality by never allowing the radiative flux to exceed the radiation energy density times the speed of light in vacuum.

For closure between internal energy and temperature again the ideal gas approximation

$$\rho\epsilon = c_V \rho T \tag{9}$$

is used. Here c_V is the specific heat capacity. This yields for (5)

$$c_V\, \partial_t \rho T = -\sigma c (a_R T^4 - E_R) - \nabla \cdot \boldsymbol{F}_*. \tag{10}$$

For the irradiation flux blackbody radiation times an attenuation factor is assumed:

$$\boldsymbol{F}_*(r) = \left(\frac{R_*}{r}\right)^2 \sigma_{\mathrm{B}} T_*^4 e^{-\tau_*}, \tag{11}$$

where τ is the optical depth

$$\tau_* = \int_{R_*}^{r} \sigma_* dr = \tau_0 + \int_{r_{\mathrm{min}}}^{r} \sigma_* dr \tag{12}$$

and $\tau_0 = \kappa_{\mathrm{gas}} \rho(r_{\mathrm{min}})(r_{\mathrm{min}} - 3R_*)$.

Furthermore, the mean opacities at the typical wavelengths of the stellar light and the rim's thermal emission are defined as

$$\sigma_* = \rho_{\mathrm{dust}} \kappa_{\mathrm{dust}}(\nu_*) + \rho_{\mathrm{gas}} \kappa_{\mathrm{gas}}, \tag{13}$$

$$\sigma = \rho_{\mathrm{dust}} \kappa_{\mathrm{dust}}(\nu_{\mathrm{rim}}) + \rho_{\mathrm{gas}} \kappa_{\mathrm{gas}}, \tag{14}$$

$$\rho_{\mathrm{dust}} = f_{\mathrm{d2g}}\, \rho_{\mathrm{gas}}. \tag{15}$$

Here κ_{gas} is the frequency-averaged opacity of the gas. Finally, f_{d2g} is the dust-to-gas ratio of the respective densities, and its calculation is explained in the following section.

2.3. Dust Sublimation and Opacities

The most crucial effect for the evolution of the disk is arguably the dust sublimation. Because the dust absorbs more radiation than the gas, it is strongly heated by the star and through its own so-called back-warming, i.e., the infrared radiation emitted by the dust. A small amount of dust can substantially decrease the radiation that reaches the area behind it, making the transition between vapor and condensed dust very thin.

In order to resolve this thin layer the dust sublimation formula from Flock et al. (2016) smooths the transition over a temperature range of 100 K and uses the tangens hyperbolicus as a model function. The formula is

$$\begin{aligned} f_{\mathrm{d2g}} &= \frac{f_{\Delta\tau}}{2}\left\{1 - \tanh\left[\left(\frac{T - T_{\mathrm{ev}}}{100\ \mathrm{K}}\right)^{3}\right]\right\} \\ &\quad \cdot \left\{\frac{1 - \tanh(1 - \tau_*)}{2}\right\} \qquad \text{if } T > T_{\mathrm{ev}} \\ &= \frac{f_0}{2}\{1 - \tanh(20 - \tau_*)\} + f_{\Delta\tau} \quad \text{if } T < T_{\mathrm{ev}}, \end{aligned} \tag{16}$$

with the dust evaporation temperature T_{ev}, the reference dust-to-gas ratio f_0, and the transition dust-to-gas ratio $f_{\Delta}\tau$. For the dust evaporation temperature the fitting model proposed by Isella & Natta (2005)

$$T_{\mathrm{ev}} = 2000\ \mathrm{K}\left(\frac{\rho}{1\ \mathrm{g\ cm^{-3}}}\right)^{0.0195} \tag{17}$$

is used. It describes the dependence of the evaporation temperature on the gas density for silicate grains. The transition dust-to-gas ratio $f_{\Delta\tau}$ is defined as

$$f_{\Delta\tau} = \frac{\Delta\tau_*}{\rho_{\mathrm{gas}}\kappa_{\mathrm{dust}}(\nu_*)\Delta r} = \frac{0.3}{\rho_{\mathrm{gas}}\kappa_{\mathrm{dust}}(\nu_*)\Delta r}, \tag{18}$$

with Δr being the radial size of one grid cell. The transition optical depth of $\Delta\tau_* = 0.3$ is chosen so that the absorption of the radiation at the rim can be resolved (Flock et al. 2016). Furthermore, it is useful for numeric stability to impose a minimum value of $f_{\mathrm{d2g}}^{\mathrm{min}} = 10^{-10}$. The maximum value of $f_0 = 10^{-2}$ is chosen because it reflects the amount of dust present in the interstellar medium (Li & Draine 2001) and therefore represents the maximum ratio in the protoplanetary disk.

The dust sublimation formula describes gradual building up of the dust halo for temperatures lower than T_{ev} and the actual sublimation front for temperatures above. By design, the formula for the dust halo has an upper limit $f_{\Delta}\tau$, which is reached for optical depths larger than one, close to the evaporation temperature. Beyond the condensation front the dust-to-gas ratio grows with the optical depth and reaches its maximum for $\tau_* \geqslant 20$.

Similar to Flock et al. (2016) an average value of $\kappa_{\mathrm{gas}} = 10^{-4}\ \mathrm{cm^2\ g^{-1}}$ is used in the computations of this paper. This value ensures that the optical depth τ_* remains small enough inside the gaseous inner disk, preventing the absorption of too much stellar radiation in this region, which would result in the inner rim moving too close to the star.

For the opacity of the dust two wavelengths are important, the stellar light's and the thermal radiation of the rim at the condensation temperature. In the specific case of a star with a surface temperature $T_* = 10{,}000$ K a dust opacity of $\kappa_{\mathrm{dust}}(\nu_*) = 2100\ \mathrm{cm^2\ g^{-1}}$ is calculated in Flock et al. (2016) using the MieX code by Wolf & Voshchinnikov (2004). Using the same method an opacity of $\kappa_{\mathrm{dust}}(\nu_{\mathrm{rim}}) = 700\ \mathrm{cm^2\ g^{-1}}$ is obtained for thermal radiation of approximately 1300 K, which represents a typical dust sublimation temperature.

2.4. Surface Density

The surface density Σ is modeled using the steady thin disk approximation (Clarke & Carswell 2009)

$$\Sigma = \frac{\dot{M}}{3\pi\nu_t}\left[1 - \left(\frac{R_*}{r}\right)^{0.5}\right] \approx \frac{\dot{M}}{3\pi\nu_t}, \tag{19}$$

where the latter approximation applies at distances much larger than the radius of the star. Here $\dot{M}$ is the accretion rate, r the radial distance, and ν_t the kinematic turbulent viscosity.

As an estimate for the viscosity the α-viscosity prescription introduced by Shakura & Sunyaev (1973) is employed:

$$\nu_t = \alpha H c_s = \frac{\alpha c_s^2}{\Omega}, \tag{20}$$

where the pressure scale height $H = c_s/\Omega$ was used to expresses the kinematic turbulent viscosity ν_t through the local speed of sound $c_s = \sqrt{\partial p/\partial\rho}$ and the Kepler rotation frequency $\Omega = \sqrt{GM_*/R^3}$. The constant α is on the order of 10^{-2} for turbulent flow.

With a given viscosity it is possible to calculate the surface density and the effect of the viscous dissipation on the temperature.

2.5. Viscous Dissipation

The significant turbulent viscosity suggests that heat dissipation needs consideration in the energy balance, especially for active disks. In contrast to Flock et al. (2016) this effect is included in this paper by introducing the heating term in the equation for the evolution of the internal energy. The viscous heating term can be obtained from the Navier–Stokes equation by taking the scalar product with the velocity field. This yields an additional term Q_{heat} in (5):

$$\partial_t\rho\epsilon = -\sigma c(a_R T^4 - E_R) - \nabla\cdot\boldsymbol{F}_* + Q_{\mathrm{heat}}, \tag{21}$$

with

$$Q_{\mathrm{heat}} = \boldsymbol{\sigma}\colon \nabla\boldsymbol{v}, \tag{22}$$

where ":" denotes a double contraction. In spherical coordinates assuming a dominant azimuthal velocity the expression of (22) simplifies to

$$Q_{\mathrm{heat}} = \rho\nu_t[r\ \partial_r\ \Omega]^2. \tag{23}$$

The effect of this new term is discussed in Section 4.1.

2.6. Thermal Conduction

Since momentum eddy diffusivity and heat transfer eddy diffusivity are linked through the turbulent Prandtl number $Pr_t = c_p\nu_t\rho/k_t = \mathcal{O}(1)$, the effect of thermal conduction should have a similar impact on the internal energy as the effect of viscous dissipation and therefore will also be considered. This new addition to the model will be shown to be important for the higher accretion rates studied in this paper. Here k_t is the turbulent thermal conductivity and c_p is the specific heat at constant pressure. This yields for k_t

$$k_t = \frac{\rho \nu_t \Gamma c_V}{Pr_t}, \tag{24}$$

where $c_p = \Gamma c_v$, with Γ being the adiabatic index. The addition of the turbulent heat conduction changes Equation (5) to

$$\partial_t \rho\epsilon = -\sigma c(a_R T^4 - E_R) - \nabla \cdot \boldsymbol{F}_* + Q_{\text{heat}} + Q_{\text{cond}}, \tag{25}$$

with

$$Q_{\text{cond}} = k_t \nabla^2 T. \tag{26}$$

The changes through thermal conduction will be addressed in Section 4.1.

3. Numerical Implementation

This section details the numerical implementation of the above described model as well as the set of initial and boundary conditions. In particular, the boundary conditions pose a delicate problem that needs to be explored tentatively because of their influence on the final solution. Also, a benchmark for a specific set of parameters is presented. The implementation in this paper is partially derived from the model of Flock et al. (2013), but deviates when expedient. The code used in this paper can be found at bitbucket.org/astro_bayreuth/radiation_code. It is written in Matlab/Octave and implicitly solves the radiation hydrodynamic equations.

3.1. Iterative Procedure

The procedure to determine the final disk structure is threefold.

The first step is to calculate the hydrostatic equilibrium for a given temperature distribution using the equations of Section 2.1 to determine the density distribution. For the density in the equatorial plane ρ_0 the surface density and the pressure scale height $H = [k_B T r^3/(GM_* \mu_g u)]^{0.5}$ are used:

$$\rho_0 = \frac{\Sigma}{\sqrt{2\pi} H}. \tag{27}$$

Then, from the midplane outward, density and pressure are integrated. At this point one also calculates the optical depth with formula (12) and the corresponding radiation flux F_*.

The second step is to implicitly solve the two coupled equations for the temperature and radiation field from Section 2.2. This is done using the BiCSTAB solver first presented by Van der Vorst (1992). For preconditioning the incomplete LU-factorization is used, and the convergence criterion is met if the reduction of the L_2 norm of the residual $||\boldsymbol{r}||_2/||\boldsymbol{r}_{\text{init}}||_2$ is $<10^{-5}$. This deviates from Flock et al. (2013) where the matrix is Jacobi preconditioned, but faster convergence is found with incomplete LU-factorization.

The final step is to calculate the dust-to-gas ratio with formula (16). After these three steps, the process is repeated starting again with the hydrostatic equilibrium using the newly obtained temperature distribution. The iterations are continued until the relative change of temperature and density field

$$\max\left(\max\left(\frac{T^n - T^{n-1}}{T^{n-1}}\right), \max\left(\frac{\rho^n - \rho^{n-1}}{\rho^{n-1}}\right)\right),$$

which is used as the convergence criterion, reaches a steady state.

For stability it has been found that it is advantageous to introduce the dust-to-gas ratio logarithmically in the first 30 steps of the iteration. The calculation begins with no dust present and then the effect is slowly introduced. This was done in Flock et al. (2016) as well, but only for the first five iterations. It is necessary to introduce the dust slower because of the different grid spacing. The grid is equidistantly spaced in radial and polar direction, in contrast to Flock et al. (2016), where a logarithmically spaced radial grid is employed. Therefore, to compensate for the bigger grid cells in the inner region, the model needs more steps to equilibrate during the dust introduction. Furthermore, up to three different time steps are used, initially smaller ones dt_1 for N_1 iterations then bigger ones dt_2 for N_2 iterations and finally again smaller ones dt_3 for N_3 iterations. This way the code converges into a stable configuration with less iterations. The small steps $dt_1 = dt_3$ are chosen as 10^4 s or 0.0056 inner orbits, while the bigger ones dt_2 are 10^{12} s or 560 thousand inner orbits in the benchmark case and 10^7 s or 5.6 inner orbits in all later cases.

3.2. Initial and Boundary Conditions

As stated in the previous section there is initially no dust present and the dust-to-gas ratio is zero everywhere. Therefore, the initial temperature distribution is that of an optically thin gas:

$$T_{\text{thin}}(r) = \left(\frac{1}{\epsilon_{\text{gas}}}\right)^{0.25} \left(\frac{R_*}{2r}\right)^{0.5} T_*, \tag{28}$$

with $\epsilon_{\text{gas}} = 1$. Using the initial temperature the surface density can be calculated using Equation (19). (Note that for the benchmark presented below the density has been set constant.) Then the density can be integrated. The initial condition for the radiation energy density is $E_R = a_R T^4$ with the radiation constant a_R.

The boundary condition for the temperature field is zero gradient on all four edges. For the energy density the boundaries are fixed. At the outer edge $E_R = 3.4255 \cdot 10^{-6}\ \text{J/m}^3$, which is equivalent to about 260 K. This is the temperature of the outer edge in Flock et al. (2016) and also close to the analytical expression in Ueda et al. (2017). At the inner edge the condition is

$$E_R = (1 - e^{-\tau_0}) a_R T^4_{\text{thin}}(r_{\min}), \tag{29}$$

which accounts for the optical depth up to the inner boundary, and uses ϵ_{gas} since there is no dust present in proximity to the star.

Along the upper and lower radial boundaries the problem is more complex. While the gas is still optically thin, the boundary condition is given by inserting (28) in (29) with a modified ϵ that includes the dust-to-gas ratio:

$$\epsilon = \frac{\kappa_{\text{gas}} + f_{\text{d2g}}\, \kappa_{\text{dust}}(\nu_{\text{rim}})}{\kappa_{\text{gas}} + f_{\text{d2g}}\, \kappa_{\text{dust}}(\nu_*)}. \tag{30}$$

This method is used up to the transition radius $r_{\text{trans}} = 0.83$ au that was calculated with expressions from Ueda et al. (2017), specifically Equations (6), (17), and (19) therein. For these calculations a ratio between surface height and pressure scale

Table 1
Model `S100` Setup Parameters

Parameter	Value
Surface density	100 g cm^{-2}, uniform
$N_r \times N_\theta$	1280 × 129
$[r_{\min}, r_{\max}]$	[0.2 au, 4 au]
$[\theta_{\min}, \theta_{\max}]$	$[\pi/2 - 0.18, \pi/2 + 0.18]$
Stellar parameter	$T_* = 10{,}000$ K, $R_* = 2.5 R_\odot$, $M_* = 2.5 M_\odot$
Dust-to-gas ratio	$f_0 = 0.01$
Time steps	$dt_1 = 10^4$ s, $dt_2 = 10^{12}$ s
Iterations	$N_1 = 40$, $N_2 = 20$

height $z_*/H = 3.6$ is used. For the temperature in this region Equation (21) from Ueda et al. (2017) can be modified to

$$T = \left\{\frac{2}{\pi}\left[\arctan\left(\frac{r_{\text{trans}} - r}{h}\right) + \frac{\pi}{2}\right]\right\}^{1/4} T_{\text{trans}}, \tag{31}$$

where T_{trans} is the temperature at r_{trans} and $h = 0.04\, r_{\text{trans}}$.

This holds true until $T < T_{\text{flaring}}$, with

$$T_{\text{flaring}} = \frac{550\text{ K}}{r_{\text{au}}^{3/7}} \tag{32}$$

being the flaring disk approximation from Chiang & Goldreich (1997). The value of 550 K is also taken from Flock et al. (2016) and r_{au} is the radius in astronomical units. Then the temperature T_{flaring} is used. All these temperatures are transformed into the corresponding radiation energy values analog to (29) with the optical depth being capped at unity.

3.3. Benchmark

To verify the compliance of the code with previous results a benchmark against the `S100` run from Flock et al. (2016) is presented. In this simulation both viscous heating as well as thermal conduction are neglected, and the run uses a constant surface density in every iteration for comparability. This is the same setup as was used in the run that it is compared against. The parameters used are listed in Table 1. They are typical for a Herbig Ae class star (van den Ancker et al. 1998). The dust-to-gas ratio is fixed after the 40 small steps for faster convergence.

The resulting radial temperature can be seen in Figure 1. The temperatures are in very good agreement corroborating the correctness of the implementation.

Figure 2 represents the 2D profile for a case with thermal conduction and without viscous heating. The parameters used are as listed in Table 2 but with $N_3 = 250$. It shows all the features, like the dust halo, a rounded-off rim, and a shadowed region behind the rim, that were also found in the `S100` run from Flock et al. (2016). It follows that the simulation code used in this paper reproduces both qualitatively as well as quantitatively the results of Flock et al. (2016), giving confidence in the implementation.

4. Results

This section presents the results for cases with viscous heating and thermal conduction, describes the influence of the accretion rate, and analyzes the effect on the structure of the rim.

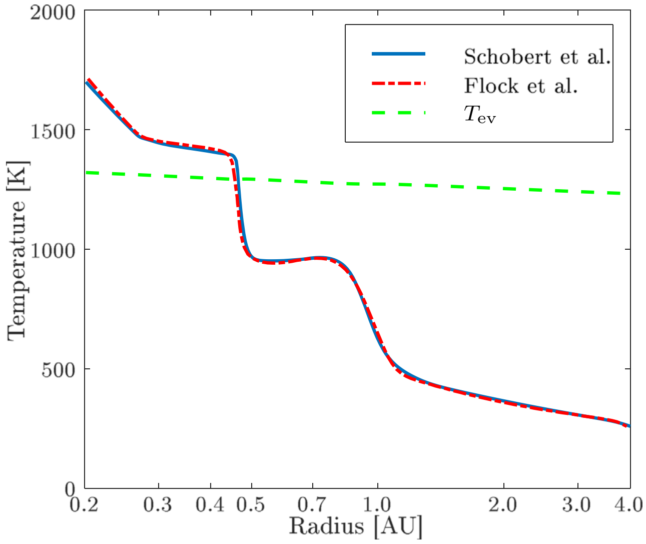

Figure 1. Our midplane radial temperature profile (blue solid line) for model `S100` compared to the temperature profile of Flock et al. (2016) (red dashed −dotted line). The evaporation temperature (green dashed line) is shown for reference.

4.1. Rise in Temperature through Viscous Dissipation and Cooling through Thermal Conduction

As a first step the influence of viscous heating and thermal conduction will be examined. To do so four cases are compared with viscous heating turned on (`VH1`) versus turned off (`VH0`) and thermal conduction enabled (`TC1`) or disabled (`TC0`) with otherwise identical parameters as listed in Table 2.

The accretion rate chosen is $5 \cdot 10^{-8}\, M_\odot\, \text{yr}^{-1}$ to nicely exemplify all effects, and α is set to $0.95 \cdot 10^{-2}$; cases with different α and $\dot{M}$ are explored in the next section. Little is known about the turbulent Prandtl number in accretion disks, but the Prandtl number of hydrogen at temperatures from 700 to 1000 K is 0.68 (McCarty et al. 1981), and it is this value that is used in the model. Furthermore, like α, the Prandtl number is taken to be uniform in the computational domain, and the optical depth in the first cell τ_0 is multiplied with $q_\tau = 0.1$ to prevent the rim from moving outside the computational domain (Flock et al. 2016).

Figure 3 depicts the midplane temperature profiles of the four runs. A significantly hotter inner rim is obtained in the cases with viscous heating, with temperatures reaching the evaporation temperature. In particular, the optically thick regions deviate in temperature from the runs without viscous heating because the heat generated in these regions cannot be radiated away efficiently. The two runs without viscous heating, `TC0VH0` and `TC1VH0`, have almost identical temperature profiles as expected for nonviscous heated cases with the same surface density. The temperature in the shadowed region is elevated through the dissipation as well, and regions with fully evaporated dust begin to appear at around 0.5 au.

Due to the diffusive nature of the heat conduction the radial variation of the temperature is less steep in the `TC1VH1` case compared to `TC1VH0`. The fairly pronounced temperature sink before the rise is still present, and the shadowed regions are also slightly cooler. In general the effect of thermal conduction effectively cools the disk and leads to a significant difference in the profile.

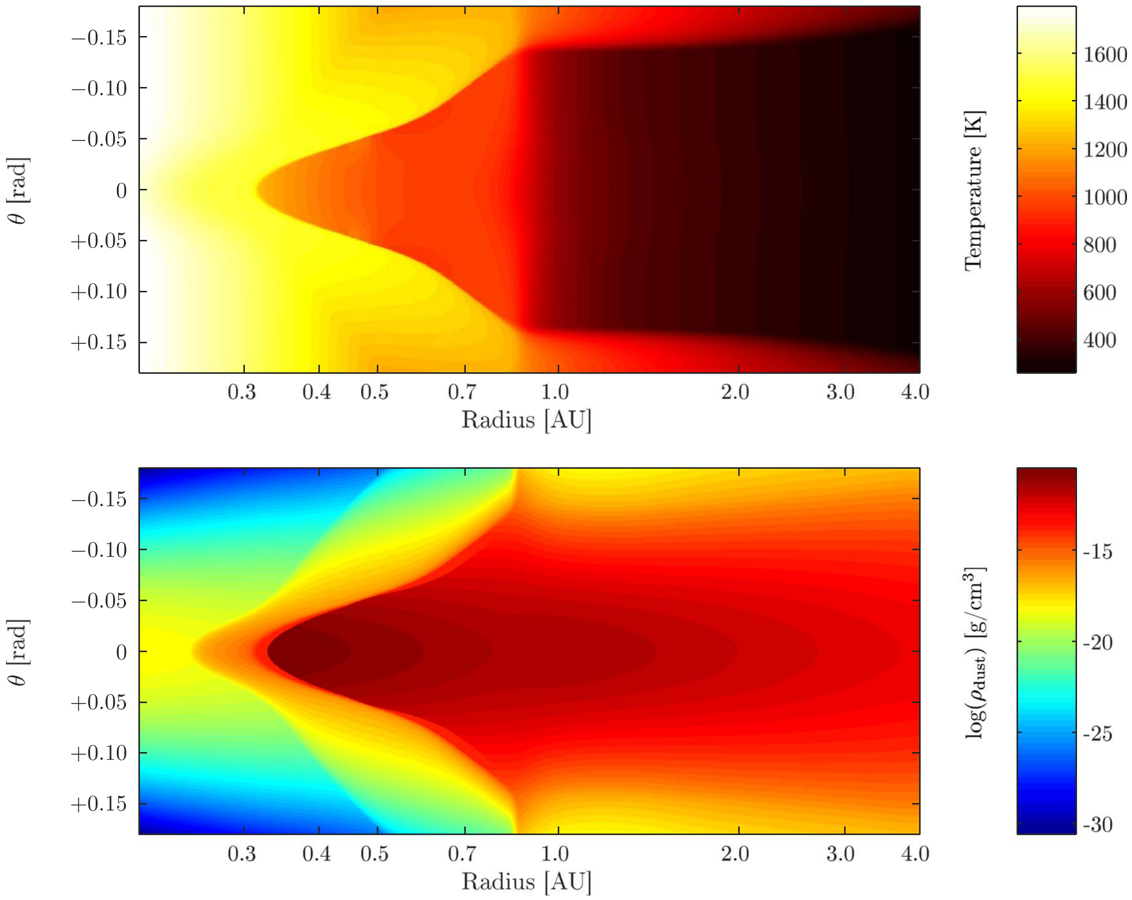

Figure 2. 2D profiles of temperature (top) and the logarithm of the dust density in g cm^{-3} to the base 10 (bottom) for the `jTC1e-7` case. The *y*-axis is the polar angle in rad offset by $\pi/2$ and the *x*-axis the radial distance in astronomical units.

Table 2
Model Setup Parameters for Figures 3 and 4

Parameter	Value
Surface density	$\Sigma(r) = \dot{M}/(3\pi\nu_t)$
$N_r \times N_\theta$	5120×513
$[r_{\min}, r_{\max}]$	[0.2 au, 4 au]
$[\theta_{\min}, \theta_{\max}]$	$[\pi/2 - 0.18, \pi/2 + 0.18]$
Stellar parameter	$T_* = 10{,}000$ K, $R_* = 2.5\,R_\odot$, $M_* = 2.5\,M_\odot$
Dust-to-gas ratio	$f_0 = 0.01$
Time steps	$dt_1 = 10^4$ s, $dt_2 = 10^7$ s, $dt_3 = 10^4$ s
Iterations	$N_1 = 30$, $N_2 = 40$, $N_3 = 50$
q_τ	0.1

4.2. The Influence of the Accretion Rate

All cases in this section consider both viscous heat as well as thermal conduction. All of them have the same surface density (provided that temperatures are equal), but different accretion rates and corresponding α. Three cases are considered with parameters identical to those listed in Table 2.

Since typical accretion rates for Herbig Ae/Be stars are expected to be high, especially in the early stages, the effect of viscous heating is important. Experimental data suggest that accretion rates up to $10^{-6}\,M_\odot\,\mathrm{yr}^{-1}$ are common (van den Ancker 2005) and that 25% of HAe stars have $\dot{M} > 10^{-7}\,M_\odot\,\mathrm{yr}^{-1}$ (Garcia Lopez et al. 2006). For this reason, $\dot{M} = 10^{-7}\,M_\odot\,\mathrm{yr}^{-1}$, $\dot{M} = 5 \cdot 10^{-8}\,M_\odot\,\mathrm{yr}^{-1}$, and $\dot{M} = 10^{-8}\,M_\odot\,\mathrm{yr}^{-1}$ are chosen for models `mdot1e-7`, `mdot5e-8`, and `mdot1e-8`, respectively.

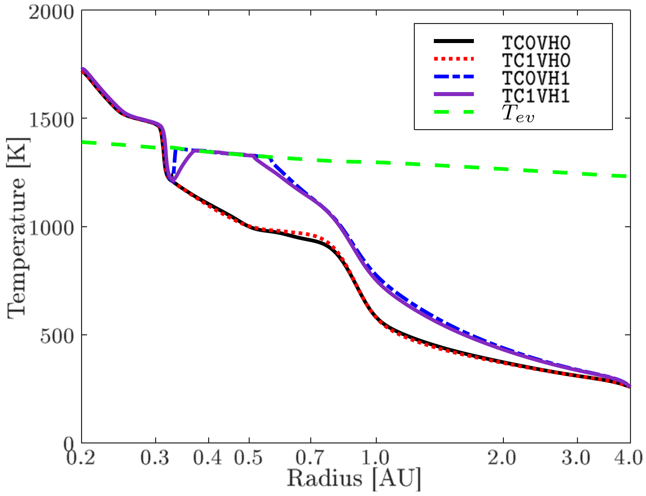

Figure 3. Comparison of four radial temperature profiles of runs including viscous heating (`VH1`) and/or thermal conduction (`TC1`), the black solid line is for the model `TC0VH0`, the red dotted line is for `TC1VH0`, the blue dashed −dotted line is for `TC0VH1`, and the purple solid line is for `TC1VH1`. The evaporation temperature (green dashed line) is shown for reference.

In order for all cases to have the same surface density, α is chosen to be $1.9 \cdot 10^{-2}$, $\alpha = 0.95 \cdot 10^{-2}$, and $1.9 \cdot 10^{-3}$ for the `mdot1e-7`, `mdot5e-8`, and `mdot1e-8` cases,

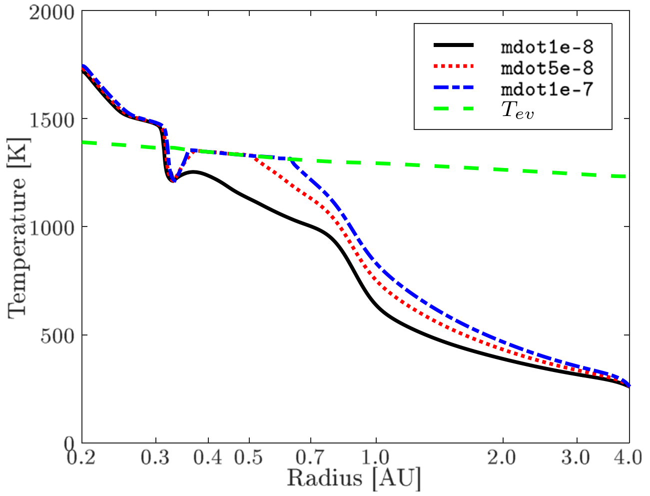

Figure 4. Comparison of three radial temperature profiles of runs including viscous heating and thermal conduction, but with different accretion rates; the black solid line is for the model `mdot1e-8`, the red dotted line is for `mdot5e-8` (note that this is identical to `TC1VH1`), and the blue dashed −dotted line is for `mdot1e-7`. The evaporation temperature (green dashed line) is shown for reference.

respectively. These represent realistic values for thin disks (King et al. 2007; Davis et al. 2010). Furthermore, α is constant throughout the whole box.

The midplane temperature profiles of all three runs are depicted in Figure 4. For the `mdot1e-8` case, the temperature no longer reaches the evaporation temperature, but the other two still have an area where the dust is fully evaporated. The area, where all the dust is evaporated, has a wider extent in the case with an higher accretion rate.

These gaseous regions could be ionized and MRI active, thus vindicating the high values for α that are used in the setup. Although the temperature at which the MRI sets in depends on various parameters, like gas density and dust-to-gas ratio (Umebayashi & Nakano 1988; Desch & Turner 2015), a typical value is 1000 K. Both runs with viscous heating turned on are well above this mark before 1 au.

The position of the dust rim ($\tau_r^* = 1$) does not change for different accretion rates, as seen in Table 3. For all three cases the rim lies at 0.29 au, since its position is determined by the surface density in the gaseous disk and these are identical for all three models.

The dead zone edge ($T_{\mathrm{mid}} = 1000$ K), the point where the MRI is no longer dominant, lies further from the star as the accretion rate increases. The range is 0.70–0.87 au, and in particular, the value for `mdot1e-7` 0.87 au is in good agreement with the value that was found in Flock et al. (2016) for `MDe-7` of 0.86 au. It lies further outward because the viscous heating can maintain a larger hot section for stronger accretion rates.

4.3. Structure of the Rim

The structure of the rim is affected by the viscous dissipation and turbulent heat conduction. It still displays four distinct regions as found by Flock et al. (2016) but has a very different thermal and density profile as can be seen in Figure 5 for the `mdot1e-7` case. Depicted is the `mdot1e-7` case with parameters as in Table 2, but $N_2 = 1$ and $N_3 = 135$. This is the case at an earlier stage than previously to show the development of the dust-free zone inside the rounded-off rim.

Table 3
Model Results for Different Accretion Rates

Model	$\tau_r^* = 1$	$T_{\mathrm{mid}} = 1000$ K
`mdot1e-8`	0.29	0.70
`mdot5e-8`	0.29	0.82
`mdot1e-7`	0.29	0.87

Note. Model name, position of dust rim ($\tau_r^* = 1$), and position of the dead zone edge ($T_{\mathrm{mid}} = 1000$ K) in astronomical units.

The first region is a dust-free inner zone that follows the optically thin gas temperature and lies inward of 0.25 au.

The next zone is the dust halo where the dust-to-gas ratio gradually rises before the condensation temperature is reached at 0.35 au.

Following that is the condensation front that engulfs the third region. This section is formed by the rounded-off rim and in its center can be an active zone that reaches the condensation temperature through the viscous dissipation. This is the exact opposite of a dead zone, a zone where temperature is too low for MRI to arise. This region can reach MRI capable conditions and is kept at high temperature because of the resulting high viscosity in combination with the high optical thickness that does not allow for effective radiative cooling.

The last and fourth region is the outer disk that is getting colder with radial distance and lies at optical depth beyond unity. The part of this region that is close to the equatorial plane is warmer than the higher altitudes; the outer disk is not isothermal at constant radius, contrary to the case without viscous heating.

Potentially there are two stable states that can be reached by a protoplanetary disk: one with a dead zone, if the viscous heating is insufficient, and the area inside the rounded-off rim cools because no external radiation can heat it and another with an active zone, if the viscous heating is strong enough and the heat is trapped inside the disk. These two cases can be seen in the bottom panel of Figure 6. On the left viscous heating is disabled and the radiation energy density inside the disk is almost in equilibrium with the radiation energy density outside. On the right viscous heating is included and a significant increase of radiation energy density inside the disk is visible. This means the energy created by the viscous heating cannot be radiated away at a sufficient rate through the optically thick rim. That leads to an equilibrium with an active zone. Both cases use parameters as in Table 2, but $N_2 = 3$ and $N_3 = 170$.

Interesting to note is that despite the strong radial temperature gradients no local pressure maximum forms in the midplane. In agreement with Flock et al. (2016) there is no local pressure maximum for constant α; once a temperature-dependent α is introduced a local pressure maximum appears at the location where the viscosity changes. In the model description of this paper the viscosity is uniform, and a rise in the temperature with radius occurs through the viscous heating. This increase in temperature, however, is insufficient for the pressure gradient to change sign.

The top panel of Figure 6 shows the `mdot1e-7` case with parameters as in Table 2, but $N_2 = 3$ and $N_3 = 170$. It shows that the active zone inside the rounded-off rim is in its final size. After the active zone has reached a certain size small temperature deviations start to occur and travel through it.

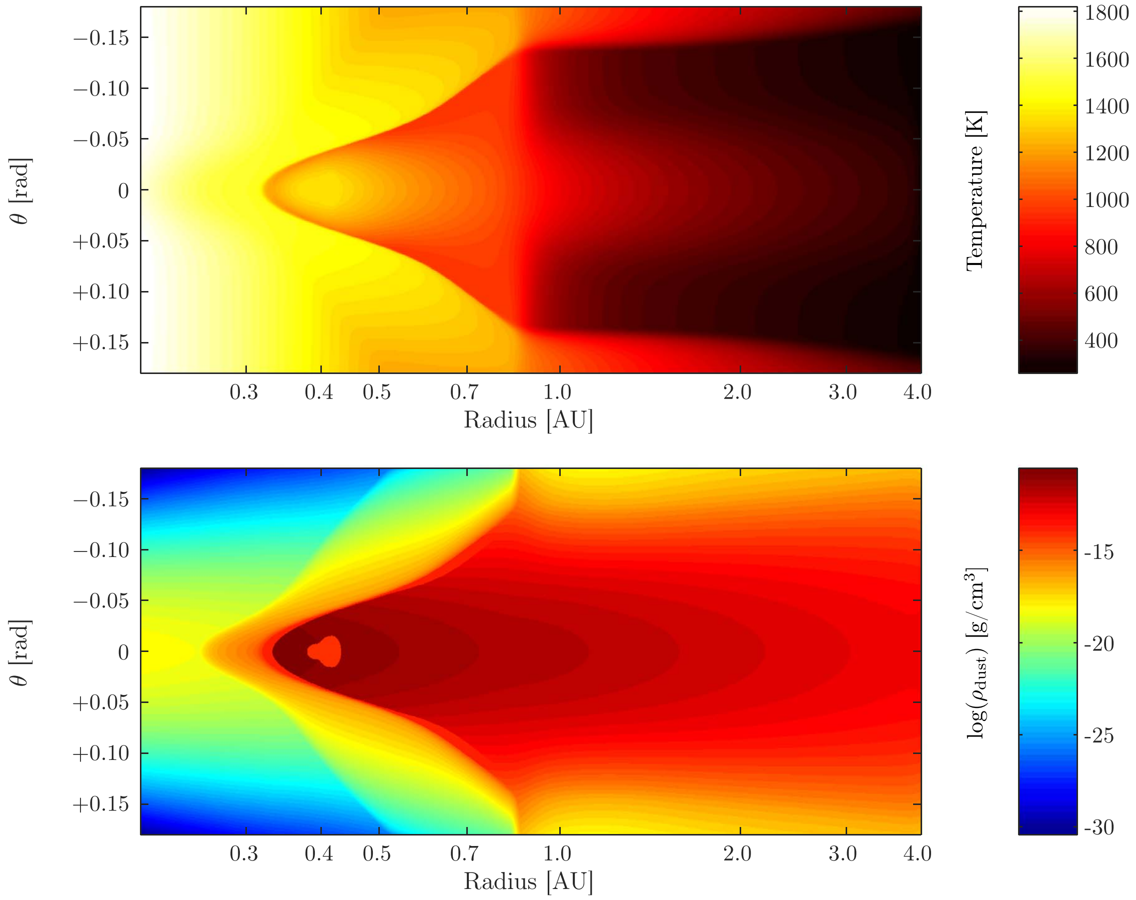

Figure 5. 2D profiles of temperature (top) and the logarithm of the dust density in g cm^{-3} to the base 10 (bottom) for the `mdot1e-7` case at an early stage. The *y*-axis is the polar angle in rad offset by $\pi/2$ and the *x*-axis the radial distance in astronomical units.

These small deviations manifest in the depiction as walls where the dust is present. Since the simulation does not include latent heat it is not possible to decide whether these small deviations have to occur or not, but they were consistently found for every parameter set that produced a dust-free zone.

The surface density in Figure 7 mirrors the cavity that is also present in Figure 6. The dust density falls to $\Sigma_{\text{dust}} \approx 2$ g cm^{-2} in the dust-free zone. To further analyze the equilibrium in the dust-free zone an alternative sublimation formula is in progress.

The optical depth at constant radius

$$\tau_z = \int_{-\infty}^{\infty} \sigma dz \tag{33}$$

for near-infrared radiation in Figure 8 suggests that the dust-free zone forms after a large enough depth in the θ direction is reached because diffusion of radiation energy is no longer sufficient to cool the disk.

5. Discussion

This work represents an early stage in developing a self-consistent model of the inner rim of protoplanetary disks. In this section some important limitations of the model will be discussed.

The simplifications introduced in Flock et al. (2016), such as a uniform dust-to-gas ratio in the shadowed region and a non-frequency-dependent gas opacity are also applied in this work. A more elaborate sublimation formula is needed in the future, especially with respect to the dust-free cavity inside the disk. A detailed implementation of gas line radiation transfer would go beyond the scope of this work. Further, the value of α was chosen to be constant throughout the box. However, the strength of the turbulence is expected to be influenced by the temperature and could be lower in MRI inactive regions (Lesur et al. 2014; Turner et al. 2014; Simon et al. 2015). A temperature-dependent α will be explored in further work.

The temperature deviations and dust walls described at the end of Section 4.3 will have to be further scrutinized in combination with the modeling of the dust-to-gas ratio. Small differences in the temperature can lead to significant changes in the dust-to-gas ratio around the sublimation temperature. This is therefore a delicate problem that needs to be explored tentatively and might necessitate the inclusion of further effects like dust diffusion, latent heat, and temperature-dependent viscosity.

6. Conclusions and Outlook

This paper presents a 2D model for protoplanetary disks that consistently includes viscous heating and thermal conduction. The model expands previous works (Flock et al. 2016) and explores new parameter ranges that led to qualitatively new results. These results are:

(1) For accretion rates $\dot{M} \geqslant 3 \cdot 10^{-8} M_\odot$ yr^{-1} the viscous dissipation cannot be neglected. It affects all regions and

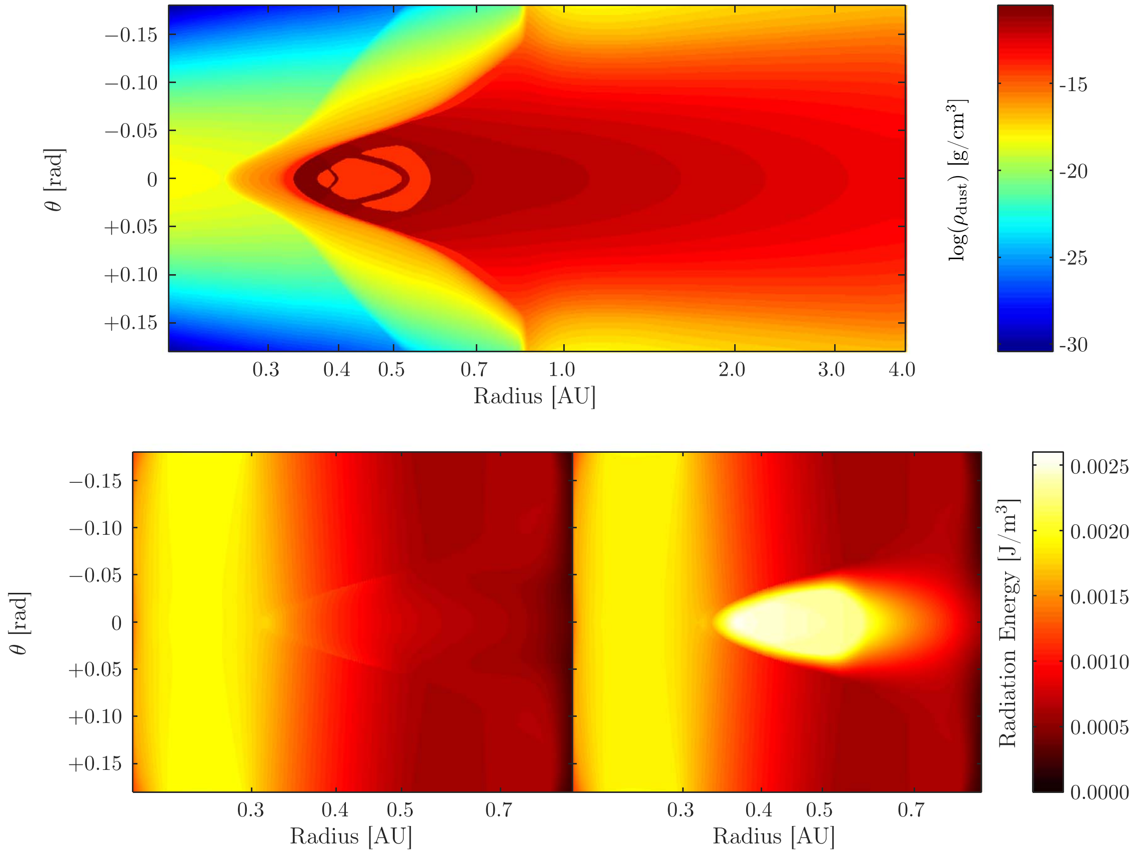

Figure 6. 2D profile of the logarithm of the dust density in g cm^{-3} to the base 10 (top) for the `mdot1e-7` case at a late stage with waves visible and a comparison of the radiation energy densities (bottom) of the `jTC1e-7` case (left) and the `mdot1e-7` case. The *y*-axis is the polar angle in rad offset by $\pi/2$ and the *x*-axis the radial distance in astronomical units.

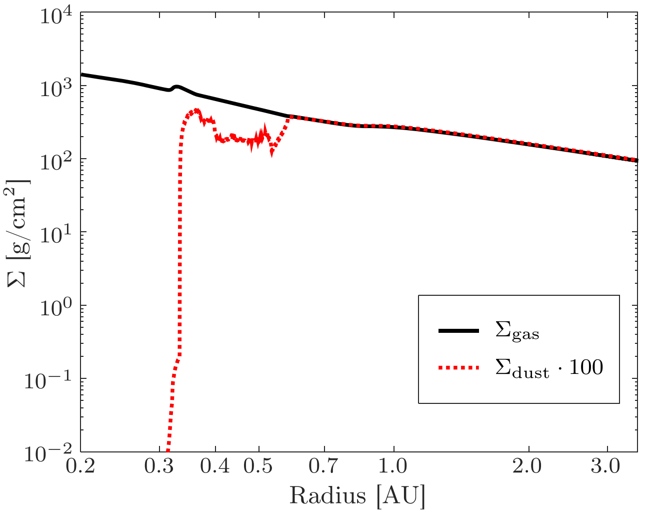

Figure 7. Comparison of gas (solid line) and dust (dotted line) surface density for model `mdot1e-7`.

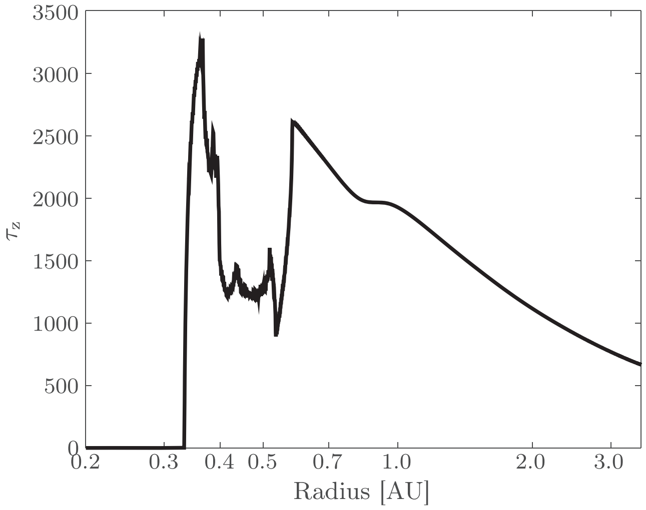

Figure 8. Vertical optical depth in NIR for model `mdot1e-7`.

can cause an MRI active zone to form behind the condensation front.

(2) The thermal conduction is important since high radial temperature gradients exist through the accretion heating. The cooling through thermal conduction is a significant part in the energy balance of the disk; it can therefore also not be neglected for the parameters used.

(3) Despite the strong radial temperature gradients no local pressure maximum forms in the midplane. Therefore, the model calculations do not provide for a region where the radial drift of grains generated by the friction with the gas is reversed (Guilera & Sándor 2017).

(4) The inner rim position is not affected by viscous heating but is determined by the surface density.

(5) The dead zone edge shifts radially outward for higher accretion rates because of a larger zone with viscous heating.

The code used to produce these results can be found at bitbucket.org/astro_bayreuth/radiation_code.

This model could be expanded through temperature-dependent viscosity or thermal conductivity and embedded it in a computationally more demanding 3D simulation. Also a subsequent paper is devoted to study the spectral energy densities produced by active disks. But this lies outside the scope of this work.

References

Balbus, S. A., & Hawley, J. F. 1998, RvMP, 70, 1

Chiang, E. I., & Goldreich, P. 1997, ApJ, 490, 368

Clarke, C. J., & Carswell, R. F. 2009, Principles of Astrophysical Fluid Dynamics (Cambridge: Cambridge Univ. Press),

D'Alessio, P., Cantó, J., Calvet, N., & Lizano, S. 1998, ApJ, 500, 411

Davis, S. W., Stone, J. M., & Pessah, M. E. 2010, ApJ, 713, 52

Desch, S. J., & Turner, N. J. 2015, ApJ, 811, 156

Dullemond, C. P., Dominik, C., & Natta, A. 2001, ApJ, 560, 957

Flock, M., Fromang, S., González, M., & Commerçon, B. 2013, A&A, 560, A43

Flock, M., Fromang, S., Turner, N. J., & Benisty, M. 2016, ApJ, 827, 144

Garcia Lopez, R., Natta, A., Testi, L., & Habart, E. 2006, A&A, 459, 837

Guilera, O. M., & Sándor, Z. 2017, A&A, 604, A10

Herbig, G. H. 1960, ApJS, 4, 337

Isella, A., & Natta, A. 2005, A&A, 438, 899

Keppler, M., Benisty, M., Müller, A., et al. 2018, A&A, 617, A44

King, A. R., Pringle, J. E., & Livio, M. 2007, MNRAS, 376, 1740

Kretke, K. A., Lin, D. N. C., Garaud, P., & Turner, N. J. 2009, ApJ, 690, 407

Lesur, G., Kunz, M. W., & Fromang, S. 2014, A&A, 566, A56

Levermore, C. D., & Pomraning, G. C. 1981, ApJ, 248, 321

Li, A., & Draine, B. T. 2001, ApJ, 554, 778

McCarty, R. D., Hord, J., & Roder, H. M. 1981, Selected Properties of Hydrogen (Washington, DC: U.S. Government Printing Office)

Müller, A., Keppler, M., Henning, T., et al. 2018, A&A, 617, L2

Shakura, N. I., & Sunyaev, R. A. 1973, in IAU Symp. 55, ed. H. Bradt & R. Giacconi (Dordrecht: Reidel), 155

Simon, J. B., Lesur, G., Kunz, M. W., & Armitage, P. J. 2015, MNRAS, 454, 1117

Turner, N. J., Benisty, M., Dullemond, C. P., & Hirose, S. 2014, ApJ, 780, 42

Ueda, T., Okuzumi, S., & Flock, M. 2017, ApJ, 843, 49

Umebayashi, T., & Nakano, T. 1988, PThPS, 96, 151

van den Ancker, M. E. 2005, High Resolution Infrared Spectroscopy in Astronomy (Berlin: Springer), 309

van den Ancker, M. E., de Winter, D., & Tjin A Djie, H. R. E. 1998, A&A, 330, 145

Van der Vorst, H. A. 1992, SIAM J. Sci. Stat. Comput., 13, 631

Wolf, S., & Voshchinnikov, N. V. 2004, CoPhC, 162, 113

Chapter 7

Impact of dust diffusion on the rim shape of protoplanetary disks

B. N. Schobert and A. G. Peeters

This chapter has been published in Astronomy & Astrophysics:

- Schobert, B. N. & Peeters, A. G., 2021, Astronomy & Astrophysics, 651, A27
  URL: `https://doi.org/10.1051/0004-6361/202039398`

A&A 651, A27 (2021)
https://doi.org/10.1051/0004-6361/202039398

Astronomy & Astrophysics

Impact of dust diffusion on the rim shape of protoplanetary disks

B. N. Schobert and A. G. Peeters

Department of Astrophysics, University of Bayreuth, Universitätsstraße 30, Bayreuth, Germany
e-mail: `benjamin.schobert@uni-bayreuth.de`

Received 11 September 2020 / Accepted 2 May 2021

ABSTRACT

Context. Multiple mechanisms are known to give rise to turbulence in protoplanetary disks, which facilitates the accretion onto the central star. Small dust particles that are well coupled to the gas undergo diffusion due to this turbulent motion.
Aims. This paper investigates the influence of turbulence-induced dust diffusion on the equilibrium of protoplanetary disks.
Methods. The model accounts for dust sublimation, radiative transfer with the flux-limited diffusion approximation, and dust diffusion. It predicts the density and temperature profiles as well as the dust-to-gas ratio of the disk.
Results. It is shown that dust diffusion can have a large impact: Assuming the dust survives for 10^4 s or longer before it can be evaporated, this leads the dust diffusion to widen the inner disk considerably. This effect is generated through a feedback mechanism as the diffusion length is much shorter than the disk width. With increasing dust diffusion, the inclination of the inner rim toward the stellar radiation becomes steeper until it is almost vertical. The temperature range of evaporation and condensation, which is linked to the dust composition, has no influence on this effect.
Conclusions. For realistic parameters, dust diffusion cannot be neglected when determining the equilibrium of the disk. Stronger turbulence inside the disk induces more dust diffusion. Therefore, the dust density grows more gradually over a greater distance and less radiation reaches the disk surface. The new equilibrium shape of the disk is more inclined toward the star. This effect is universal and independent of the specific dust composition.

Key words. protoplanetary disks – radiative transfer – diffusion

1. Introduction

Herbig Ae Be stars are intermediate mass stars that are younger than the Sun. They have accretion disks that are believed to be the origin of planets. In recent years the resolution at which protoplanetary disks (PPDs) can be observed has increased, making the inner rim more visible and allowing for constraints on its structure. Lazareff et al. (2017) found the ratio between disk height and radius in the inner disk to be $z/R \approx 0.2$, which is larger than predicted by previous theoretical models (Vinković & Jurkić 2007; Mulders & Dominik 2012) by a factor of approximately two. The shape of the inner rim has long been debated because it determines the physical conditions in the dusty planet-forming region.

In an early development, Dullemond et al. (2001) modeled the inner rim as a cylindrical wall that truncates the disk where the evaporation temperature of the dust is reached. Isella & Natta (2005) took into consideration that this evaporation temperature is dependent on the gas density, which leads to a rounded rim. Flock et al. (2016) then incorporated this function for the evaporation temperature into their radiative transfer model, confirming the structure of the rim. An alternative explanation for a rounded rim that does not rely on a density-dependent T_{ev} involves the different speeds of dust settling for two species of dust particles (Tannirkulam et al. 2007).

The transition between no dust and dust at the inner rim can be especially difficult to resolve because of the high temperature gradient and the significant change in opacity. In Flock et al. (2016) the dust-to-gas ratio was chosen such that not too much star light would be absorbed within a single cell in order to ensure a smooth transition. Using the same dust description, Schobert et al. (2019) found model solutions with interesting feedback loops when considering the absorption of star light. That work found temperature deviations that manifested as dust walls traveling through the disk. As fluctuations in the spectral energy distribution (SED) with periods of days to weeks are a common observation in PPDs (Flaherty et al. 2014), exploring these fluctuations could prove to be insightful. This paper continues to investigate the idea that these fluctuations are related to the treatment of dust at its evaporation temperature. In light of the observed feedback, and to describe the transition at the dust boundary more realistically, this work introduces the effect of diffusion into the description of the dust.

A complete description of the inner rim necessarily includes dust diffusion. Gas accretion is commonly believed to be facilitated by turbulence. This turbulence will inevitably induce diffusion in the dust particles as long as they are strongly bound to the gas. This builds upon the notion that for micrometer dust particles the Stokes number is close to one, and therefore the dust diffusion coefficient will be nearly equivalent to the gas diffusion coefficient (Brauer et al. 2008). Since neither dust formation nor destruction are instantaneous processes, dust will be found slightly outside of its equilibrium position in regard to temperature. The timescale on which dust can be formed or destroyed is of order 10^5–10^7 s (Morfill 1988; Tachibana et al. 2011; Nakamura et al. 2007; Lenzuni et al. 1995). Dust diffusion will therefore take place on that timescale. This addition is also beneficial because it naturally smooths the transition from no dust to dust, which was previously difficult to resolve. Therefore, this paper presents a method of incorporating the diffusive motion of the dust particles into the model from Flock et al. (2016) and Schobert et al. (2019).

A short back-of-the-envelope calculation of the length scale corresponding to dust diffusion, $l_{\rm diff} = 6.5\times10^{-4}$ AU (for details, see Sect. 4.2), suggests that the length scale is negligible to the overall conformation of the inner rim. However, it will be shown in this paper that the impact of dust diffusion is much larger than can be expected from this estimate.

This paper is structured as follows: Sect. 2 explains the model equations introduced to describe the dust diffusion. In Sect. 3 the numerical implementation and convergence criteria are briefly detailed. Section 4 outlines the results and qualitative changes compared to a model without dust diffusion. Section 5 discusses the results in comparison to an analytical prediction and with respect to the rim shape. The paper concludes in Sect. 6 with a summary of the results.

2. Model equations

The model equations used in this work for radiative transfer and hydrostatic equilibrium follow those proposed in Flock et al. (2016) and Schobert et al. (2019). The exact equations and numerical methods are detailed in Schobert et al. (2019). For brevity, only the changes applied to the model compared to Schobert et al. (2019) are outlined in the following section.

2.1. Dust-to-gas ratio

Dust sublimation is of deciding importance for the configuration of the inner rim and thereby for the evolution of the complete disk. Because the dust shields the area behind it from irradiation and because it is heated by the star and the infrared radiation it itself emits, the dust greatly affects the temperature profile of the disk. The transition distance between vapor and condensed dust is very thin and requires special attention.

In order to resolve this thin layer, the dust sublimation formula from Flock et al. (2016) smooths the transition over a temperature range of 100 K and uses the tangens hyperbolicus as a model function. The formula is

$$f_{\rm d2g,old} = \begin{cases} \frac{f_{\Delta\tau}}{2}\left\{1-\tanh\left[\left(\frac{T-T_{\rm ev}}{100\,{\rm K}}\right)^3\right]\right\}\cdot\left\{\frac{1-\tanh(1-\tau_*)}{2}\right\}, & \text{if } T > T_{\rm ev} \\ \frac{f_0}{2}\left\{1-\tanh(20-\tau_*)\right\}+f_{\Delta\tau}, & \text{otherwise,} \end{cases} \tag{1}$$

where $T_{\rm ev}$ is the dust evaporation temperature, f_0 is the reference dust-to-gas ratio, and $f_{\Delta\tau}$ is the transition dust-to-gas ratio. For the dust evaporation temperature, the fitting model proposed by Isella & Natta (2005),

$$T_{\rm ev} = 2000\,{\rm K}\left(\frac{\rho}{1\,{\rm g\,cm^{-3}}}\right)^{0.0195}, \tag{2}$$

is used. It describes the dependence of the evaporation temperature on the gas density for silicate grains. The transition dust-to-gas ratio ($f_{\Delta\tau}$) is defined as

$$f_{\Delta\tau} = \frac{\Delta\tau_*}{\rho_{\rm gas}\kappa_{\rm dust}(\nu_*)\Delta r} = \frac{0.3}{\rho_{\rm gas}\kappa_{\rm dust}(\nu_*)\Delta r}, \tag{3}$$

where Δr is the radial size of one grid cell. The transition optical depth of $\Delta\tau_* = 0.3$ was chosen so that the absorption of the radiation at the rim can be resolved (Flock et al. 2016). This numerical remedy ensures that the transition can be described within each chosen radial resolution; however, it is not necessitated by the physics involved. Furthermore, it is useful for numeric stability to impose a minimum value of $f_{\rm d2g}^{\rm min} = 10^{-10}$. The maximum value of $f_0 = 10^{-2}$ was chosen because it reflects the amount of dust present in the interstellar medium (Li & Draine 2001) and therefore represents the maximum ratio in the PPD.

This method, however, becomes discontinuous if an optically thick area is heated above the evaporation temperature. This was observed in Schobert et al. (2019) in the form of dust waves traveling through the inner hole of the disk. To remove this discontinuity from the description, a new formula for the dust-to-gas ratio is presented in this paper that is simpler and continuous:

$$f_{\rm d2g,new} = \frac{f_0}{2}\left\{1-\tanh\left[\left(\frac{T-T_{\rm ev}}{\Delta T_{\rm dust}}\right)^3\right]\right\}\left\{\frac{1-\tanh(1-\tau_*)}{2}\right\}, \tag{4}$$

where $f_{\Delta\tau}$ was replaced by f_0. This also means that a separation between temperatures above and below the evaporation temperature is no longer necessary because the second case of Eq. (1) is incorporated into the first. It is also preferable to get the same result ($f_{\rm d2g} = f_0$ for low temperatures and high optical depths) as before with just one equation that is continuous. Additionally, a new variable, $\Delta T_{\rm dust}$, is introduced to describe the size of the temperature range over which the dust-to-gas transition occurs. This parameter is dependent on the composition of the dust; in this paper $\Delta T_{\rm dust} = 100$ K is generally chosen, but different values are investigated. This allows the model to be more general. Section 4.3 details the impact of different temperature ranges on the results.

The use of this new formula in the numerical implementation becomes possible by overcoming a pitfall of the previous model: All of the radiation would be absorbed in a single cell if the dust-to-gas ratio were allowed to rise too rapidly. To ensure a smooth transition, the new model now relies on the effect of dust diffusion instead of a staggered dust-to-gas ratio. How dust diffusion was incorporated into the model is explained in the following section.

2.2. Dust diffusion

To derive a description for dust diffusion, one starts with the continuity equation and inserts the advective and diffusive flux components:

$$\frac{\partial\rho}{\partial t} = \nabla\cdot(D\nabla\rho) - \boldsymbol{\nabla}\cdot(\boldsymbol{v}\rho) + R, \tag{5}$$

where ρ is the density, D the diffusion coefficient, $\boldsymbol{v}$ the fluid velocity, and R any source or sink terms necessary for dust description. Because of the relative smallness of the diffusion term, one can neglect it at first and solve the equations for the purely advective case. This leads to the hydrostatic solution for the gas density (Flock et al. 2016; Schobert et al. 2019) and to $\rho_{\rm dust} = f_{\rm d2g}\rho_{\rm gas} = \rho_0$ for the dust density as a best approximation considering that R is not fully known. Inserting this lowest-order solution, ρ_0, into the first-order terms leads to:

$$\frac{\rho_{\rm diff}-\rho_0}{\tau_{\rm diff}} = \nabla\cdot(D\nabla\rho_{\rm diff}) \tag{6}$$

$$\frac{\rho_{\rm diff}-\rho_0}{\tau_{\rm diff}} = D\,\nabla^2\rho_{\rm diff} \tag{7}$$

$$\left[1-D\tau_{\rm diff}\nabla^2\right]\rho_{\rm diff} = \rho_0, \tag{8}$$

where ρ_0 is the lowest-order solution for the density including only advection and $\rho_{\rm diff}$ is the first-order solution including diffusion. A forward differentiation was used together with a typical time of $\tau_{\rm diff}$ to approximate the derivative. Step (7) uses the fact that the gradient length of the mass density is expected to be much smaller than the length scale on which the diffusion coefficient (D) changes. To implement the diffusion, the following two implicit equations are computed via the BiCGStab solver:

$$\left[1 - D\tau_{\text{diff}}\nabla^2\right]\rho_{\text{gas,diff}} = \rho_{\text{gas}} \tag{9}$$

$$\left[1 - D\tau_{\text{diff}}\nabla^2\right]\rho_{\text{dust,diff}} = \rho_{\text{dust}}. \tag{10}$$

Here, the dust-to-gas ratio is $f_{\text{d2g}} = \rho_{\text{dust,diff}}/\rho_{\text{gas,diff}}$, ρ_{diff} is the respective density of dust or gas after one diffusion time step has taken place, τ_{diff} is the typical time it takes for the dust to condensate or evaporate, and D is the diffusion constant of the dust. The idea is that dust particles that are in the process of forming or being destroyed will still be displaced during that time through the intrinsic turbulence or through the gas with which they are very well coupled. One can imagine this as a residual of the dust because its destruction and formation is not instantaneous.

The diffusion constant of the dust is connected to the gas diffusion by the Stokes number, St (Brauer et al. 2008):

$$D_{\text{dust}} = \frac{D_{\text{gas}}}{1 + \text{St}} \approx D_{\text{gas}}. \tag{11}$$

Since St < 1 for small particles, both coefficients approximately match each other (Brauer et al. 2008), and thus $D_{\text{dust}} = \nu = \alpha c_s H$.

Typical condensation times for τ_{diff} range from 10^5 to 10^7 s (Morfill 1988). The formation timescale of chondrules is 10^5 s (Tachibana et al. 2011). The formation timescales of corundum and hibonite range from 10^5 to 10^7 s (Nakamura et al. 2007). Forsterite has been observed to nucleate within 1.4×10^5 s–3.3×10^5 s (Tachibana et al. 2014). Destruction of silicate grains occurs via sublimation and proceeds under quasi-equilibrium conditions (Lenzuni et al. 1995; Duschl et al. 1996). This implies that the evaporation of silicate dust takes an amount of time comparable to that of its formation. It is a useful simplification to assume one diffusion time as the average time of formation since both the exact time the nucleation of dust particles takes and the time their evaporation takes are dependent on the chemistry of the dust composition as well as on the temperature difference between the evaporation temperature and the environment of the particle. In order to still cover a wide range of possible dust compositions, a study on the effect of different formation timescales is performed in Sect. 4.2.

3. Numerical implementation

This section details the numerical implementation of the model described above as well as the convergence criteria. The first step is to determine the density distribution by solving the hydrostatic equilibrium equations for a given temperature profile using the method detailed in Schobert et al. (2019). The second step is to implicitly solve the two coupled equations for the temperature and radiation energy density. This is done using the BiCSTAB solver first presented by Van der Vorst (1992). For preconditioning, the incomplete LU factorization is used. The final steps are calculating the dust-to-gas ratio with Eq. (4) and then executing one diffusive step. The numerical implementation of the dust diffusion is consistent with the calculation of the radiative equilibrium. It is calculated implicitly for gas and dust density using Eqs. (9) and (10), respectively. This is done using both the BiCGStab solver and LU factorization. After these three steps, the process is repeated, starting again with hydrostatic equilibrium and using the newly obtained temperature distribution. The iterations are continued until the convergence criterion is reached.

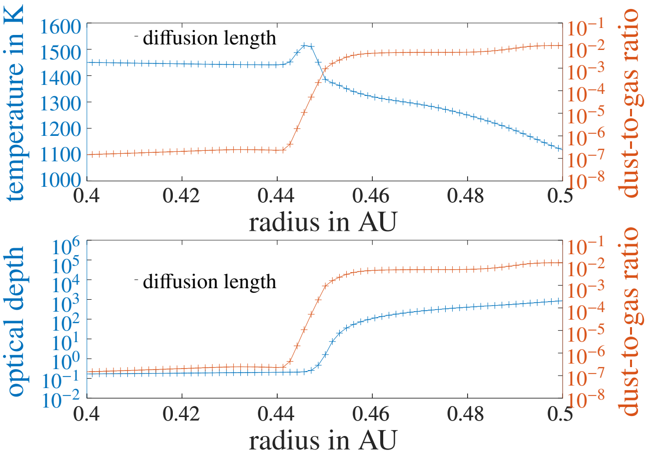

Fig. 1. Midplane profiles for temperature, optical depth, and dust-to-gas ratio. The crosses represent grid points, and the lines are to help guide the eye. The small black line labeled "diffusion length" represents one diffusion length, which is smaller than one radial grid cell.

3.1. Convergence criterion

The convergence criterion used is the same as that in Schobert et al. (2019), where the relative local changes in density and temperature are observed. These normally show an exponential decline in time and converge faster close to the star than farther out because of the dynamical timescale. By the time the outer regions complete several orbits and the disk is vertically isothermal, the inner regions have completed many more orbits and should also be converged. However, some cases were observed where the inner regions showed periodic behavior. This is discussed in detail in Sect. 4.4 and is also consistent with findings from Schobert et al. (2019). In these cases, the disk is considered converged if the outer regions fulfill the convergence criterion and the inner periodic region has completed more than 100 cycles.

3.2. Resolution study

Figure 1 shows the midplane profiles of several key quantities and is zoomed in on the rim transition. The crosses represent grid points at the resolution used in the cases presented in this work. They form continuous, smooth transitions, which are resolved over several grid cells. No jumps or oscillations are visible, and therefore the quantities are well resolved. The critical region in particular, where the optical depth (τ) increases from 0.1 to 10, is resolved over 103 grid points in the midplane. Additionally, to ensure that the numerical resolution is sufficient, a fiducial run at double resolution was performed.

4. Results

This section presents the findings produced by introducing: (i) the new dust-to-gas ratio, (ii) the influence from both diffusion and the temperature range, and (iii) the effect on the waves that were observed with the previous implementation of the dust-to-gas ratio. The model parameters used are listed in Table 1. These values were chosen because they are typical for Herbig Ae stars (van den Ancker et al. 1998). The surface density was determined using the assumption of a steady state with an accretion rate of $\dot{M} = 10^{-8}\, M_\odot\, \text{yr}^{-1}$, except in Sect. 4.4, where the accretion rate is set higher at $\dot{M} = 10^{-7}\, M_\odot\, \text{yr}^{-1}$ to show the

Table 1. General model setup parameters.

Parameter	Value
$N_r \times N_\theta$	2560×257
$[r_{\min}, r_{\max}]$	[0.2 AU, 4 AU]
$[\theta_{\min}, \theta_{\max}]$	$[\pi/2 - 0.18, \pi/2 + 0.18]$
Stellar parameter	$T_* = 10\,000$ K, $R_* = 2.5\,R_\odot$, $M_* = 2.5\,M_\odot$
Dust-to-gas ratio	$f_0 = 0.01$

waves. The lower rate was chosen such that no dust-free hole forms inside the disk, whereas the higher rate includes that feature. In Schobert et al. (2019) it was shown that for accretion rates above $\dot{M} = 10^{-8}\,M_\odot\,\mathrm{yr}^{-1}$ the accretion heating can generate a gaseous inner hole in the dust distribution. Waves in the dust density formed inside this cavity; they are examined in Sect. 4.4.

4.1. Differences through the new dust-to-gas ratio

In Fig. 2 the dust densities for the old (Eq. (1)) and new (Eq. (4)) dust-to-gas ratios are compared. The new dust-to-gas ratio formula changes the configuration of the inner region, specifically at the transition between vaporized and condensed dust. As can be seen in Fig. 2, the transition radius lies closer to the star, moving from 0.55 AU to 0.45 AU. Furthermore, the condensed area is wider in the θ-direction at the transition radius and therefore has a steeper angle toward the stellar radiation.

The regions inward of the transition radius are identical in the two versions; the halo forms in an identical shape and at the same distance from the star. Past 0.8 AU, the models also agree with each other.

At the transition point in the midplane in the right panel of Fig. 2 there is a small line of condensed dust inside the disk. Because the stellar radiation is impinging on the disk that is directly perpendicular to it in the midplane, this point is prone to heat up and condense. In a physical disk with gas turbulence, the dust above and below would be diffused into that line and close this gap. In the following section, this effect is introduced, and even the smallest amount of dust diffusion that we tested effectively mitigates this artifact.

The old dust-to gas ratio kept the amount of dust at the transition artificially small; it used the $f_{\Delta\tau}$ term, such that the absorption of the radiation at the rim could be resolved (Flock et al. 2016). If the amount of dust is artificially diminished, the evaporation front forms farther away from the star. Since $f_{\Delta\tau}$ is a function of the density at each point, the diminishing effect is increased for smaller densities or, equivalently, farther away from the midplane. Removing this artificial factor will therefore move the evaporation closer to the star and, to a greater extent, farther above and below the midplane. These two effects are exactly what we see in Fig. 2. Raising the resolution will increase $f_{\Delta\tau}$ and remedy these effects, beginning in the midplane, as is shown in the appendix of Flock et al. (2016). To completely remedy the effect of $f_{\Delta\tau}$ far above and below the midplane, resolutions that are not obtainable would be necessary. The resolution would need to be increased in both dimensions by at least a factor of 100. Therefore, it is preferable to remove $f_{\Delta\tau}$ from the equation completely. Doing so, however, creates artifacts connected with a poorly resolved radiation absorption, as can be seen in Fig. 2. To remove these artifacts, dust diffusion was introduced as it provides a physically motivated smoothing effect that allows the radiation absorption to be resolved. This was achieved for even for the smallest amount of diffusion tested. Increasing the effect of diffusion to a reasonably motivated amount will change the shape of the rim to an even greater degree, as is discussed in the following section.

4.2. Influence of the diffusion

This section elaborates on the influence of the diffusion. Eight runs with different diffusion times (τ_{diff}) were performed (see Fig. 3). The times were chosen such that they encompass the full possible range of formation times of dust particles as explained in Sect. 2.2. The profiles show where light falling vertically onto the disk reaches an optical depth of unity, which is used as a measure for the height of the disk. The first difference to note is between the two magenta lines, which denote the different ways of calculating the dust-to-gas ratio. With the new formula, Eq. (4) (dashed line), the inner regions of the rim move closer to the star and are more rounded, while the outer regions stay almost unchanged. This is discussed in more detail in Sect. 4.1.

All the profiles with diffusion times given in this section use the new dust-to-gas formula. Comparing the profiles for no diffusion up to a diffusion time $\tau_{\mathrm{diff}} = 10^3$ shows that the change in diffusion time within this range has very little effect on the profile. The starting point in the midplane remains the same; from 0.5 AU to 0.6 AU the profiles deviate slightly from each other, and past that distance they align once again. At first the height slightly decreases with higher diffusion times of up to $\tau_{\mathrm{diff}} = 10^2$, but this trend stops with $\tau_{\mathrm{diff}} = 10^3$, when the height of the disk begins to increase with diffusion time. Overall, the deviances for these four runs are small compared to the ones with higher diffusion times.

Comparing the profiles for diffusion times of $\tau_{\mathrm{diff}} = 10^3$ up to $\tau_{\mathrm{diff}} = 10^6$ shows a stronger influence of diffusion on the profiles. First, the starting point of the profile is closer to the star for higher diffusion times, moving the inner rim inward, and second, the height of the inner regions increases significantly for the closer regions (0.4 AU to 0.5 AU) and moderately for the midregion (0.5 AU to 0.8 AU). The outer regions again align with one another. This leads to a change in the configuration of the disk. While disks at $\tau_{\mathrm{diff}} = 10^2$ have a narrow rounded-off inner region, disks with diffusion times of $\tau_{\mathrm{diff}} = 10^4$ and higher display an enlarged surface of the inner region with a higher grazing angle. Although a higher grazing angle means a larger area facing the star and therefore more absorption of stellar irradiation, this is mitigated by a more diffused and therefore gradual dust transition, and a new equilibrium is found.

It is interesting to note the discrepancy between the expected diffusion length (l_{diff}) and the actual scale of the effect. The typical diffusion length is

$$l_{\mathrm{diff}} = \sqrt{\tau D_{\mathrm{dust}}} \tag{12}$$

and can be used to compare the effect of dust diffusion on the rim shape with what could be expected. For the typical values used in this paper – $\tau = 10^5$ s and $D_{\mathrm{dust}} = 1.27 \times 10^{11}\,\mathrm{m}^2\,\mathrm{s}^{-1}$, calculated as described in Sect. 2.2 – the diffusion length is $l_{\mathrm{diff}} = 1.1 \times 10^8\,\mathrm{m} = 7.5 \times 10^{-4}$ AU. The displacement of the $\tau = 1$ surface as seen in Fig. 3 is an order of magnitude bigger than one diffusion length. This suggests a mechanism that reinforces the effect of diffusion on the rim. The equilibrium disk height with diffusion may potentially be increased further because the radiation from the star is absorbed over a greater distance and more gradually, which allows for a steeper grazing angle in return. The smoother the transition into dust, the steeper the grazing angle can be. This

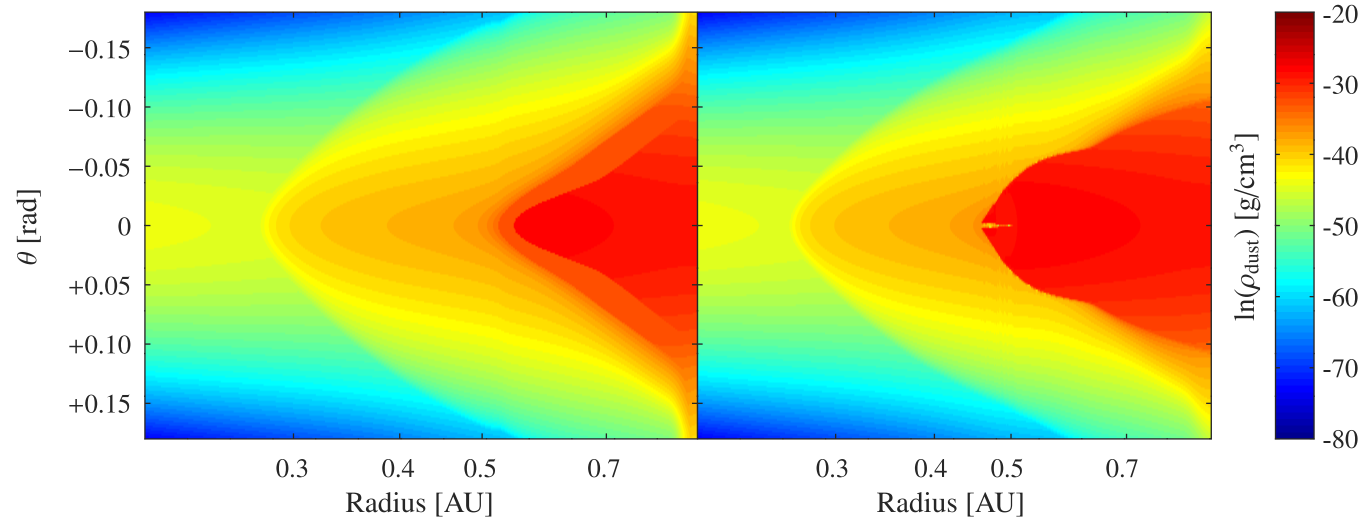

Fig. 2. Comparison of old and new dust-to-gas ratio equations. Depicted is the natural logarithm of the dust density for both cases. The simulation on the left uses the old variant (Eq. (1)), whereas the simulation on the right uses the new (Eq. (4)). The y-axis is the polar angle in rad offset by $\pi/2$, and the x-axis is the radial distance in AU.

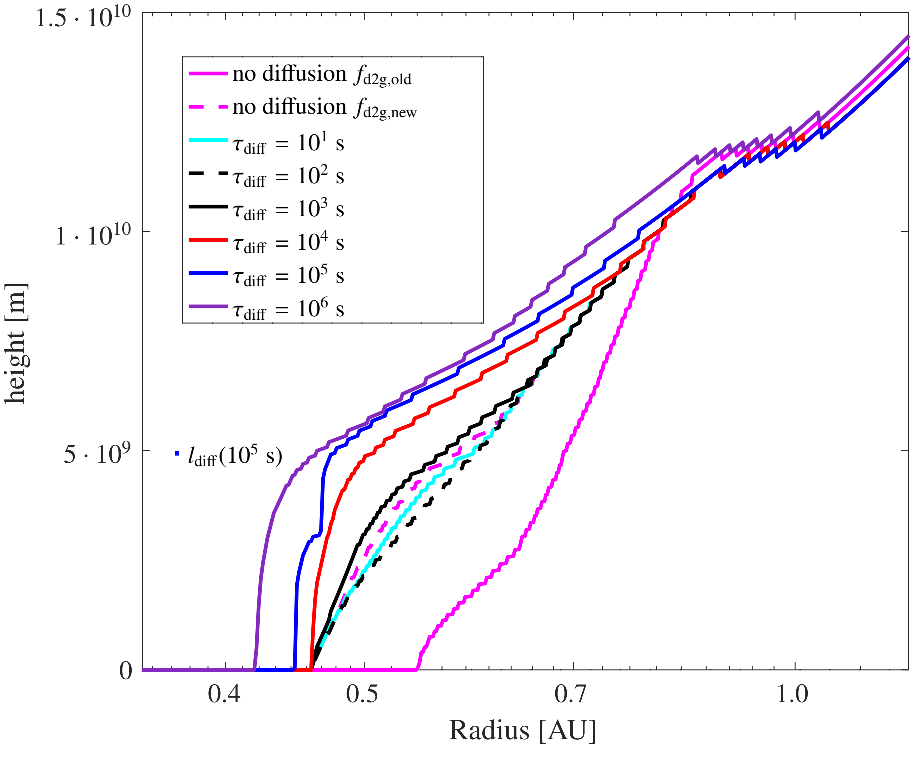

Fig. 3. Comparison of eight radial disk height profiles on different diffusion timescales. Depicted is the height vertically above the midplane where the optical depth measured vertically toward the midplane from the box boundary reaches unity. The two magenta lines are cases with no dust diffusion (i.e., $\tau_{\text{diff}} = 0$) for the old (solid lines) and new (dashed lines) versions of f_{d2g} as described in Sect. 2.1. The six other cases cover the range of diffusion times from 10 s to 10^6 s. The small blue bar to the left represents one diffusion length in the vertical direction for $\tau_{\text{diff}} = 10^5$ s. It is significantly smaller than the change in shape of the corresponding blue profile.

is one explanation for the strong effect of diffusion on the rim shape, which is elaborated on in Sect. 5.2.

4.3. Influence of the temperature range

This section describes the impact of the temperature range ΔT_{dust} over which evaporation occurs. The parameter is introduced in Eq. (4), and its default value is 100 K. Figure 4 shows a comparison between three otherwise identical cases where ΔT_{dust} is 50 K (black line), 100 K (red line), and 200 K (blue line), respectively. The figure shows that the magnitude of the temperature range ΔT_{dust} has little impact on the configuration of the rim. All three cases form a flattened structure with a nearly vertical cusp. However, the range does affect the radius at which the condensation front facing the star forms. In the midplane, the front moves inward, from 0.49 AU in the first case to 0.45 AU and 0.37 AU in the second and third, respectively. If dust can condense at a higher temperature due to the larger range, the optical depth measured radially outward from the star grows faster. This means that the region behind the point, where the first dust particles start to appear ($T \approx T_{\text{ev}} - 0.5\Delta T$), receives less irradiation and the condensation front ($T = T_{\text{ev}}$) moves inward.

Different temperature ranges simulate different dust compositions of the disk. Depending on the size of the grains and their chemical components, they evaporate at different temperatures. Since the configuration of the rim is not greatly affected by the

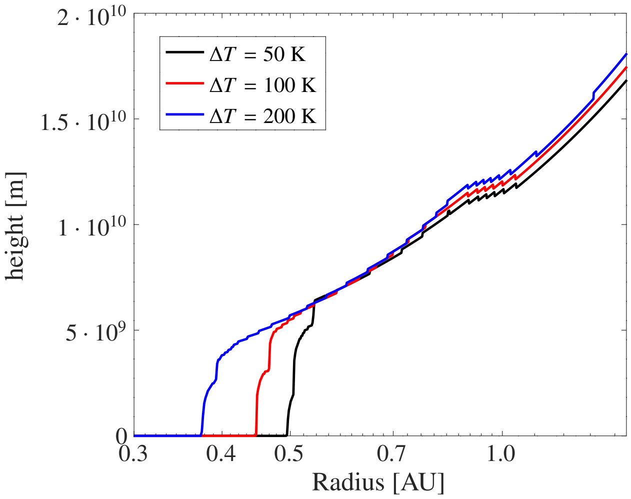

Fig. 4. Comparison of three radial disk height profiles for different evaporation temperature ranges. Depicted is the height vertically above the midplane where the optical depth measured vertically toward the midplane from the box boundary reaches unity. The black line is a case with $\Delta T = 50$ K, the red line represents $\Delta T = 100$ K, and the blue $\Delta T = 200$ K.

temperature range, the findings of this paper can be applied to a wide variety of disks.

4.4. Waves

In this section a case with an increased accretion rate, $\dot{M} = 10^{-7}\,M_\odot\,\mathrm{yr}^{-1}$, is explored. The dust diffusion time (τ_diff) is set to 10^5 s and the temperature range is 100 K.

At these parameters an inner hole forms inside the disk because the heat produced through viscous heating by accretion is sufficiently trapped inside the disk and the midplane heats above the evaporation point, as explained in Schobert et al. (2019). Inside this inner hole, waves in the dust density were traveling through the simulation domain away from the star. However, there are two differences with respect to the case in Schobert et al. (2019). First, the dust walls caused by small temperature deviations that were observed in the previous work are no longer present. This suggests that they were an artifact of the discontinuous dust-to-gas ratio description, as was presumed in that paper. Since the dust-to-gas ratio is less sensitive around the evaporation temperature, a continuous temperature region is present inside the hole with a smooth dust density.

The second difference is that waves in the dust density traverse along the outer perimeter of the disk away from the star. They originate at the closest distance of the disk to the star and then progress away from the star while continuously losing intensity. Eventually they fade into the body of the disk. One such cycle can be seen in Fig. 5. The progression goes from left to right, then from top to bottom, with 3×10^4 s between each panel.

The first step is the formation of a new dust front at the transition radius, which is at approximately 0.3 AU for this case. This front then gradually grows bigger and starts to move radially outward. Once the front is big enough, it splits along the midplane and two separate dust density maxima move along the outer edge of the disk. Along the way, they lose intensity and morph into the disk before they reach 0.4 AU. Once the dust front splits, it leaves the front of the disk open for the next dust front to form, and the cycle continues. Fourier analysis of the temperature over time at a fixed position in the midplane shows an average dominant wave frequency at 2.19×10^{-6} Hz (i.e., a period of 5.3 days). Coincidentally, fluctuations of a similar period have been observed in protostellar disks (Flaherty et al. 2014). For the shown case, the effect of these density fluctuations on synthetic SEDs of the disk was found to be negligible by Dullemond et al. (2012) using RADMC3D, but the intensity of these waves depends on the diffusion time chosen, as well as the surface density of the disk (which is determined here through the accretion rate). These waves are consistently found for every parameter set but are more pronounced for longer diffusion times as well as higher surface densities.

5. Discussion

This section discusses the results in comparison to another theoretical model and quantifies the effects on rim shape and grazing angle. Synthetic images are shown that represent what different levels of diffusion would look like observationally.

5.1. Theoretical comparison

The cylindrical shape of the rim toward the star is reminiscent of a model previously proposed by Dullemond et al. (2001). This section compares that model to the findings of this paper, specifically the rim radius and rim height.

The rim position was determined in Dullemond et al. (2001) as the radius where radiative equilibrium is reached at the evaporation temperature:

$$R_\mathrm{rim} = \left(\frac{L_*}{4\pi T_\mathrm{rim}^4 \sigma}\right)^{1/2} \left(1 + \frac{H_\mathrm{rim}}{R_\mathrm{rim}}\right), \tag{13}$$

where L_* is stellar luminosity, T_rim the evaporation temperature at the rim, σ the Stefan-Boltzmann constant, and $H_\mathrm{rim} = \chi_\mathrm{rim} h_\mathrm{rim}$ the height of the disk at the rim, which is χ_rim times the pressure scale height at that location. The second factor of this equation takes into account the radiation that is reemitted from the opposing disk area.

To calculate χ_rim, a vertical Gaussian density profile is assumed, as well as a linear behavior of $H(R)/R$ with a slope of $-1/8$ (see Appendix A.3 in Dullemond et al. 2001). Here the surface height is defined to be the height to which the optical depth (τ) of the rim on a radially outward directed ray is greater than one:

$$\begin{aligned} \tau(H_\mathrm{rim}) &= \int_{R_\mathrm{rim}}^{\infty} \rho(R, H_\mathrm{rim}) \kappa_\mathrm{dust}(T_*) f_\mathrm{d2g} \mathrm{d}R = 1 \\ \mathrm{erf}\left(\frac{\chi_\mathrm{rim}^\mathrm{theo}}{\sqrt{2}}\right) &= 1 - \frac{1}{4\Sigma(R_\mathrm{rim}) \kappa_\mathrm{dust}(T_*) f_\mathrm{d2g}}, \end{aligned} \tag{14}$$

where erf(x) denotes the error function and Σ is the gas surface density of the disk.

While in Dullemond et al. (2001) Σ is chosen to be constant, this work has a radially dependent surface density. Therefore, $\Sigma(R_\mathrm{rim})$ needs to be chosen self-consistently to calculate χ, which in turn is needed to iteratively find R_rim with Eq. (13). This yields $\chi_\mathrm{rim}^\mathrm{theo} = 3.69$ and $R_\mathrm{rim}^\mathrm{theo} = 0.64$ AU. However, since the simulation does not take into account the reemitted radiation at the opposing dust rim, it is advantageous for the comparison to neglect the second factor of Eq. (13), which yields $\chi_\mathrm{rim}^\mathrm{theo} = 3.69$ and $R_\mathrm{rim}^\mathrm{theo} = 0.60$ AU. The height ratio χ does not change within two decimals because the change in surface density is small and the radius

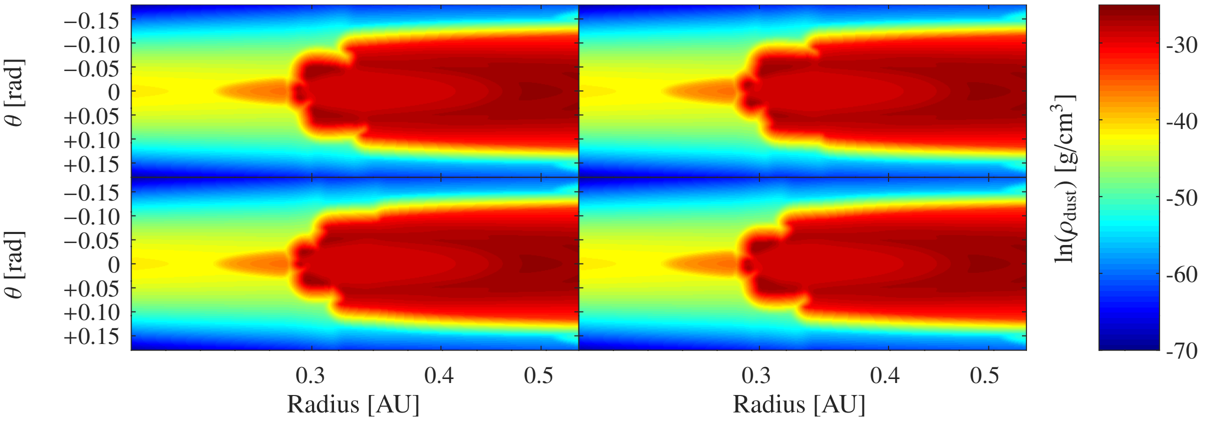

Fig. 5. Evolution of one wave cycle. Depicted is the natural logarithm of the dust density at four points in time. The y-axis is the polar angle in rad offset by $\pi/2$, and the x-axis is the radial distance in AU.

moves slightly inward, as expected if less radiation falls onto the rim. These last two values (i.e., $\chi_{\mathrm{rim}}^{\mathrm{theo}} = 3.69$ and $R_{\mathrm{rim}}^{\mathrm{theo}} = 0.60$ AU) are illustrated in Fig. 6 by the solid line.

For comparison, the same quantities can be calculated from the simulation data, where $R_{\mathrm{rim}}^{\mathrm{sim}}$ is the radius (where the optical depth in the midplane measured from the star reaches one) and $\chi_{\mathrm{rim}}^{\mathrm{sim}}$ is found through the height (where the optical depth at the boundary facing away from the star minus the optical depth at the rim radius reaches one). This yields $\chi_{\mathrm{rim}}^{\mathrm{sim}} = 4.13$ and $R_{\mathrm{rim}}^{\mathrm{sim}} = 0.45$ AU and is illustrated in Fig. 6 by the dotted line. The discrepancy in radius can be explained by the difference caused by slowly increasing the dust-to-gas ratio with the radius as in the simulation and switching from no dust being present to the maximum dust-to-gas ratio in the theoretical model. As more stellar radiation is absorbed closer to the star, the equilibrium point moves inward as well. The same effect was observed in Sect. 4.1: When the discontinuity in the dust-to-gas model was removed, the rim radius moved radially inward. The difference in χ is largely due to the change in pressure scale height with radius. As such, it is conducive to also compare the radians covered by the different heights: $\theta_{\mathrm{sim}} = 0.29$ and $\theta_{\mathrm{theo}} = 0.33$. These two values are in reasonably good agreement with each other, as can be seen in Fig. 6. This comparison shows that while an accurate assessment of course demands a numerical simulation, the analytic estimates provide a good approximation.

Another comparison can be drawn to observational data from Lazareff et al. (2017), where the height of the inner rim was estimated by considering the fraction of the stellar luminosity that is reprocessed to near-infrared radiation (NIR). That approach leads to $z/R \approx 0.2$, which exceeds the predictions of previous hydrostatic models by a factor of two (Vinković & Jurkić 2007; Mulders & Dominik 2012). However, it only exceeds the height of the inner rim that is discussed in this section: $z/R \approx 0.5\,\theta_{\mathrm{sim}} = 0.145$ by 38%. This discrepancy can be due in part to the different methods of evaluating the rim height and the specific choice of parameters for the case presented in this section. Nevertheless, incorporating dust diffusion into hydrostatic models is a possible solution to the mismatch of disk heights in previous simulations and the disk heights observed in Lazareff et al. (2017).

5.2. Rim shape

To characterize the rim shape, it is helpful to divide the rim into two sections. The first one extends from R_1, the radius where the vertical optical depth in the near infrared becomes nonzero and ends at R_2, the radius where the radial optical depth for the star light is one. This region encompasses the very beginning of the disk and is nearly vertical for higher diffusion cases. The angle β_1 is calculated from the disk height at R_2 and the difference between the two radii (R_1 and R_2).

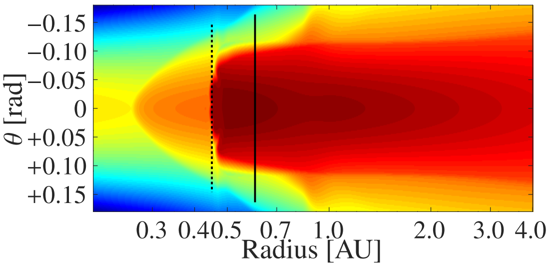

Fig. 6. Comparison between analytical prediction and simulation. The dashed line shows R_{rim} and the disk height calculated from the simulation, and the solid line shows R_{rim} and the disk height calculated as in Dullemond et al. (2001). Depicted is the natural logarithm of the dust density for the case with $\Delta T = 100$ K.

The second section lies beyond R_2 and extends to R_3, the radius where the midplane temperature falls below 1000 K. Corresponding to this section, an angle β_2 can be calculated, which is the average disk angle between R_2 and R_3. The angle β_{total} is the average angle of the disk from R_1 to R_3. The values χ_2 and χ_3 are the ratios of disk height, calculated with the vertical NIRR optical depth, and the pressure scale height at R_2 and R_3.

In Table 2 the values for β_1 suggest that the diffusion does not significantly influence the angle of the first section, up to a diffusion time of 10^2 s. For higher diffusion times, the angle rapidly steepens until it is fully vertical for the final value. The inner radius (R_1) stays identical within two decimals up to a diffusion time of 10^5 s, and then it starts to slowly decrease with increasing diffusion time. Similarly, R_2 moves inward with higher diffusion times, and the distance between these two radii decreases. The effect of the diffusion time on R_3 is small except for the two cases with the largest dust transition ranges, $\tau_{\mathrm{diff}} = 10^6$ s and $\Delta T = 200$ K, where the midplane temperature dropped farther from the star because the heating through irradiation could reach farther inside the disk.

None of the tested cases displayed a shadow cast on the outer region of the disk. The grazing angle always tends to zero before the disk starts to flare again farther out. The change in stellar

Table 2. Properties of the different models discussed in this paper.

Series	Figure	$\tau_{\rm diff}$	$\Delta T_{\rm dust}$	$R_1/\rm AU$	$R_2/\rm AU$	χ_2	z_2/R_2	$R_3/\rm AU$	χ_3	z_3/R_3	β_1	β_2	$\beta_{\rm total}$
Diffusion time	2	0 s	100 K	0.46	0.50	2.03	0.034	0.54	3.49	0.051	23.9°	14.2°	19.0°
		10 s	100 K	0.46	0.50	1.80	0.030	0.54	3.19	0.047	21.3°	13.6°	17.3°
		10^2 s	100 K	0.46	0.49	1.31	0.022	0.54	2.90	0.043	22.7°	12.4°	15.6°
		10^3 s	100 K	0.46	0.46	0.55	0.009	0.53	3.61	0.053	43.6°	19.9°	21.8°
		10^4 s	100 K	0.46	0.47	2.09	0.034	0.52	4.72	0.068	69.6°	19.9°	30.7°
		10^5 s	100 K	0.45	0.45	1.78	0.029	0.53	5.27	0.076	83.4°	19.5°	27.0°
		10^6 s	100 K	0.42	0.42	0.48	0.008	0.78	5.21	0.092	90.0°	10.8°	11.3°
Temperature range	3	10^5 s	50 K	0.49	0.50	0.65	0.011	0.56	5.20	0.078	74.1°	30.5°	33.2°
		10^5 s	200 K	0.37	0.38	1.18	0.018	0.78	4.90	0.086	77.3°	8.6°	9.4°

flux absorbed per unit distance monotonously decreases with the radius. This is in contrast to the theoretical model from the previous section. Heating by accretion keeps the disk hot enough to not collapse into a shadowed region.

The change in the rim shape due to the diffusion of dust is quite dramatic compared to expectations informed by the diffusion length. As mentioned in Sect. 4.2, the displacement of the transition in the vertical direction is two orders of magnitude larger then predicted. Because the transition between evaporated and condensed dust is such a delicate problem, with repercussions for all areas behind it, even small differences can inform a significant change in the overall configuration. Therefore, dust diffusion plays an important role in the formation of the inner rim.

The introduction of dust diffusion allows dust to exist for a short period of time outside of areas where the previous model (without dust diffusion) had predicted it. This newly displaced dust will have a cooling effect on everything in its shadow. More dust particles can form because of the lower temperature in these areas, enhancing the dust-to-gas ratio and thus shifting the position of the dust-to-gas transition. Dust will be displaced by diffusion once again until equilibrium is reached. The shape of the rim is substantially altered through dust diffusion, although the diffusion length is small compared to this change. However, the diffusion length is not small compared to all important scale lengths. The critical distance over which the dust-to-gas transition occurs is comparable to the diffusion length.

5.3. Synthetic images

To provide a realistic view of the rim, synthetic images were created using the RADMC3D code from Dullemond et al. (2012). Figure 7 shows the intensity at a wavelength of 2 µm for a disk with a diffusion time $\tau_{\rm diff} = 0$ s or diffusion turned off (upper panel) and a disk with $\tau_{\rm diff} = 10^5$ s representing moderate diffusion (lower panel). The disks are viewed from above at an angle of 60° from face-on orientation, and as such the rim can be seen. The luminosity from the star itself is suppressed and the flux conservation is of second order.

The case without diffusion shows a thinner and rounder rim compared to the one with diffusion, in agreement with Fig. 3. The peak luminosity is reached at the rim itself in both cases; however, the maximum is 2.1×10^{-7} erg [s cm^2 Hz ster]$^{-1}$ without diffusion and 3.5×10^{-7} erg [s cm^2 Hz ster]$^{-1}$ with diffusion. This is a 67% increase in luminosity in the rim region.

The total luminosity is 3.12×10^{-4} erg [s cm^2 Hz ster]$^{-1}$ without diffusion and 3.31×10^{-4} erg [s cm^2 Hz ster]$^{-1}$ with diffusion. This is a 6% increase in luminosity in the region of the near-infrared bump.

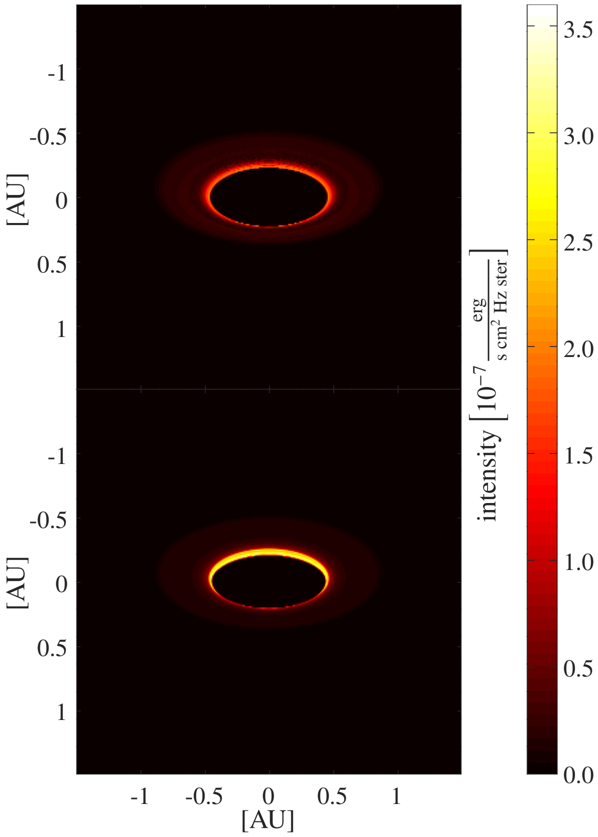

Fig. 7. Synthetic images of the disk, viewed 60° from face-on at 2 µm wavelength. The intensity maps correspond to no diffusion (*top*) and $\tau_{\rm diff} = 10^5$ s (*bottom*).

6. Conclusions

This paper presents a two-dimensional model for PPDs that synchronizes the dust description over all temperature ranges and consistently includes dust diffusion. The model builds upon earlier work (Flock et al. 2016; Schobert et al. 2019), leading to qualitatively new results:

1. Dust diffusion has a far larger impact than a simple estimate of the diffusion length suggests. A feedback effect leads to a more gradual dust transition, which absorbs the stellar radiation along a longer path. This allows for a steeper grazing angle of the inner rim and a wider disk height.
2. Varying the temperature range moves the inner radius, while the general structure of the rim remains unchanged. This

means the model is robust for different possible dust compositions.

3. The intensity emitted by the disk at a wavelength of 2 μm is a function of the diffusion time. It increases significantly at the apex of the rim and increases slightly when averaged over the whole disk.
4. No more waves are observed inside the gaseous hole, unlike what was found in Schobert et al. (2019): those waves were an artifact of the discontinuous dust description.
5. Waves in dust density propagate along the outer perimeter of the disk for higher accretion rates and lower dust diffusion times. They display a period of 5.3 days.

The code used to produce these results can be found online[1].

References

Brauer, F., Dullemond, C. P., & Henning, T. 2008, A&A, 480, 859
Dullemond, C. P., Dominik, C., & Natta, A. 2001, ApJ, 560, 957
Dullemond, C. P., Juhasz, A., Pohl, A., et al. 2012, Astrophysics Source Code Library [record ascl:1202.015]
Duschl, W. J., Gail, H.-P., & Tscharnuter, W. M. 1996, A&A, 312, 624
Flaherty, K. M., Muzerolle, J., Wolk, S. J., et al. 2014, ApJ, 793, 2
Flock, M., Fromang, S., Turner, N. J., & Benisty, M. 2016, ApJ, 827, 144
Isella, A., & Natta, A. 2005, A&A, 438, 899
Lazareff, B., Berger, J.-P., Kluska, J., et al. 2017, A&A, 599, A85
Lenzuni, P., Gail, H.-P., & Henning, T. 1995, ApJ, 447, 848
Li, A., & Draine, B. T. 2001, ApJ, 554, 778
Morfill, G. E. 1988, Icarus, 75, 371
Mulders, G. D., & Dominik, C. 2012, A&A, 539, A9
Nakamura, T. M., Sugiura, N., Kimura, M., et al. 2007, Meteorit. Planet. Sci., 42, 1249
Schobert, B. N., Peeters, A. G., & Rath, F. 2019, ApJ, 881, 56
Tachibana, S., Nagahara, H., Ozawa, K., et al. 2011, ApJ, 763, 16
Tachibana, S., Takigawa, A., Miyake, A., Nagahara, H., & Ozawa, K. 2014, 45th Lunar and Planetary Science Conference, 1226
Tannirkulam, A., Harries, T. J., & Monnier, J. D. 2007, ApJ, 661, 374
van den Ancker, M. E., de Winter, D., & Tjin A Djie, H. R. E. 1998, A&A, 330, 145
Van der Vorst, H. A. 1992, SIAM J. Sci. Stat. Comput., 13, 631
Vinković, D., & Jurkić, T. 2007, ApJ, 658, 462

---

[1] `bitbucket.org/astro_bayreuth/radiation_code`

Chapter 8

Numerical modelling of the inner disk structure of a young stellar object: HD 144432 based on near- and mid-infrared interferometry and spectroscopy

B. N. Schobert, J. Varga, T. Ueda, M. Flock and A. G. Peeters

This chapter has been submitted to Astronomy & Astrophysics.

Astronomy & Astrophysics manuscript no. paperV3
March 26, 2024

Numerical modelling of the inner disk structure of a young stellar object: HD 144432 based on near- and mid-infrared interferometry and spectroscopy

B. N. Schobert[1], J. Varga[2,3], T. Ueda[4,5], M. Flock[4], and A. G. Peeters[1]

[1] Department of Astrophysics, University of Bayreuth, Universitätsstraße 30, Bayreuth, Germany
e-mail: `benjamin.schobert@uni-bayreuth.de`
[2] HUN-REN Research Centre for Astronomy and Earth Sciences, Konkoly Observatory, Konkoly-Thege Miklós út 15-17, H-1121 Budapest, Hungary
[3] CSFK, MTA Centre of Excellence, Konkoly-Thege Miklós út 15-17, H-1121 Budapest, Hungary
[4] Max Planck Institute for Astronomy, Königstuhl 17, D-69117 Heidelberg, Germany
[5] Center for Astrophysics, Harvard & Smithsonian, Cambridge, Massachusetts 02138, USA

Received March 26, 2024

ABSTRACT

Context. Recent observations suggest that many disks around young stellar objects (YSOs) have oversized half-light radii in the mid-infrared region compared to the size-luminosity relation in the near-infrared.

Aims. This paper aims to determine the structure and key properties of a protoplanetary disk, using a physics based model that is constrained by the observations of SED (spectral energy distribution) as well as the visibility in the near and mid-infrared. The results are used to interpret observational data from VLTI/MATISSE.

Methods. The physics based model predicts density and temperature profiles, while self-consistently accounting for dust sublimation and radiative transfer. Synthetic images are produced via ray tracing from these profiles and converted into SEDs and visibility curves. The model parameters are adjusted until the simulated SEDs and visibilities compared well to their observational counterparts.

Results. Reasonable agreement between model prediction and observation is obtained. The 3 μm visibility curve is strongly connected to the inner rim position and there is an easy analytical equation connecting half-width of the visibility to the inner rim position. The 9 μm visibility curve is indicative of the amount of accretion heating within the disk, HD 144432 has a high turbulent viscosity, with $\alpha = 0.04$ and an accretion rate of $\dot{M} = 1.6 \cdot 10^{-8} M_{\odot}\mathrm{yr}^{-1}$. The SED is best reproduced with graphite and silicate particles with sizes in the range of 0.003-1 μm and an absorption to emission ratio of $\varepsilon = 0.11$.

Conclusions. The accretion heating has a important impact on HD 144432 and must be included to explain the large mid-infrared region. It is possible to determine regions where the majority of the near- and mid infrared radiation originates. This corresponds well with measured visibility curves from HD 144432, where longer wavelength radiation, i.e. colder radiation, is observed coming from further away from the star as expected. Furthermore, it is possible to constrain the accretion rate and inner and outer rim radii of the disk, as well as confining possible dust compositions.

Key words. Accretion, accretion disks – protoplantary disks – radiative transfer – Techniques: interferometric – Methods: numerical – Methods: observational

1. Introduction

Accretion disks, made of gas and dust, surround many young stellar objects (YSOs), that have been observed. In order to understand the formation of planetary systems it is necessary to know the structure of the disk itself. This proves especially difficult for the inner regions of the disk, because these are hard to spatially resolve for remote objects using current methods. Within this inner region of the disk, the temperature of the gas gradually drops as a function of the distance to the star and eventually reaches the condensation temperature of the dust. At this point the inner disk rim (Dullemond & Monnier 2010) forms, the evaporation front of the dust suspended in the gas.

Spectra and interferometric examinations of stars and disks enable predictions about the disk's internal structure, when they are compared to theoretical models. Early models predicted a cylindrical wall-like puffed up inner rim with a shadowed region behind it (Dullemond et al. 2001). Subsequently, the introduction of a density-dependent evaporation temperature or multiple dust species yielded a rounded off rim structure (Isella & Natta 2005; Flock et al. 2016; Tannirkulam et al. 2007), that still could incorporate shadowing. However the temperature profile of this rounded off structure seems to strongly depend on the disk properties, especially the accretion rate (Jankovic et al. 2021; Chrenko et al. 2022). The temperature profile within the disk determines where MRI (magneto rotational instability) can occur, and the transition of turbulent regimes can lead to dust traps that facilitate planet formation (Ueda et al. 2019).

HD 144432 is a well studied system with multiple stars. It was initially categorized as a binary by Wackerling (1970) and further identified to be a Herbig Ae/Be star with a companion by Pérez et al. (2004). Carmona et al. (2007) found no disk for the companion, but one present for the central star HD 144432A. Later Müller et al. (2011) imaged the companion with enough resolution to determine it to be a binary itself, making HD 144432 a hierarchical triple system.

Therefore, HD 144332 is a young triple system with a planet-forming disk around its central object, which has recently been imaged with the VLTI (Very Large Telescope Interferometer), revealing an oversized half-light radius in the mid-infrared region. The observed SED (spectral energy distribution) and especially the visibility curves (Varga, J. et al. 2024) for distinct wavelengths of light are valuable constraints for the disk model used in this paper.

Previous mid-infrared-size surveys found the phenomenon of an enlarged mid-infrared region in disks to be common (Monnier et al. 2009; Menu et al. 2015). This is especially peculiar, since the correlation between the near-infrared size of the disks to their luminosities is strong, while the mid-infrared sizes are too large for the corresponding luminosity. It has been proposed that this deviation from the theoretical expectation can be explained through gaps in the disk caused by planets, or disk clearing by binary companions, or emission from remnant dust envelopes.

This paper will employ a radiative transfer code, based on previous work by Flock et al. (2013) and including accretion heating (Schobert et al. 2019) and dust diffusion (Schobert & Peeters 2021) to self consistently calculate temperature and density profiles, as well as the specially resolved dust-to-gas ratio, to produce SEDs and visibility curves matching the observations. By employing physical constraints through equilibrium states and steady-state accretion it is possible to narrow down properties of the disk, like the inner rim radius, the outer rim radius, the accretion rate and make statements on the composition of the dust. The physics based model, therefore, reduces the number of adjustable parameters and yields a consistent disk description.

This paper is structured as follows: Sect. 2 explains the model equations needed to describe the disk in terms of boundary conditions imposed by companion stars, as well as the method used to calculate the visibility curves. In Sect. 3 the numerical implementation, convergence criteria as well as processes to create simulated SEDs and visibility curves is outlined. Section 4 details the results and how specific properties of the system HD 144432 can be constrained using the observational data in conjunction with the simulations. Section 5 discusses the results as they pertain to the structure of protoplanetary disk in general and the effect of shadowing. The paper concludes in Sect. 6 with a summary of the results.

2. Model equations

The model equations used in this work for radiative transfer and hydrostatic equilibrium are those from (Schobert et al. 2019) with the additions from (Schobert & Peeters 2021). Given the characteristic parameters of a star, i.e. mass M_*, radius R_*, and surface temperature T_*, the model calculates the temperature and radiation energy density profiles of a 2D vertical slice of the disk. The simulation domain is bound by an inner and outer radius and an upper and lower polar angle. First the surface density is determined by the steady state accretion solution. From this the gas density is found through hydrostatic equilibrium. Third the radiative transfer equations are implicitly solved to determine temperature and radiation energy density in the disk. Finally the dust density is found in accordance with the temperature and the process is iterated until equilibrium. For brevity only the changes compared to (Schobert & Peeters 2021) are outlined in this section.

2.1. Stellar flux

The stellar flux is the main heat source of the disk, it is absorbed by the disk proportional to the local opacity. Rather than numerically calculating the divergence of the stellar flux $\mathbf{F}_*$, by taking the difference of flux through the surfaces of a finite volume, the divergence can be evaluated analytically, improving the precision. The temperature equation in (Schobert & Peeters 2021) was of the form:

$$\frac{c_\mathrm{v}\rho\Delta T}{\Delta t} = \rho\dot{Q}_\mathrm{cond} + \rho\dot{Q}_\mathrm{exchange} - \nabla\cdot\mathbf{F}_*, \tag{1}$$

where c_v is the specific heat capacity, ρ is the density, T the temperature, t the time, $\dot{Q}_\mathrm{cond}$ the heating rate through thermal conduction and $\dot{Q}_\mathrm{exchange}$ the heating rate through absorption of radiation within the disk combined with the cooling rate through emission by radiative cooling. By the definition of the stellar flux:

$$F_*(r) = \left(\frac{R_*}{r}\right)^2 \sigma_B T_*^4 e^{-\tau_*} \tag{2}$$

$$\tau_* = \int_{R_*}^{r} \sigma_*\, dr \tag{3}$$

$$\sigma_* = \rho_\mathrm{gas}\kappa_\mathrm{gas} + \rho_\mathrm{gas} f_\mathrm{d2g}\kappa_\mathrm{dust}(\nu_*)\,, \tag{4}$$

this can be evaluated in spherical coordinates and both sides normalized with respect to the density to yield:

$$\frac{c_\mathrm{v}\Delta T}{\Delta t} = \dot{Q}_\mathrm{cond} + \dot{Q}_\mathrm{exchange} + F_*[\kappa_\mathrm{gas} + f_\mathrm{d2g}\kappa_\mathrm{dust}(\nu_*)], \tag{5}$$

where f_d2g is the dust-to-gas ratio, κ_gas is the opacity of the gas and $\kappa_\mathrm{dust}(\nu_*)$ is the opacity of the dust at the characteristic frequency of the stellar light ν_*. This simplification, i.e. replacing equation (1) with equation (5), improves both runtime and precision of the code.

2.2. Companion stars

As will be shown in Sect. 3.1 the issue of boundary conditions needs to be treated with special care. Especially the boundary that is facing away from the central star is interesting, because it receives no direct stellar radiation as it is shadowed by the disk itself. Further it is the coldest part of the disk, acting as its heat sink. Using the same approach for the boundary as on the three other bounding surfaces is in this case possible, because the closest stars in the environment of the disk are known: the binary of HD144432B and HD14432C orbiting the central star. The projected distance between the central star and the binary is 1.47″ (Müller et al. 2011) at a distance of 154.1 pc (Bailer-Jones et al. 2021):

$$r_\mathrm{AB} = 154.1\,\mathrm{pc}\ \times 1.47'' = 226.5\,\mathrm{AU} \tag{6}$$

The presence of CO in the proto-planetary disk surrounding HD144432 was detected by Dent et al. (2005) up to a projected outer diameter of 0.6″, i.e. a radius of 46 AU using the same distance to earth as above. Additionally Monnier et al. (2017) found that beyond a projected radius of 0.3″ the maximum surface brightness of the disk stays below 20 mag arcsec^{-2}, one of the smallest far-IR excess from their sample. This suggests that the disk is truncated around 46 AU. Therefore, one can confidently assume the temperature at 100 AU from the central star towards the binary to be dominated by the optically thin approximation:

$$T^4_{\rm thin}(r = 100\,{\rm AU}) = \frac{1}{\varepsilon_{*,\rm B}} \left(\frac{R_{*,\rm B}}{2(r_{\rm AB} - 100\,{\rm AU})}\right)^2 T^4_{*,\rm B} + \tag{7}$$

$$\frac{1}{\varepsilon_{*,\rm C}} \left(\frac{R_{*,\rm C}}{2(r_{\rm AB} - 100\,{\rm AU})}\right)^2 T^4_{*,\rm C} \tag{8}$$

$$T_{\rm thin}(r = 100\,{\rm AU}) = 31.9\,{\rm K}, \tag{9}$$

where $\varepsilon_{*,\rm B} = 0.32$ and $\varepsilon_{*,\rm C} = 0.35$ are the ratios of the Planck mean opacity at the characteristic wavelength of the disk and the Planck mean opacity at the characteristic wavelength of the two companion stars. These opacities are calculated from the frequency dependent opacity given by Draine & Lee (1984). They were calculated for a typical sublimation temperature of the dust, $T_{\rm subl} = 1350\,{\rm K}$ similar to (Flock et al. 2016), and the effective temperatures of the companion stars, $T_{*,\rm B} = 4000\,{\rm K}$ and $T_{*,\rm C} = 3750\,{\rm K}$ (Müller et al. 2011). The stellar parameters of the binary as given by Müller et al. (2011) are for the radii $R_{*,\rm B} = R_{*,\rm C} = 1.5 \pm 0.7\,R_\odot$ and for the effective temperatures $T_{*,\rm B} = 4000 \pm 250\,{\rm K}$ and $T_{*,\rm C} = 3750 \pm 250\,{\rm K}$. These parameters lead to an estimate of 31.9 K for a distance of 100 AU from the central star towards the binary, which can be used as the boundary condition facing away from the central star. Because the disk is rotating and will receive less radiation from the other side, that is not facing HD 144432 B and C, 31.9 K can be seen as an upper bound on the boundary condition. Section 3.1 provides simulations that proof a convergence of the temperature profile for the disk beyond 8 AU if the boundary condition at 100 AU is chosen to be 40 K or lower.

2.3. Surface denstiy

The surface density Σ is calculated assuming a steady state thin disk approximation (Clarke & Carswell 2009):

$$\Sigma = \frac{\dot{M}}{3\pi\nu_{\rm t}} \left[1 - \left(\frac{R_{\rm max}}{r}\right)^{0.5}\right], \tag{10}$$

where $\dot{M}$ is the accretion rate, $\nu_{\rm t}$ is the turbulent viscosity and $R_{\rm max}$ is the point at which the angular velocity has its maximum. This is somewhere close to the star but not closer than its magnetic truncation radius. In Schobert et al. (2019) the second term in the square brackets was neglected, because the simulation domain was sufficiently far removed from the star. This work requires boxes closer to the star and the correction term could no longer be neglected, therefore $R_{\rm max} = 5R_*$ was chosen (Calvet & Gullbring 1998), a point that lies around the magnetic truncation radius of the star. This will prevent the surface density from becoming unphysically high close to the star.

2.4. IR interferometric measurements

The visibilty data used in this work has been observed by VLTI/MATISSE (Varga, J. et al. 2024). The measurements have been shifted with regard to the inclination so that minor and major axis would be identical and the disk would appear circular.

The visibility can be calculated from the mutual coherence function:

$$\Gamma_{12}(u, v) = \int\int_{\rm source} I(l, m) \exp(-2\pi i(ul - vm))\,{\rm d}l\,{\rm d}m, \tag{11}$$

that is defined as the Fourier transform of the intensity by the van Cittert–Zernike theorem (van Cittert 1934; Zernike 1938). The complex visibility $\mu(u, v)$ is the normalization of the coherence function:

$$\mu(u, v) = \frac{\Gamma_{12}(u, v)}{\Gamma_{12}(0, 0)} \tag{12}$$

But the complex visibility cannot be measured for near- and mid-infrared, only the absolute value and under the assumption of cylindrical symmetry it is convenient to use the radial distance in phase space, or baseline, $B = \sqrt{u^2 + v^2}$:

$$V(B) = \left\|\mu(\sqrt{u^2 + v^2})\right\| \tag{13}$$

The baseline is basically the distance of the two measuring telescopes. The numerical process to obtain the intensity maps and calculate the visibility curve is outlined in Sect. 3.2.

Table 1. General model setup parameters, which are from top to bottom the radial and polar number of grid cells, inner and outer box radius, the upper and lower polar box angle, stellar surface temperature, radius and mass in solar equivalent and the mass density ratio of dust and gas in the disk.

Parameter	Value
$N_r \times N_\theta$	3840×257
$[r_{\rm min},\ r_{\rm max}]$	$[0.052\,{\rm AU},\ 8\,{\rm AU}]$
$[\theta_{\rm min},\ \theta_{\rm max}]$	$[\pi/2 - 0.36,\ \pi/2 + 0.36]$
Stellar parameter	$T_* = 7\,750\,{\rm K}$, $R_* = 2.23 R_\odot$, $M_* = 1.82 M_\odot$
Dust-to-gas ratio	$f_0 = 0.01$

3. Numerical implementation

This section describes the creation of synthetic images and SEDs from the simulations and the calculation of the visibility curve as well as a study of the influence of the outer rim boundary condition on the temperature profile of the disk. The model parameters used are listed in table 1. The surface density is calculated using a steady state assumption for different accretion rates that are stated for each individual case.

3.1. Convergence with the outer rim boundary condition

In this section, the convergence of the simulations with respect to the outer boundary condition is investigated. The simulation implicitly solves a system of equations for the temperature and the radiation energy density, which are coupled through emission and absorption (Schobert et al. 2019). The boundary condition for the temperature is zero gradient and for the radiation energy density $E_{\rm R}$ fixed boundary conditions are employed. On the outer edge of the simulation box, the side facing away from the star, a single value is assumed for the radiation energy density, which for ease of understanding is converted to a temperature in the following text with $T = a_{\rm R}^{-0.25} E_{\rm R}^{0.25}$, where $a_{\rm R}$ is the radiation constant.

As can be seen in Fig. 1 boundary temperatures below 40 K align very well for even for large radii, the discrepancy between 40 K and 10 K is less than 1 K at 40 AU distance. However, for a radiation energy density at the boundary, that corresponds to 70 K, which would be the case if HD 144432 had a companion star of about equal surface temperature, the temperature profile is affected by more than 10 K discrepancy for radii up to 10

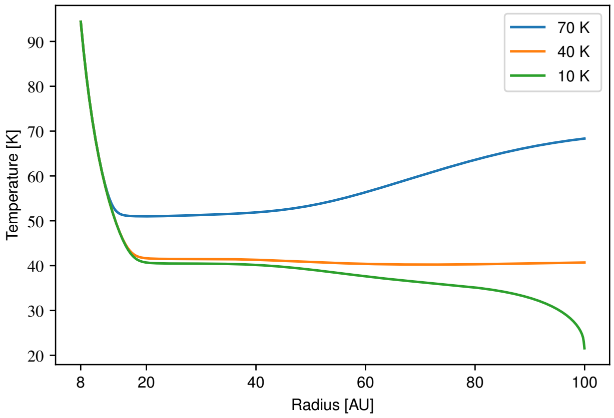

Fig. 1. Midplane temperature profile from 8 to 100 AU for three different outer boundary conditions, specifically radiation energy densities equivalent to 70 K (blue line), 40 K (orange line) and 10 K (green line).

AU towards the central star. A Temperature of this magnitude is excluded with respect to the calculations presented in Sect. 2.2, which means the results shown in the following are robust towards the specific choice of outer boundary condition.

3.2. SED and visibility

In order to produce visibility curves of an object an intensity map is necessary. This can be produced using the ray-tracing code RADMC3D (Dullemond et al. 2012). Images were produced for $3\,\mu$m and $9\,\mu$m wavelength, respectively, using 0° inclination. The observational data from Varga, J. et al. (2024) compensates the baselines towards the major axis. Therefore, artificially introducing an inclination in the synthetic image, only to compensate for it in the calculation of the visibility curve, would be futile. The temperature profile and dust density profile were produced with the code described in Sect. 2. RADMC3D was used only for the intensity map since the effect of accretion heating is not included in its code. The synthetic intensity map is then Fourier-transformed using an explicit Fourier-series and normalized to the total intensity according to eqs. (12) and (13).

The SED also includes the light coming from the central star, HD 144432A, which is modeled as a black body with surface temperature 7750 K, stellar mass $M_* = 1.82\,M_\odot$ and stellar radius $R_* = 2.23\,R_\odot$ (Guzmán-Díaz et al. 2021). The frequency dependent opacity of the dust is taken from (Draine & Lee 1984).

The synthetic image in the top of Fig. 2 shows, what the disk around HD 144432A looks like at $3\,\mu$m wavelength. For illustrative purposes these two images do include an 48° inclination (Dent et al. 2005). In order to clearer show more of the structure of the disk the maximum surface brightness has been capped in both images in Fig. 2. The radiation is localized to a small ring around the inner edge of the dust disk, most of the radiation comes from the annulus between 0.31 AU and 0.34 AU, like the analytic approximation in Sect. A suggests. The lower image is the same view for 9μm wavelength. In this regime the radiation is more spread out and a significant portion can still be observed around 1.25 AU. The apparent vertical asymmetry is due to the inclination. The flaring disk shows more of its hot surface to the observer above the star than below. The star itself is suppressed in these images, again to make the structure visible, for the calculation of the visibility however the star is included.

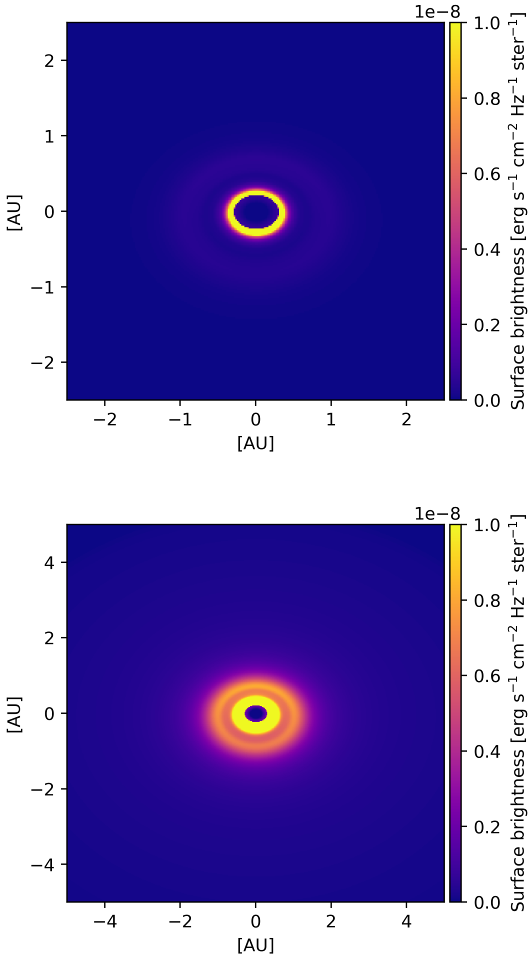

Fig. 2. Synthetic images of the disk, viewed at 48° inclination (Dent et al. 2005) from face-on at $3\ \mu$m (*top*) and $9\ \mu$m (*bottom*) wavelength. The surface brightness is capped at 10^{-8} erg s^{-1}cm^{-2}Hz^{-1}ster^{-1} to better see the structure. The inclination is for illustrative purpose.

4. Results

This section presents the best set of parameters to model the observational data of HD 144432 as well as a general connection between the $3\,\mu$m visibility curve and the inner rim radius $r_{\rm in}$ where the dust begins to form and the disk becomes optically thick radially outwards from the star. Further the connection between the amount of accretion heating and and its influence on the visibility curve at $9\,\mu$m are discussed and finally different dust compositions and their SEDs are shown.

4.1. Best set of model parameters for HD 144432

The leading idea of this work is to present a simple physically coherent model of an accretion disk that reproduces the observational data for HD 144432 to the models best ability. This means the simulation has only a small amount of free parameters, so that these are well constrained by the data. These three parameters are: the accretion rate $\dot{M}$, the viscosity parameter α and the ratio of the mean Planck opacities for the characteristic wavelength of the star and the dust sublimation front ε. As shown in the following Sects. the $3\ \mu$m visibility curve is strongly connected to the inner radius of the sublimation front of the disk, which itself is function of all three parameters. Thus one degree

Table 2. Best set of model parameters for HD 144432. Accretion rate in $M_{\odot}\mathrm{yr}^{-1}$, viscosity α and ratio of mean Planck opacities ε.

Parameter	Value
$\dot{M}$ in $M_{\odot}\mathrm{yr}^{-1}$	$1.6 \cdot 10^{-8}$
α	$4.0 \cdot 10^{-2}$
ε	0.11

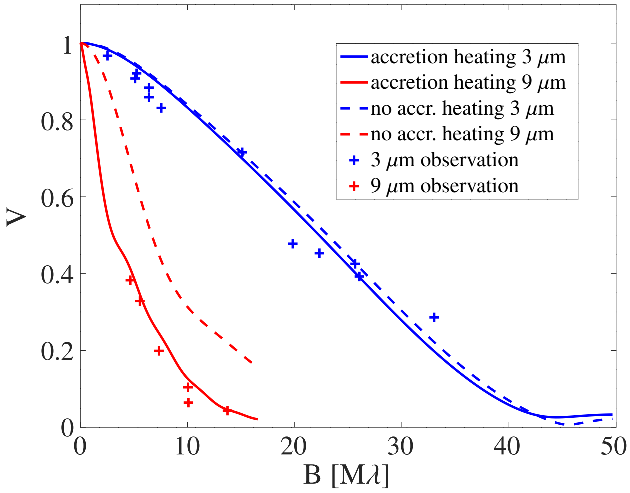

Fig. 3. Visibilities as measured by Varga, J. et al. (2024) for 3 μm (blue crosses) and 9 μm (red crosses) and simulated visibilities for 3 μm (blue lines) and 9 μm (red lines) using the parameters from Table 2. The solid lines show the model including accretion heating and the dashed lines show the same model without accretion heating.

of freedom is removed. Secondly the 9 μm line sets the amount of accretion heating which is connected to α, therefore removing a second degree of freedom. Lastly the SED and especially the shape of the silicate feature informs the dust composition, or at least the ratio of mean Planck absorption and emission efficiencies, determining the final fit parameter.

The final values used for the run presented in figs. 3, 8 and 9 are listed in table 2. The accretion rate lies within the range provided in (Donehew & Brittain 2011), which is $(1.8 \pm 0.4) \cdot 10^{-8} M_{\odot}\mathrm{yr}^{-1}$. The α-viscosity $\alpha = 4.0 \cdot 10^{-2}$ lies within numerical predictions for MRI α values, which can range from 0.01 to 0.1 (Flock et al. 2017) depending on the magnetic field configuration. Finally the ε value is within the range of the four opacity models investigated and corresponds to the dust composition presented in Draine & Lee (1984).

This best fit can be seen in Fig. 3. The figure shows how the observational data compares to the simulated intensity found through RADMC3D as described in Sect. 3.2. The 3 μm curve and especially the 9 μm curve fit the data well. The solid lines show the model including accretion heating, whereas the dashed lines represent the same model without the effect. The conclusions that can be drawn from the shape of the 9 μm curve are outlined in Sect. 4.3 and the implications of the 3 μm curve are explained in the following Sect.

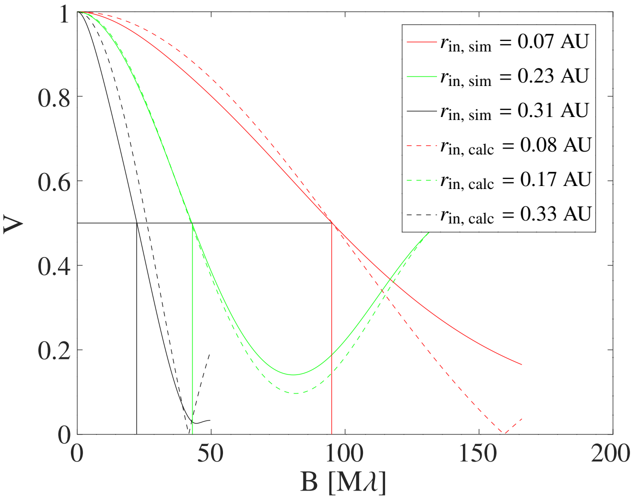

Fig. 4. 3 μm visibilities for different inner rim simulations (solid lines) and corresponding analytic visibilities calculated with eq. (A.2) (dashed lines) using $C_* = 0.2$ (red dashed line), $C_* = 0.55$ (green dashed line) and $C_* = 0.05$ (black dashed line). $B_{0.5,3\mu\mathrm{m}}$ is measured as 95, 43 and 23 $M\lambda$ respectively. The corresponding inner rim radii are listed in Table 3.

4.2. 3 μm visibility curve and inner rim position

The visibility at short baselines can be used as a measure for the disk radius (Dullemond & Monnier 2010). Evaluation of simulations with different inner rim positions shows a strong connection between the inner rim position r_{in} and the half-width baseline $B_{0.5,3\mu\mathrm{m}}$ of the 3 μm visibility curve. The inner rim position r_{in} is determined as the point where the vertical optical depth reaches unity integrated from the midplane upwards at the opacity of 3 μm wavelength. This correlation can be used in conjunction with the analytic model proposed in the Appendix to suggest a simple equation for the inner rim position:

$$r_{\mathrm{in}}[AU] = 0.9 \frac{1.65}{2\pi} \frac{d[AU]}{10^6\, B_{0.5,3\mu\mathrm{m}}[M\lambda]} \tag{14}$$

$$= 0.236 \frac{d[AU]}{10^6\, B_{0.5,3\mu\mathrm{m}}[M\lambda]}, \tag{15}$$

where $d[AU]$ is the distance of the system to earth in astronomical units and $B_{0.5,3\mu\mathrm{m}}[M\lambda]$ is the half-width of the 3 μm visibility curve in units of one million wavelengths.

To test eq. (15) and compare it to simulations, three exemplary cases with different surface densities and, therefore, different inner rim radii, were evaluated. The approximation holds true over a wide range of inner radii, as can be seen in Fig. 4 and table 3. Simulations with an inner rim radius from 0.07 AU to 0.31 AU, which is the value predicted for HD 144432 in this work, were tested. The simple analytic approximation derived from a ring model can be used to make a meaningful prediction about the inner rim position of such disks. The only assumption that this approximation needs is that most of the irradiation of the disk at 3 μm is emitted from an annulus, that has a ratio of radii $r_{\mathrm{in}}/r_{\mathrm{out}} = 0.9$. This value has been derived from the simulation that best agrees with the data from (Varga, J. et al. 2024) for HD 144432.

Table 3. Simulated and analytic inner radii for cases with different surface densities and, therefore, different inner rim radii, for validation of the analytic relation eq. (15).

#	$r_{\text{in, sim}}$	$r_{\text{in, calc}}$
1	0.067 AU	0.079 AU
2	0.226 AU	0.174 AU
3	0.314 AU	0.326 AU

4.3. Accretion heating and 9 μm visibility curve

Similar to the influence of the inner rim position on the 3 μm visibility profile, the amount of accretion heat through viscous dissipation Q_{heat} affects the outer rim position, especially for the 9 μm curve. More viscous dissipation means that the area behind the inner rim has a lower temperature gradient, than a less viscous disk. This effect was already studied in Schobert et al. (2019) (see Sect. 4.2 and Fig. 4 therein). The accretion heat is included in the calculation of the internal energy of the disk:

$$\partial_t \rho u = -\sigma c(a_{\text{R}} T^4 - E_R) - \nabla \cdot \mathbf{F}_* + Q_{\text{heat}} \tag{16}$$

$$Q_{\text{heat}} = \rho \nu_t \, [r \, \partial_r \, \Omega]^2 \,, \tag{17}$$

where ρ is the density of the gas, u is the internal energy density, σ is the mean opacity, a_{R} is the radiation constant, $\mathbf{F}_*$ is the stellar flux, ν_{t} is the turbulent viscosity and Ω the angular rotation frequency. It is therefore possible to estimate the turbulent viscosity of the disk through the shape of the 9 μm visibility curve. Fig. 5 shows the visibility profiles for four different cases with varying α parameters. These cases use surface density profiles that ensure the same inner rim radius, which is already constrained from the 3 μm visibility curve, but they differ in the amount of accretion heat they experience. This keeps their temperature high to larger radii. Keeping the analytic ring model in mind it is possible to predict how this should influence the visibility curve. If the outer radius, meaning the radius where the brightness drops below a relevant threshold, increases, while the inner radius stays the same, then their ratio ϵ shrinks. Lowering ϵ makes the visibility curve decrease slower, but increasing r_{out} leads to a steeper decent, and this effect wins out analytically as well as in the simulations. Bigger α values lead to a better agreement with the observational data. This means the region behind the inner rim of the disk must have a sufficient high viscosity and, consequently, be significantly heated, to produce the necessary amount of 9 μm radiation, that is measured. The simulations show improved agreement with the measured data up to an $\alpha = 4 \cdot 10^{-2}$ after which the improvement saturates. Therefore this value was chosen in the final simulation of HD 144432.

The code used for the simulations in this paper is able to incorporate temperature dependent viscosity. So the α parameter, using the α prescription for turbulent viscosities (Shakura & Sunyaev 1973), can change at a temperature where MRI is no longer possible. The simulations have shown, that the α parameter for the MRI inactive regions further out can not be determined from the 9 μm profile, since these regions are too cold the meaningfully contribute to the 9 μm radiation. Therefore, only a single α parameter is chosen and determined, which is set constant in the simulation box.

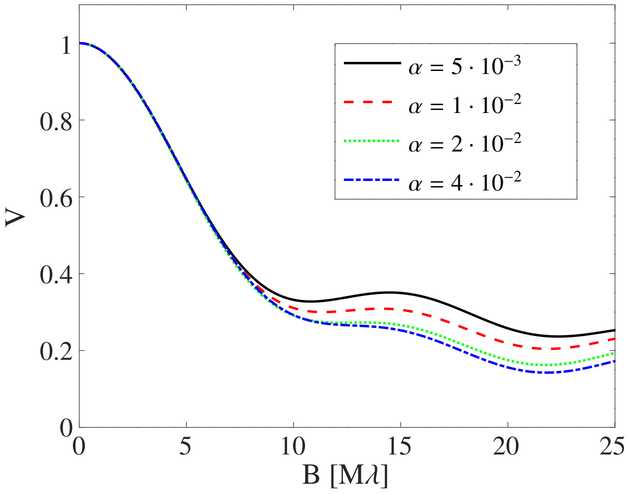

Fig. 5. Visibility curves for 9 μm for different viscosities.

Table 4. Mean Planck opacities for different data sets at 7750 K and 1350 K and their absorption to emission ratio ε.

κ_ν data set	$\kappa_{\text{dust, star}}$ $\left[\frac{\text{cm}^2}{\text{g}}\right]$	$\kappa_{\text{dust, rim}}$ $\left[\frac{\text{cm}^2}{\text{g}}\right]$	ε
Preibisch et al. 1993	12258.74	644.34	0.053
Draine & Lee 1984	3817.20	420.40	0.11
Varga et al. 2024	7714.29	1484.22	0.19
Henning et al. 1999	11435.47	317.73	0.028

4.4. Dust composition and the SED silicate feature

The dust composition influences the simulations in two major ways: first the ratio of the mean Planck opacities for the characteristic wavelength of the star and the dust sublimation front ε effects the inner rim position. But the inner rim position is already determined by the 3 μm curve and the viscosity is already determined by the 9 μm visibility curve, so the possible value for ε is within a tight range. Second the shape of the wavelength dependent opacity will influence the shape of the SED. So especially the shape of the silicate feature around 10 μm, that is present in HD144432 observations, needs to be modeled correctly by the dust composition.

This work looks at four previously published dust compositions and their corresponding opacity curves: A model by Preibisch et al. (1993) with amorphous carbon and ice-coated silicate grains, a model by Draine & Lee (1984) with graphite and silicate particles with sizes in the range of 0.003-1 μm, a composition from Varga, J. et al. (2024) for the middle zone of the disk with grain sizes of 0.1, 2.0 and 5 μm of several species and finally a curve produced from data from Henning et al. (1999) with 0.1 μm grains made of olivine. All the opacity curves can be seen in Fig. 6. They are generally similar but differ in how pronounced the jump at the 10 μm point is.

Like mentioned above the first way the opacity influences the disk is through the ratio of absorption to emission efficiency. These values are listed in table 4. Analytically one can determine the inner rim position using equations (5) and (6) from (Ueda

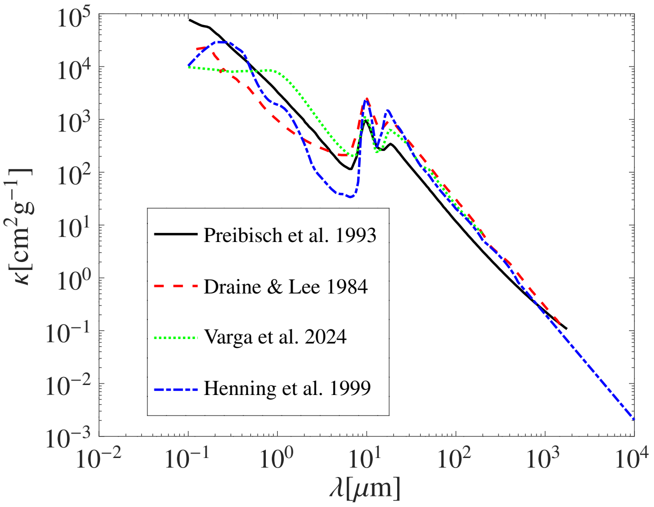

Fig. 6. A selection of wavelength dependent opacities from different works: Preibisch et al. (1993) (black solid line), Draine & Lee (1984) (red dashed line), correspondence with Varga, J. et al. (2024) κ for the middle zone of the disk (green dotted line), compiled from database from Henning et al. (1999) (blue dashed and dotted line).

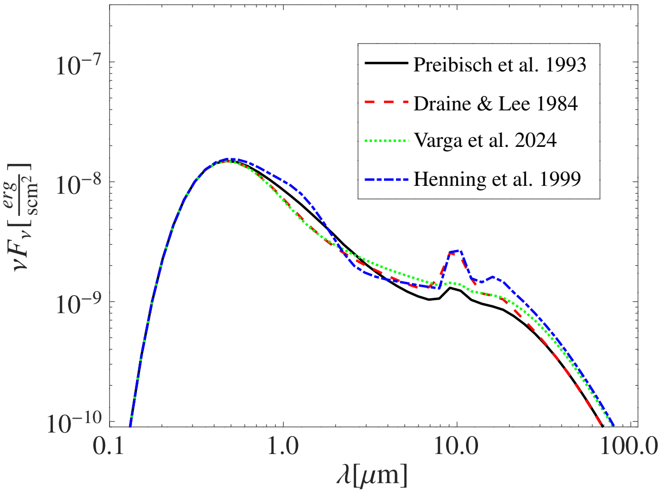

Fig. 7. A selection of SEDs computed from the opacities from Fig. 6: Preibisch et al. (1993) (black solid line), Draine & Lee (1984) (red dashed line), correspondence with Varga, J. et al. (2024) κ for the middle zone of the disk (green dotted line), compiled from database from Henning et al. (1999) (blue dashed and dotted line).

et al. 2017):

$$R_{\mathrm{AB}} = \frac{1}{2}\left(\frac{T_*}{T_{\mathrm{ev}}}\right)^2 R_* \tag{18}$$

$$R_{\mathrm{BC}} = \frac{1}{2}\left(\frac{1}{\varepsilon}\right)^{0.5}\left(\frac{T_*}{T_{\mathrm{ev}}}\right)^2 R_* \,, \tag{19}$$

with $T_{\mathrm{ev}} = 1470$ K and $\varepsilon = 0.11$. These boundaries for the inner rim position compute to $R_{\mathrm{AB}} = 0.14$ AU, which is the boundary between the dust free region and the dust halo, and $R_{\mathrm{BC}} = 0.51$ AU, which is the boundary between the dust halo and the condensation front. The value that was determined in Sect. 4.2, which is 0.31 AU lies between these two values as expected, because the dust gradually forms between these two boundaries and the optically thick transition happens closer to the end of the range. Because of this analytical compatibility, and also because of the fit of the SED as described in the following the opacity curve of Draine & Lee (1984) was chosen for the final simulation for HD 144432.

The second way the observables are influenced by the opacity curves is visible in the SED, especially around the silicate feature. The simulated SEDs for all for dust compositions are shown in Fig. 7. Only two of the four opacity curves display a prominent silicate feature, namely the opacity model from Draine & Lee (1984) and Henning et al. (1999), but again the opacity model from Draine & Lee (1984) is the best fit, because it has lower intensity at longer wavelengths than 10 μm and better reproduces the data of Varga, J. et al. (2024) in the rage of 1 to 5 μm. The prominence of the silicate peak at 10 μm is influenced by the value of the opacity at 10 μm. Draine & Lee (1984) and Henning et al. (1999) have opacity values at 10 μm, that are about twice those from Varga, J. et al. (2024) and Preibisch et al. (1993), thus the corresponding SED values at 10 μm are also about double.

For both reasons outlined above the opacity curve chosen to simulate HD 144432 is the one provided by Draine & Lee (1984). The final SED for the best set of parameters can be seen in Fig. 8. It reproduces the photometry data for the star below 1 μm very well and even aligns at 100 μm. The peak of the silicate feature is captured but the flanks do not fall of as steeply as observed.

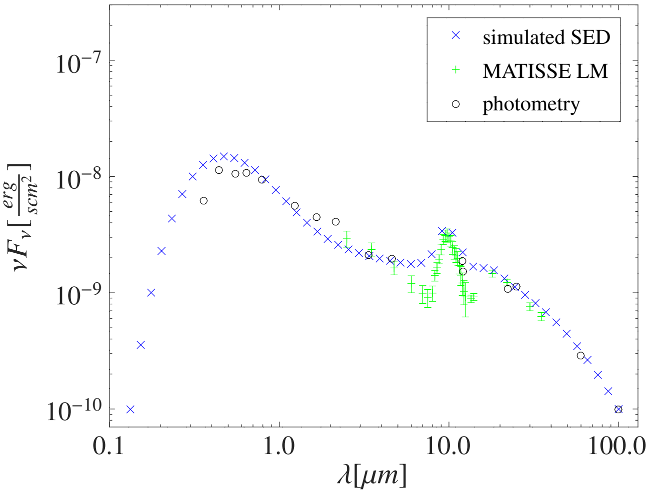

Fig. 8. SED for HD 144432 as measured by MATISSE in the LM-band (green crosses with vertical error bars) (Varga, J. et al. 2024), photometric data (black circles) and simulated SED from this work (blue crosses).

5. Discussion

This section discusses the properties of the disk found to be the best model for the observational data of HD 144432 and what can be derived for the inner structure of the disk.

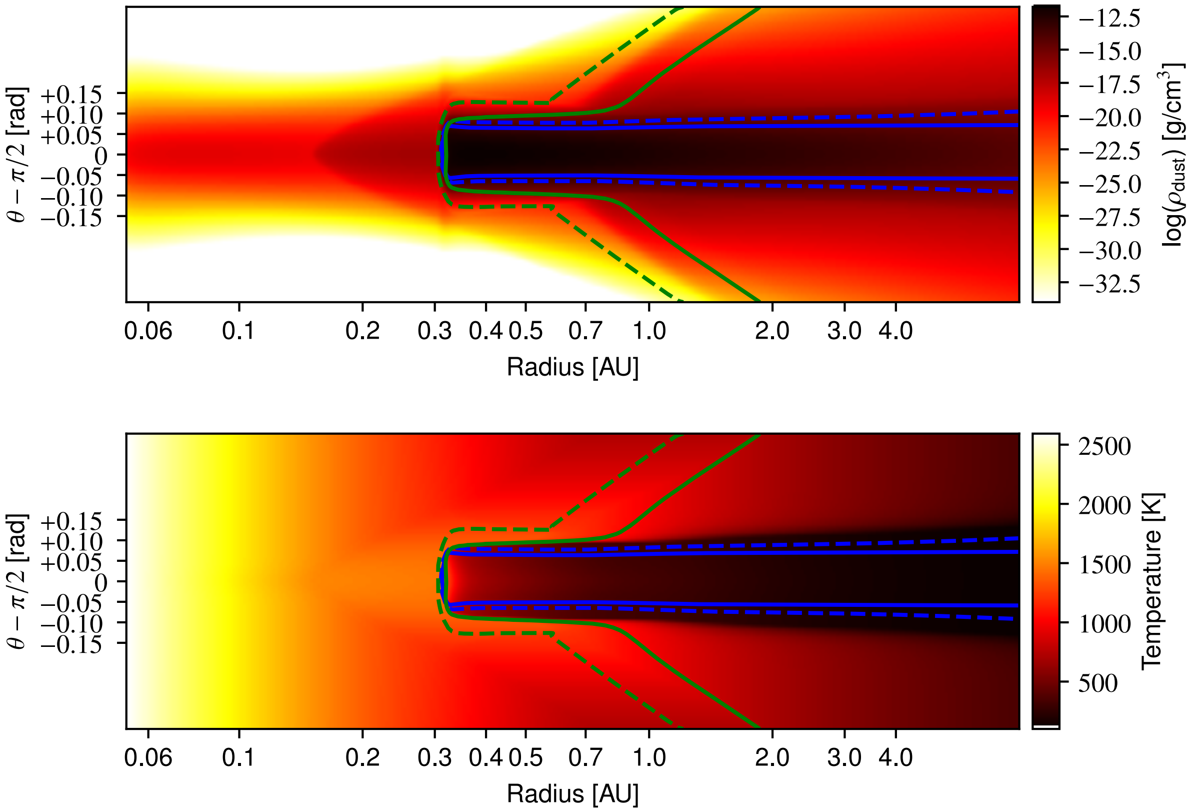

Fig. 9. Logarithm to the base 10 of the dust density (*top*) and temperature (*bottom*), the y-axis it the angle measured from the midplane, the x-axis is the distance to the central star in logarithmic scaling. The blue line depicts the optical depth of unity for 9 μm (dashed line) and 3 μm (solid line). The green lines show the dust evaporation temperature (solid line) and a dust-to-gas ratio of $5 \cdot 10^{-7}$ (dashed line).

5.1. Structure of the disk

Fig. 9 depicts the logarithm of the dust density as well as different dust formation thresholds. The y-axis shows the angle toward the midplane and the x-axis is the logarithmic distance to the central star. The area that emits the 3 μm radiation can be seen in the lower image starting behind the blue lines at the inner rim of the disk, where there is a small lens shaped area in bright red, that is hot enough to be significant. The temperature then continues to fall as the distance to the star increases but with a lower gradient.

The results gained from evaluating the visibility curves allow for an analysis of the structure of the disk. The inner rim becomes optically thick for 3 and 9 μm radiation at 0.31 AU and the temperature falls rapidly beyond that. Radiation in the 3 μm band is not emitted in a significant amount beyond 0.34 AU and the 9 μm radiation falls below the threshold around 1.25 AU. The 9 μm area is in fact located in a similar area to a zone 1 in (Varga, J. et al. 2024), where they find that their zone 2 starts at 1.3 AU, or more precisely the gap dividing zone 1 and 2 ends at 1.26 AU. In Fig. 2 (*bottom*) a second ring starting around 1 AU is visible, this is connected to the flaring of the dust-to-gas ratio as can be seen in Fig. 9.

5.2. Puffed-up rim and shadowing

A puffed up inner rim with a shadowed region behind has been part of previous theoretical models (Dullemond et al. 2001). The model presented in this work shows multiple brightness rings in Fig. 2, specifically for 9 μm. Comparing to Fig. 9 we find that position of the rings aligns with a puffed up region of dust density. The model presented in this work uses a formula for the dust to gas ratio that adapted from Flock et al. (2016), has been simplified in Schobert & Peeters (2021) and now additionally simplified by dropping the optical depth dependency:

$$f_{\mathrm{d2g}} = \frac{f_0}{2}\left\{1 - \tanh\left[\left(\frac{T - T_{\mathrm{ev}}}{\Delta T_{\mathrm{dust}}}\right)^3\right]\right\}, \tag{20}$$

with the dust evaporation temperature T_{ev}, evaporation temperature range $\Delta T_{\mathrm{dust}} = 100\,\mathrm{K}$ and the reference dust-to-gas ratio $f_0 = 10^{-2}$. For the dust evaporation temperature the fitting model proposed by Isella & Natta (2005)

$$T_{\mathrm{ev}} = 2000\,\mathrm{K}\left(\frac{\rho}{1\,\mathrm{g\,cm^{-3}}}\right)^{0.0195} \tag{21}$$

was used.

Using Eq. (20) one can understand the green lines in Fig. 9. The solid one is the equilibrium point $f_{\mathrm{d2g}} = \frac{f_0}{2}$ or $T = T_{\mathrm{ev}}$. It corresponds to an almost conical rim with a wall-like inner surface and also shows a small puffed-up rim, leading to a shadowed region between ~ 0.35 AU and ~ 0.9 AU. This is even better visible in the dashed line, where $f_{\mathrm{d2g}} = 5 \cdot 10^{-7}$ or $T \approx T_{\mathrm{ev}} + 170\,\mathrm{K}$; it does show a higher polar angle at the rim and drops to lower angles behind, before the disk begins to flare, at ca. 0.6 AU. This dust density profile translates to the two brightness rings seen in Fig. 2, meaning a shadowed disk. At even lower dust thresholds the characteristic rounded of rim, that is connected to a density dependent evaporation temperature can be seen.

6. Summary

This paper presents the best set of model parameters to align with data measured for HD 144432 and explains how the observational data can be interpreted prima face with a simple analytical model as well as in depth with a numerical 2D model for protoplanetary disks that self-consistently includes radiative transfer and dust sublimation. The model builds upon earlier work (Flock et al. 2016; Schobert et al. 2019; Schobert & Peeters 2021) and measurement data (Varga et al. 2018; Varga, J. et al. 2024) to produce the following results:

1. The 3 μm visibility curve is strongly connected to the inner rim position. There is an easy analytical equation connecting the half-width of the visibility to the inner rim position.
2. The 9 μm visibility curve is indicative of the amount of accretion heating within the disk, HD 144432 has a high turbulent viscosity, with $\alpha = 0.04$ and an accretion rate of $\dot{M} = 1.6 \cdot 10^{-8} M_{\odot} \mathrm{yr}^{-1}$.
3. The SED is best reproduced with graphite and silicate particles with sizes in the range of 0.003-1 μm and an absorption to emission ratio of $\varepsilon = 0.11$.

The code used to produce these results can be found at bitbucket.org/astro_bayreuth/rmhdcode.

Acknowledgements. MATISSE was designed, funded and built in close collaboration with ESO, by a consortium composed of institutes in France (J.-L. Lagrange Laboratory - INSU-CNRS - Côte d'Azur Observatory - University of Côte d'Azur), Germany (MPIA, MPIfR and University of Kiel), The Netherlands (NOVA and University of Leiden), and Austria (University of Vienna). The Konkoly Observatory and Cologne University have also provided some support in the manufacture of the instrument. J. Varga is funded from the Hungarian NKFIH OTKA project no. K-132406. J. Varga has received funding from the European Research Council (ERC) under the European Union's Horizon 2020 research and innovation programme under grant agreement No 716155 (SACCRED). The research of J. Varga is supported by NOVA, the Netherlands Research School for Astronomy. J. Varga acknowledges support from the Fizeau exchange visitors program. The research leading to these results has received funding from the European Union's Horizon 2020 research and innovation programme under Grant Agreement 101004719 (ORP).

References

Bailer-Jones, C. A. L., Rybizki, J., Fouesneau, M., Demleitner, M., & Andrae, R. 2021, The Astronomical Journal, 161, 147
Calvet, N. & Gullbring, E. 1998, The Astrophysical Journal, 509, 802
Carmona, A., van den Ancker, M. E., & Henning, T. 2007, A&A, 464, 687
Chrenko, O., Chametla, R. O., Nesvorný, D., & Flock, M. 2022, A&A, 666, A63
Clarke, C. J. & Carswell, R. F. 2009, Principles of Astrophysical Fluid Dynamics (Cambridge University Press)
Dent, W. R. F., Greaves, J. S., & Coulson, I. M. 2005, MNRAS, 359, 663
Donehew, B. & Brittain, S. 2011, The Astronomical Journal, 141, 46
Draine, B. T. & Lee, H. M. 1984, ApJ, 285, 89
Dullemond, C. & Monnier, J. 2010, Annual Review of Astronomy and Astrophysics, 48, 205
Dullemond, C. P., Dominik, C., & Natta, A. 2001, ApJ, 560, 957
Dullemond, C. P., Juhasz, A., Pohl, A., et al. 2012, RADMC-3D: A multi-purpose radiative transfer tool
Flock, M., Fromang, S., González, M., & Commerçon, B. 2013, A & A, 560, A43
Flock, M., Fromang, S., Turner, N. J., & Benisty, M. 2016, ApJ, 827, 144
Flock, M., Fromang, S., Turner, N. J., & Benisty, M. 2017, The Astrophysical Journal, 835, 230
Guzmán-Díaz, J., Mendigutía, I., Montesinos, B., et al. 2021, A&A, 650, A182
Henning, T., Il'in, V. B., Krivova, N. A., Michel, B., & Voshchinnikov, N. V. 1999, Astron. Astrophys. Suppl. Ser., 136, 405
Isella, A. & Natta, A. 2005, A & A, 438, 899
Jankovic, M. R., Owen, J. E., Mohanty, S., & Tan, J. C. 2021, Monthly Notices of the Royal Astronomical Society, 504, 280
Mahajan, V. N. 1986, J. Opt. Soc. Am. A, 3, 470
Menu, J., van Boekel, R., Henning, T., et al. 2015, A&A, 581, A107
Monnier, J. D., Harries, T. J., Aarnio, A., et al. 2017, The Astrophysical Journal, 838, 20
Monnier, J. D., Tuthill, P. G., Ireland, M., et al. 2009, ApJ, 700, 491
Müller, A., Carmona, A., van den Ancker, M. E., et al. 2011, A&A, 535, L3
Pérez, M. R., van den Ancker, M. E., de Winter, D., & Bopp, B. W. 2004, A&A, 416, 647
Preibisch, T., Ossenkopf, V., Yorke, H. W., & Henning, T. 1993, A&A, 279, 577
Rivolta, C. 1986, Appl. Opt., 25, 2404
Schobert, B. N. & Peeters, A. G. 2021, A&A, 651, A27
Schobert, B. N., Peeters, A. G., & Rath, F. 2019, ApJ, 881, 56
Shakura, N. I. & Sunyaev, R. A. 1973, A & A, 24, 337
Tannirkulam, A., Harries, T. J., & Monnier, J. D. 2007, ApJ, 661, 374
Ueda, T., Flock, M., & Okuzumi, S. 2019, The Astrophysical Journal, 871, 10
Ueda, T., Okuzumi, S., & Flock, M. 2017, ApJ, 843, 49
van Cittert, P. 1934, Physica, 1, 201
Varga, J., Ábrahám, P., Chen, L., et al. 2018, A&A, 617, A83
Varga, J., Waters, L. B. F. M., Hogerheijde, M., et al. 2024, A&A, 681, A47
Wackerling, L. R. 1970, Mem. RAS, 73, 153
Zernike, F. 1938, Physica, 5, 785

Appendix A: Analytic ring model

The disk, as it is seen by telescopes, can be approximated as a bright ring. The central star is perceived as a point source by the telescopes, so it only adds a constant to the Fourier transform. Going outward from the star the disk begins to radiate at the sublimation front, which forms the inner boundary $r_{\rm in}$ of the visible annulus. Then further from the star, the temperature decreases and with it the amount of radiation emitted by the disk. At a certain outer radius $r_{\rm out}$ it falls below a point where it contributes a meaningful part to the ring.

The Fourier transform of such a ring is well known as the obscured Airy pattern (Rivolta 1986; Mahajan 1986) and its formula is:

$$V(B) = \frac{1}{1-\epsilon^2}\left|\frac{2J_1(x)}{x} - \frac{2\epsilon J_1(\epsilon x)}{x}\right|, \tag{A.1}$$

where $x = \frac{2\pi r_{\rm out}}{d}\frac{B}{\lambda}$, with baseline B, wavelength λ and distance between observer and star system d, $\epsilon = \frac{r_{\rm in}}{r_{\rm out}}$ is the annular aperture obscuration ratio and J_1 is the Bessel function of the first kind of order one.

Adding the constant contribution of the central star C_* the formula becomes

$$V(B) = \frac{1}{1+C_*}\left|\frac{1}{1-\epsilon^2}\left(\frac{2J_1(x)}{x} - \frac{2\epsilon J_1(\epsilon x)}{x}\right) + C_*\right|. \tag{A.2}$$

So the visibility curve can be understood as a combination of two Bessel functions and a constant offset for the star.

Using the point from the simulation, where the visibility first falls below 0.5 as shown in Fig. 4, $x_{0.5,\epsilon}$ can be determined for any ratio ϵ. Knowing the inner rim radius is 0.31 AU, as seen in Fig. 9, it is possible to calculate the outer radii using an iterative procedure, where ϵ and $r_{\rm out}$ are determined simultaneously. After ϵ is set, $x_{0.5,\epsilon}$ can be found numerically and the following simple equation for the inner rim becomes available:

$$r_{\rm in}[AU] = \epsilon\frac{x_{0.5,\epsilon}}{2\pi}\frac{d[AU]}{10^6\, B[M\lambda]} \tag{A.3}$$

The self-consistent values, found for the case presented in this paper, are $x_{0.5}(\epsilon = 0.9) = 1.65$ and $r_{\rm out} = 0.34$ AU for the 3 μm curve, and $x_{0.5}(\epsilon = 0.25) = 2.20$ and $r_{\rm out} = 1.25$ AU for the 9 μm curve. For these pairs the product of both ϵ and $r_{\rm out}$ calculates to an inner rim radius of 0.31 AU, as found in the simulation. This analytic model can be seen in Fig. A.1 and the ϵ value for the 3 μm curve can be used to find a more general equation to calculate the inner rim from the half-width baseline $B(V = 0.5)$ of the 3 μm visibility, as will be shown in Sect. 4.2.

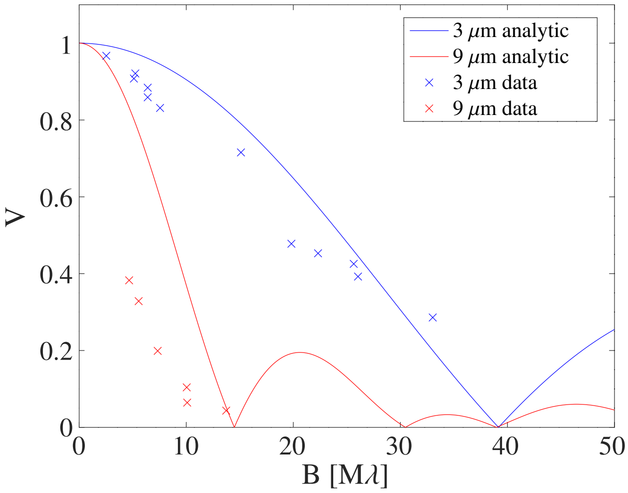

Fig. A.1. Visibilities as measured by Varga, J. et al. (2024) for 3 μm (blue crosses) and 9 μm (red crosses) and analytic ring model visibilities for 3 μm (blue line) and 9 μm (red line). $C_* = 0.05$ for 3 μm and $C_* = 0$ for 9 μm.

Bibliography

Balbus, S. A. & Hawley, J. F. 1998, RvMP, 70, 1

Brauer, F., Dullemond, C. P., & Henning, T. 2008, A&A, 480, 859

Calvet, N. & Gullbring, E. 1998, The Astrophysical Journal, 509, 802

Carmona, A., van den Ancker, M. E., & Henning, Th. 2007, A&A, 464, 687

Chandrasekhar, S. 1960, Proceedings of the National Academy of Sciences, 46, 253

Chase, M. W. et al. 1986, JANAF Thermochemical Tables, 3rd edn (U. S. Department of Commerce)

Chiang, E. I. & Goldreich, P. 1997, ApJ, 490, 368

Clarke, C. J. & Carswell, R. F. 2009, Principles of Astrophysical Fluid Dynamics (Cambridge University Press)

Collaboration, T. E. H. T., Akiyama, K., Alberdi, A., et al. 2019, The Astrophysical Journal Letters, 875, L1

Commerçon, B., Teyssier, R., Audit, E., Hennebelle, P., & Chabrier, G. 2011, A & A, 529, A35

Davis, T. A. 2006, Direct Methods for Sparse Linear Systems (Society for Industrial and Applied Mathematics)

Dullemond, C. P., Dominik, C., & Natta, A. 2001, ApJ, 560, 957

Dullemond, C. P. & Monnier, J. D. 2010, Annu. Rev. Astron. Astrophys., 48, 205

Flock, M., Fromang, S., Turner, N. J., & Benisty, M. 2016, ApJ, 827, 144

Flock, M., Fromang, S., Turner, N. J., & Benisty, M. 2017, The Astrophysical Journal, 835, 230

Goto, M., Henning, T., Kouchi, A., et al. 2009, The Astrophysical Journal, 693, 610

Habart, E., Natta, A., & Krügel, E. 2004, A&A, 427, 179

Hashimoto, A. 1990, Nature, 347, 53

Herbig, G. H. 1960, ApJS, 4, 337

Isella, A. & Natta, A. 2005, A & A, 438, 899

Johnson, R. W. 1998, The Handbook of Fluid Dynamics (CRC Press LLC)

Keppler, M. et al. 2018, A&A, 617, A44

Lenzuni, P., Gail, H.-P., & Henning, T. 1995, ApJ, 447, 848

Levermore, C. D. & Pomraning, G. C. 1981, ApJ, 248, 321

Morfill, G. E. 1988, Icarus, 75, 371

Müller, A., Carmona, A., van den Ancker, M. E., et al. 2011, A&A, 535, L3

Nagahara, H., Kushiro, I., & Mysen, B. O. 1994, Geochimica et Cosmochimica Acta, 58, 1951

Nakamura, T. M. et al. 2007, METEORIT PLANET SCI, 42, 1249

Pérez, M. R., van den Ancker, M. E., de Winter, D., & Bopp, B. W. 2004, A&A, 416, 647

Ruden, S. P. & Pollack, J. B. 1991, ApJ, 375, 740

Schobert, B. N., Peeters, A. G., & Rath, F. 2019, ApJ, 881, 56

Schobert, B. N. & Peeters, A. G. 2021, A&A, 651, A27

Shakura, N. 2018, Accretion Flows in Astrophysics (Springer International Publishing AG)

Shakura, N. I. & Sunyaev, R. A. 1973, A & A, 24, 337

Tachibana, S. et al. 2011, ApJ, 763, 16

Ueda, T., Okuzumi, S., & Flock, M. 2017, ApJ, 843, 49

van Cittert, P. 1934, Physica, 1, 201

van den Ancker, M. E., de Winter, D., & Tjin A Djie, H. R. E. 1998, A & A, 330, 145

Van der Vorst, H. A. 1992, SIAM J. Sci. Stat. Comput., 13, 631

Varga, J., Ábrahám, P., Chen, L., et al. 2018, A&A, 617, A83

Varga, J., Waters, L. B. F. M., Hogerheijde, M., et al. 2024, A&A, 681, A47

Velikhov, E. P. 1959, Zhur. Eksptl'. i Teoret. Fiz., 36

Wolf, S. & Voshchinnikov, N. V. 2004, CoPhC, 162, 113

Zernike, F. 1938, Physica, 5, 785

Acknowledgements

First, I sincerely thank my thesis supervisor, Prof. Dr. Arthur G. Peeters, for his exceptional guidance, valuable advice, and constant support throughout this project.
Further, I would like to thank my colleague and friend Dr. Lucas Löhnert for all the inspiring discussions we had over the several years we worked together.
Finally, I thank my family for their support and encouragement, which I could always rely on.

Eidestattliche Versicherung

Hiermit versichere ich an Eides statt, dass ich die vorliegende Arbeit selbständig verfasst und keine anderen als die von mir angegebenen Quellen und Hilfsmittel verwendet habe.

Weiterhin erkläre ich, dass ich die Hilfe von gewerblichen Promotionsberatern bzw. -vermittlern oder ähnlichen Dienstleistern weder bisher in Anspruch genommen habe, noch künftig in Anspruch nehmen werde.

Zusätzlich erkläre ich hiermit, dass ich keinerlei frühere Promotionsversuche unternommen habe.

Bayreuth, den ....

....
(Benjamin N. Schobert)